EXPERIMENTAL STUDY OF THE COMBINED GRAVITY AND ROTATION EFFECT ON LAMINAR NATURAL CONVECTION IN A SQUARE HORIZONTAL ENCLOSURE

Dissertation for the Degree of Ph. D.

MICHIGAN STATE UNIVERSITY
MOHSEN DIAA SHABANA

1990

This is to certify that the

dissertation entitled

EXPERIMENTAL STUDY OF THE COMBINED GRAVITY AND ROTATION EFFECT ON LAMINAR NATURAL CONVECTION IN A SQUARE HORIZONTAL ENCLOSURE

presented by

Mohsen Diaa Shabana

has been accepted towards fulfillment of the requirements for

Ph.D. degree in Mechanical Engineering

Major professor

Date 5-14-90

EXPERIMENTAL STUDY OF THE COMBINED GRAVITY AND ROTATION EFFECT ON LAMINAR NATURAL CONVECTION IN A SQUARE HORIZONTAL ENCLOSURE

By

Mohsen Diaa Shabana

A DISSERTATION

Submitted to
Michigan State University
in partial fulfillment of the requirements
for the degree of

DOCTOR OF PHILOSOPHY

Department of Mechanical Engineering

1990

ABSTRACT

EXPERIMENTAL STUDY OF THE COMBINED GRAVITY AND ROTATION EFFECT ON LAMINAR NATURAL CONVECTION IN A SQUARE HORIZONTAL ENCLOSURE

By

Mohsen Diaa Shabana

The effect of interacting gravity fields and in-plane rotational body forces on natural convection heat transfer was experimentally studied in a parallelepiped enclosure of square cross-section which rotates about its horizontal longitudinal axis at uniform speeds. The working fluid was air, and buoyant flow was induced by differential heating of two opposite longitudinal walls of length-to-height ratio ten. A fiber optics-based laser sheet and smoke flow visualization technique was used for qualitative assessment of the flow field. A Mach-Zehnder interferometer was used for real time evaluation of the entire temperature field, which allowed subsequent calculation of local and mean Nusselt numbers at the heated walls at discrete angular positions. The angular positions selected for data reduction were 0°, 270°, 180°, and 90°, which during clockwise rotation correspond to the enclosure being: heated from above, vertical with the hot wall on the right side, heated from below, and vertical with the hot wall on the left side, respectively.

Rayleigh number was fixed at 1.77×10^5 throughout the experiments, while the effect of rotation was studied by varying Taylor number from 10^5 to 10^7. The results showed the existance of an intermediate transitional Taylor number (or rotational Reynolds number) range ($1.3\times10^6 \leq Ta \leq 2.8\times10^6$), which distinctly separates two characteristically different flow regimes: at low speed rotation where gravity was dominant, and at high speed rotation where the centrifugal force had increased influence.

At relatively low rotation rates, gravitational buoyancy dominated the flow, and heat transfer was shown to be highly dependent on the angular position because of the periodic nature of the imposed gravity field. Also at low speed rotation, the Coriolis force induced secondary cross flows, which increased mixing of the core region fluid, and slightly enhanced the heat transfer. However, heat transfer was shown to decrease by more than 60% over the transitional region as a result of the growing thermal boundary layer. At relatively high rotation rates, flow was characterized by near solid body rotation which stabilized the flow, and heat transfer was shown to again increase steadily with rotation. An interesting result of the study was obtained in high speed rotation, where the centrifugal buoyancy resulted in a unique two cell flow pattern, and temperature fields which resemble the classic case of a fluid layer heated from below under stable conditions.

In general the rotation effect was to stabilize the flow and relatively enhance the heat transfer prior to and after the transition. Also at slow rotation the effect of rotation was to render the Nusselt number distribution more uniform. In addition, detailed flow and temperature field information as well as local and mean Nusselt number distributions were made available, and experimental Nusselt number correlation was obtained at high rotation rates.

To my wife, *Mona*

and my children,

Maie, Rehab and Ramy

ACKNOWLEDGEMENTS

I would like to express my sincere gratitude to my major advisor, Professor John R. Lloyd for his patient guidance, continued support and motivation, and valuable advice throughout the course of this work, which helped me develop better appreciation of independent scientific research. I am also grateful to Professor K.T. Yang for his assistance in providing the numerical work.

I would like to thank my committee members, Professor John McGrath, Professor Craig Somerton, and Professor Byron Drachman for their assistance and constructive input. Thanks is also due to Dr. Fakhri Hamady for his assistance, and to Mr. Leonard Eisele of the machine shop for building the experimental equipment.

Table of Contents

LIST OF FIGURES

LIST OF TABLES

NOMENCLATURE

a	Acceleration vector, m/sec^2
c	Specific heat, J/kg . K
g	Gravitational acceleration, m/sec^2
h	Convective heat transfer coefficient, W/m^2 . K
H	Enclosure height, m
k	Therma conductivity, W/m . K
L	Enclosure length, m
Nu	Nusselt number
p	Pressure, N/m^2
Pr	Prandtl number
r	Position vector
R	Universal gas constant, J/kg . K
Ra	Rayleigh number
Ra_r	Rotational Rayleigh number
Re	Reynolds number
S	Volumetric heat generation, W/m^3
t	Time, sec.
T	Temperature, deg. K
Ta	Taylor number
v	Velocity vector, m/sec

Greek Letters

α	Thermal diffusivity, m^2/sec
β	Coefficient of volumetric therma expansion, 1/K
θ	Temperature difference
μ	Dynamic viscosity, kg/m . sec
ν	Kimenatic viscisity, m^2/sec

ρ	Density, kg/m^3
ϕ	Angle between cold wall and horizontal, deg.
ω	Angular speed, rad/sec
Ω	Rotational speed, rpm

Subscripts

C	Cold wall
H	Hot wall
p	at constant pressure
in	Inertial
ro	Rotational
0	Reference condition

Superscripts

*	Non-dimensional

CHAPTER 1

INTRODUCTION

1.1 Rationale for the Present Study

Energy transfer by natural convection in rotating cavities is a phenomenon of significant impact on the design of optimal cooling systems, and accurate temperature control devices for a wide variety of rotating machinery in both industrial and laboratory applications, such as rotating heat pipes, thermosyphones, and heat exchangers. Cooling the rotating field windings of high capacity electric generators, the large blades of high performance gas turbines, and the rotor of a super conducting generator using liquid helium are also among the numerous examples that involve the flow of coolant in rotating channels of different geometries and orientations relative to the axis of rotation. Natural convection also plays an important role in crucial manufacturing processes such as crystal growth by chemical vapor transport, and spin casting of molten metals. Another class of natural convection problems in rotating systems invlove situations where gravity effects are relatively or completely negligible as in outer space applications. Examples of such applications are heat transfer in satellites in orbit where gravity is small compared to the rotational forces, and deliberate heating or cooling of fuel storage tanks aboard space vehicles for pressure control.

Natural convection currents are the result of buoyancy forces which are normally induced by body force fields acting on a fluid which posseses density gradients. In most enclosure situations the density gradients are the result of thermal gradients due to temperature differences between the enclosure walls and/or internal heat generation. The process results in energy transfer at the boundaries of the enclosure. In most stationary enclosures, gravity induces an upward buoyancy field in the thin fluid layer adjacent to the heated walls, which in general drives the contained fluid into primary cellular motion, and secondary boundary layer flows that either accelerate or retard the main flow and therefore increase or decrease the heat transfer depending on the orientation of the enclosure walls relative to the gravity vector.

In rotating enclosures however, the centrifugal and Coriolis forces of rotation interact with gravity to produce more complex regimes of buoyant fluid flow. A fluid element inside a rotating cavity is acted upon by three force fields, the gravitational field which exerts a periodic force except when the fluid element is rotating about a vertical axis, a uniform centrifugal field which acts in the radial direction, and a Coriolis force which drives the fluid element toward the center of curvature of its path. Note that the strength of the rotational forces howevere is a function of the radial distance from the center. Each one of these three forces combined with the density gradients within the fluid creates its own buoyancy field, however it is the combined complex buoyancy field that can have profound effects on the heat transfer process inside the enclosure. Note that while the magnitude of the gravity force is constant the other two forces increase with the speed of rotation, thereby creating domains of different flow and heat transfer characteristics based on the influence of the most dominant force (or combination of forces) in a particular domain.

As will be shown later in the literature review, even though much is known regarding fluid flow in simple rotating enclosures, there is not a large body of experimental data relevant to the effect of rotation on heat transfer, and most of the existing literature in this regard does not acknowledge the effect of an interacting gravity field. This indicates that much remains unknown in the more complex rotating enclosure systems with gravity effects, where basic experiments are scarce and highly required for the understanding of the fundamental aspects of heat transfer in crucial applications such as those mentioned in the beginning of this section. A review of the technical literature relevant to convection heat transfer in rotating enclosures is presented in the following section to provide more insight into the physical phenomena involved, and more appreciation of the subject.

1.2 Literature Review

Rotating fluid flows and the coupled phenomena of heat and mass tranfer in rotating systems have been the focus of increased research attention over the past three decades. Extensive studies in this area range in interest from understanding the fundamental aspects of the underlying physical phenomena in simple configurations, to optimization of the transport process in more complex configurations which arise in industrial applications. Basic studies are generally aimed at understanding the effect of rotation on, (a) the stability of heated fluid layers, and (b) how it is manifested in the transfer of heat at the solid boundaries in contact with the rotating fluid. The solid boundaries fall under one of three categories, (i) a heated extended horizontal surface that spins about a vertical axis, (ii) an open channel or annulus which rotates about its longitudinal axis, with either axial or radial forced flow, and uniform heating, or (iii) a closed container that rotates about a geometric or parallel axis with different walls at different temperatures.

A wealth of literature is also found for a broad spectrum of industrial applications that can be divided into two main groups. The first group involves cooling of rotating assemblies of high performance power generation devices such as large gas turbine blades, impelers and rotors, field windings of large generators, motors and centrifugal pumps etc. (Metzger and Afgan 1984, Yang 1987). The second group involves such manufacturing processes as, crystal growth from a melt (Langlois 1984,1985) or by chemical vapor deposition (Yang et al. 1988), and pulp flow in paper refiners (Kheshgi and Scriven 1985). Studies are also found in relevant applications such as heat transfer augmentation devices (Bergles 1968), rotating heat pipes (Marto 1984) and thermosyphones (El-Masri 1984, Eckels et al. 1987).

A literature review on the subject of fluid flow and heat transfer in open and closed rotating enclosures is presented next. This review is in no way a complete survey of the all related studies, however it is an attempt to cover the most important studies that relate to the fundamental aspects of the present study.

Chandrasekhar (1961) presented one of the earliest in depth anlalyses of the stability of the classical case of a fluid layer above a horizontal heated surface which is known as the Benard-Rayleigh problem. Since then several comprehensuve studies (Veronis 1968, Torrest and Hudson 1974, Catton 1978, Yang et al. 1988) have treated the same problem and showed that cellular convection ensues in the fluid layer when a critical Rayleigh number Ra_c is reached or when the buoyancy force created by gravity in the vertical direction overcomes the viscous stability. When the fluid layer is rotated it is known that the centrifugal and Coriolis accelerations of rotation will create additional buoyancy fields which greatly affect stability and the characteristics of the convection flows in the layer. Rossby (1968) studied the effect of rotation on thin layers of water and mercury and found that the heat transfer increased in water as rotation increased up to a certain value of Taylor number, and that it decreased in mercury with increasing Taylor number. He also concluded that linear theory was insufficient to fully describe the stability characteristics of the layers. The same problem has been extensively studied by others like Gillman (1973), Abell and Hudson (1975), Hunter and Riahi (1975), Clever and Busse (1979), and Homsy and Hudson (1971 & 1972) who showed that the centrifugal force stabilizes the horizontal layer everywhere except near vertical boundaries.

Bühler and Oertel (1982) treated the cellular convection problem in a rectangular box that rotates about a vertical geometrical axis, both theoretically through the use of linear stability theory, and experimentally by using interferometry to quantitatively interpret the convection flow. In their experimental investigation they were able to study the influence of the centrifugal and Coriolis forces approximately independently of each other through the use of a high Prandtl number test fluid (silicon oil) and a low Prandtl number test fluid (nitrogen), respectively. The experiments in this study were done up to a rotation rate of 150 rpm, however the centrifugal effects were neglected in the physical model which showed good agreement with the experiment for the case of low Prandtl number only. The results showed that the side walls have a stabilizing effect because of the additional viscous shear, and that rotattion characterised by Taylor number increased the critical Rayleigh number further and delayed the oncet of cellular convection which indicate that Coriolis force stabilized the flow.

Emphasis in the studies presented so far has been on the effect of rotation on flow stability and flow patterns in rotating horizontal layers heated from below where the gravity vector is orthogonal to the plane of the rotational forces, with little or no emphasis on the temperature field or the heat transfer. However it is found that fluid flow and the related problem of convection heat transfer have been more widely studied in rotating open cyliders, rectangular ducts and annuli due to the profound impact on the design of efficient coolant circulation channels in high capacity rotating machinery. The problem in this case is complex and more difficult to analyze because of the superimposed primary forced flow field that can be either axial or radially inward or outward. Morris (1981) has presented a rather comprehensive review of this subject for channels rotating about a parallel or perpendicular axis of rotation.

Experimental and theoretical studies of convection heat transfer in a rotating radial circular tube which is pertinent to the coolant channels of gas turbine rotor blades were carried out by Schmidt (1951), Barua (1955), Mori and Nakayama (1968), Mori et al. (1971), Vidyanidhi et al. (1977), Morris and Ayhan (1979), Firouzian et al. (1985, 1986), and most recently by Northrop and Owen (1988). It was shown that the Coriolis force induces secondary flows both in the direction of

the
inc
the
pri
dec
eff
Tay
of

con
flow
exp
the
uan

a tu
and
bec
infl
temp
at th
have
cylin
num
Siegw
Stepn
Pera

the flow and in the perpendicular direction which creates additional mixing and increases the heat transfer, while the effect of the centrifugal force as represented by the rotational Rayleigh number was shown to be dependent on the direction of the primary flow as it caused an increase in Nusselt number for outward flow and a decrease for inward flow (Morris and Ayhan 1984). Siegel (1985) also included the effect of the centrifugal buoyancy in a series expansion analysis for the case of low Taylor number. His results however correlated reasonably with the experimental data of Morris and Ayhan (1979).

The emphasis in heat transfer in coolant channels also motivated studies of other configurations of rotation. The case of fully developed laminar and turbulent forced flow in a horizontal cylinderical tube rotating about its geometrical axis has been experimentally studied by Cannon and Kays (1969). They found that rotation delayed the transition to turbulent flow to higher Reynolds numbers. The corresponding heat transfer problem was studied by Hudson (1970).

Another rotation configuration which has been extensively investigated is that of a tube rotating about a parallel axis. Mori and Nakayama (1967), Nakayama (1968), and Sakamoto and Fukui (1970) studied both laminar and turbulent forced convective heat transfer in a pipe rotating around a parallel axis. The studies showed that influential secondary flows cause remarkable skewness in the axial velocity and temperature profiles. Humphery et al. (1967) investigated the convection heat transfer at the entrance region of the corresponding problems. Woods and Morris (1980) have numerically treated the fully developed flows in the parallel revolving horizontal cylinder with axial flow over a broad range of Rayleigh, Reynolds, and Prandtl numbers. Their correlation agreed with the results of the asymptptic analysis of Siegwarth et al. (1969) for high Prandtl number fluids. An experimental study by Stephenson (1984) on turbulent flow and heat transfer in high rotational speed (parallel mode) circular duct showed that rotational buoyancy effects are not generally significant, but may become important in fully developed flow at high rotation rates and low flow rates.

Of equal importance to the parallel rotating cylinder is the parallel rotating rectangular duct. Flow and heat transfer studies in the rectangular cross-sectioned ducts are few despite the fact that it can be found in a broad variety of cooling applications for the simplicity in manufacturing rectangular channels in long power transmission shafts. Numerical studies by Neti et al. (1985) and Levy et al. (1986) demonstrated the significant effect of the buoyant secondary flow induced by the Coriolis force on the heat transfer.

Forced fluid flow in annuli formed between two rotating cylinders and the associated convective heat transfer have also been the subject of several studies. Diprima and Swinney (1981), Kataoka et al. (1984), and most recently Yong and Minkowycz (1989) have treated the flow stability and heat and mass transfer in concentric rotating cylinders. Kuzay and Scott (1977), Kataoka and Deguchi (1987), Ball et al. (1989) and others have treated vertical annuli when the inner cylinder is rotating and the outer is stationary. The more complex problem of two eccentric rotating cylinders has been treated analytically by Singh and Rajvanshi (1982).

Another class of fluid flow and convection heat transfer is that of closed rotating enclosures. this class of problems is important for understanding the local and overall heat flux distribution and the associated thermal stresses in internal cavities of rotating machinery. The current investigation is categorized under this class of rotating enclosures in which buoyant flows are driven by the density gradient and the gravity field as well as the rotational body forces that affect every differential volume element of the working fluid. While the centrigugal and Coriolis forces of rotation act uniformly in the radial direction perpendicular to the axis of rotation, the effect of gravity depends entirely on the angle of inclination between the axis of rotation and the gravity vector.

(19

ann

cyli

init

rota

cent

expe

in a

show

exte

spee

moti

and

almo

How

rota

gravi

by H

conv

simil

enha

force

exper

able

perfor

Numerical studies by de Vahl Davis et al. (1984) and Randriamampianina et al. (1987) on the natural convection heat transfer and fluid flow in a differentially heated annular cavity of square cross-section formed between two vertical concentric cylinders and two horizontal planes. The studies showed that the heat transfer initially decreased with increasing rotation, and started to increase at sufficiently high rotation rates, where it became independent of the Rayleigh number as the centrifugally driven motion became dominant. Sobel et al. (1986) have experimentally studied the heat transfer and flow patterns of rapidly spinning systems in a rectangular annulus similar to that of de Vahl Davis et al. (1984). The study showed the existance of weak radially inward plumes that rise from the heated external cylinder, which reflects the effect of centrifugal buoyancy at high rotation speeds. They were also able to conclude that spinning resulted in two dimensional motion, and that the heat transfer coefficient is independent of the heater lengh scale and fluid viscosity. The radial buoyant flow structures dealt with in these studies are almost independent of the garvity effect since the axis of rotation is vertical. However more complex flow regimes can result from inclination of the axis of rotation relative to the gravity vector because of the interaction between the gravitational and rotational buoyancy fields.

An experimental as well as numerical investigation has been recently carried out by Hamady (1987) and Hamady et al. (1990) on the effect of low speed rotation on convective heat transfer in a square enclosure rotating about its horizontal axis, similar to that used in the present study. The study showed that low speed rotation enhances heat transfer due to the secondary radial flows induced by the Coriolis force. They also showed that the numerical calculations can accurately predict the experimental results within their range of Rayleigh and Taylor numbers, and were able to correlate the Nusselt number results with Ra and Ta. Yang et al. (1988b) performed a similar numerical study in a rotating horizontal cylider heated

differentially at both ends. They too concluded that at slow rotation the Coriolis force has a significant influence on the temperature field as it renders the spatial heat flux distribution more uniform. They also noted that increasing rotation results in more uniform and weaker buoyancy field.

The brief review presented above shows that knowledge of heat transfer in rotating enclosures is rather limited, especially when the effect of the gravity field is significant, and that more related studies are needed over a broad range of the controling parameters in order to better asses the influence of rotation and understand the underlying physical phenomena.

1.3 Specific Objectives of the Present Study

In light of the lack of knowledge addressed above in regard to the combined effect of gravity and rotation on fluid flow and heat transfer in enclosures, the present study is aimed at experimentally investigating such effects in a simple differentially heated, air filled square enclosure that rotates about its geometrical axis, which is oriented in a direction orthogonal to the gravity vector. The benefit from the study is twofold, first to gain physical understanding both qualitatively and quantitatively of the effect of the interaction of gravitational and rotational fields on fluid flow and heat transfer in rotating enclosures, second to validate a numerical model developed by Yang et al. (1988), which once validated can be utilized to predict the enclosure flow and heat transfer in experimentally hard to simulate situations, such as more complex enclosure configurations and boundary conditions, tilted orientations relative to the gravity vector, and extreme values of the controlling parameters.

The present study is performed in a square enclosure with two opposite isothermal walls at different temperatures and two adiabatic walls. Such configuration is chosen to allow direct comparison of the present results with those that are now known for slowly rotating enclosures (Hamady et al. 1990). The Rayleigh number which represents a measure of the gravity force relative to the viscous shear forces is held constant, while the rotational Rayleigh and the Taylor numbers which represent the Coriolis and centrifugal forces, respectively, are varied as a result of changing the speed of rotation. The speed of rotation ranges from relatively low rates, where the gravitational bouyancy is expected to dominate the flow field, to relatively high rates, where centrifugal buoyancy is expected to become more influential.

Two types of experiments are performed. In the first experiment flow visualization using smoke and laser sheet is utilized to qualitatively reveal the nature of the different flow regimes and their subsequent impact on the temperature field. In the second experiment a Mach-Zehnder interferometer is employed to show the entire temperature field and quantify the local Nusselt number distribution at the isothermal walls at angular positions of 0° (which means at the intant the enclosure reaches the heated from above position), 270° (vertical position), 180° (heated from below position), and 90° (the opposite vertical position). Finally the mean and overall Nusselt numbers are calculated and correlated with the controling parameters.

CHAPTER 2

MATHEMATICAL FORMULATION

2.1 Problem Statement

The present study deals with natural convection in a rotating enclosure. As shown in figure 2.1 the enclosure is a parallelepiped cavity, with a square cross-section of side H, i.e. aspect ratio = 1, and of length L. In the enclosure the two opposite longitudinal walls are isothermal while the other four walls are adiabatic. One of the isothermal walls is maintained at a low temperature, T_C, while the other is maintained at a relatively higher tempetrature, T_H, and they are denoted *the cold and hot walls*, respectively. The enclosure is filled with air and rotates with a uniform angular velocity, $\mathbf{\Omega}$, about its longitudinal axis, which is oriented perpendicular to the gravity vector, $\mathbf{g}$. Note that bold face symbols are used to represent vector fields throughout this chapter.

An angle of rotation, ϕ, is defined as the angle between the horizontal plane passing through the axis of the enclosure, and the cold wall. In this notation an angle of rotation $\phi = 0°$ means that the enclosure is heated from above, $\phi = 90°$ or $270°$ is heated from the side, and $\phi = 180°$ is heated from below.

Buoyancy flows in this situation are induced by the combined effect of density gradients which result from the difference in temperature between the two isothermal walls, and the driving body forces that consist of a periodic gravity force and

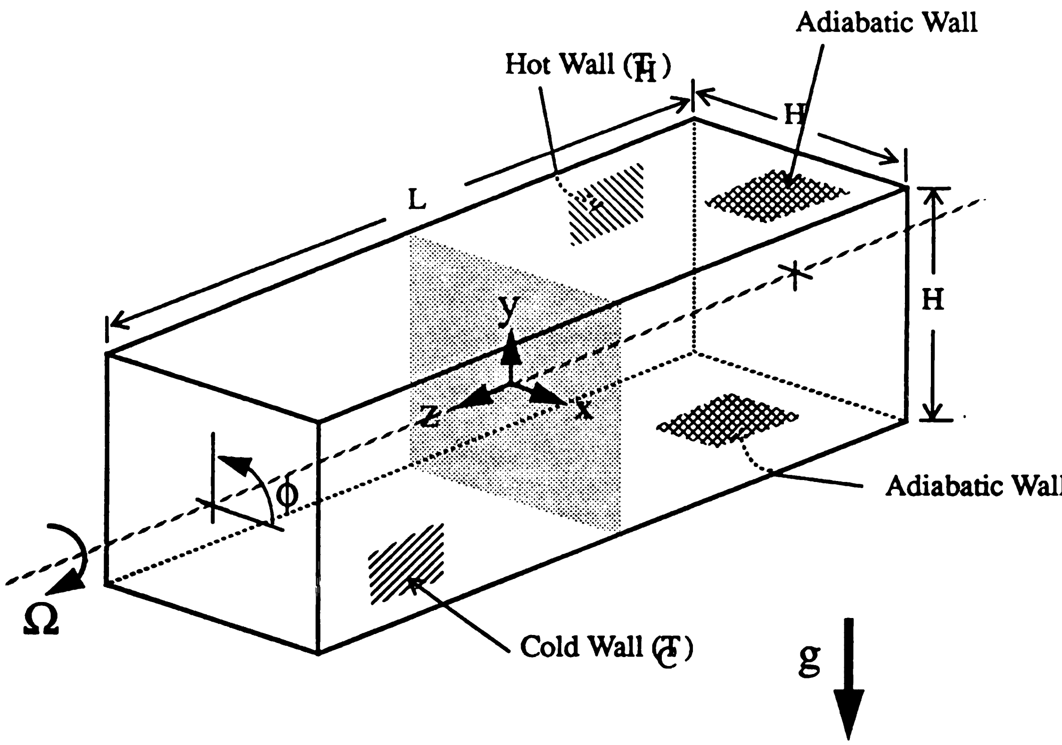

Figure 2.1 The Rotating Square Enclosure

uniform centrifugal and coriolis forces. External forces such as inertial and viscous forces also help shape the flow patterns either by retarding or assisting the motion of the fluid.

2.2 Governing Equations and Boundary Conditions

The differential equations governing natural convection flows in enclosures are the mass, momentum, and energy conservation equations. For a laminar, variable property, compressible Newtonian fluid these governing equations can be written in vector form as follows:

Mass Conservation

$$\frac{\partial \rho}{\partial t} + \nabla \cdot (\rho \mathbf{v}) = 0 \tag{2.1}$$

Momentum Conservation

$$\rho \frac{D\mathbf{v}}{Dt} = -\nabla p + \mu \nabla^2 \mathbf{v} + \frac{\mu}{3} \nabla (\nabla \cdot \mathbf{v}) + \rho \mathbf{g} \tag{2.2}$$

Energy Conservation

$$\rho c_p \frac{DT}{Dt} = \nabla \cdot k \nabla T + S \tag{2.3}$$

where, ρ, μ, c_p, and k are the density, the dynamic viscosity, the specific heat at constant pressure, and the thermal conductivity of the fluid respectively. Also, t is the time, p is the static pressure, and T is the temperature. **v** and **g** represent the velocity and the gravity vectors, respectively, and S represents a volumetric heat source. ∇

and ∇^2 are the gradient and laplacian operators, respectively, while D/Dt is the substantial derivative ($\partial / \partial t + \mathbf{v} \cdot \nabla$). It must also be noted that the viscous dissipation and pressure work terms in the energy equation are neglected because of the small velocities associated with free convection, as shown by Gebhart (1971).

So far the velocity and acceleration components in the governing equations have been described in an inertial coordinate system, i.e. relative to a fixed point in space. However, the equations are often described in a rotating coordinate system in order to simplify the mathematical analysis.

The velocity and acceleration vectors of a typical fluid element, A, shown in figure 2.2, can be described by defining the position vector, **r**, relative to the rotating coordinate system, *xyz*, as follows:

$$\mathbf{r} = x\,\mathbf{i} + y\,\mathbf{j} + z\,\mathbf{k} \tag{2.4}$$

where **i**, **j** and **k** are the unit vectors in the *x*, *y* and *z* respectively. The velovity, $\mathbf{v}_{ro}$, and the acceleration, $\mathbf{a}_{ro}$, can now be defined in the rotating coordinate system as follows:

$$\mathbf{v}_{ro} = \left[\frac{d\mathbf{r}}{dt}\right]_{ro} \tag{2.5}$$

$$\mathbf{a}_{ro} = \left[\frac{d\mathbf{v}_{ro}}{dt}\right]_{ro} = \left[\frac{d^2\mathbf{r}}{dt^2}\right]_{ro} \tag{2.6}$$

As shown by Potter and Foss (1975), the velocity and acceleration vectors of fluid element A can also be related to the inertial coordinate system, *XYZ*, as follows:

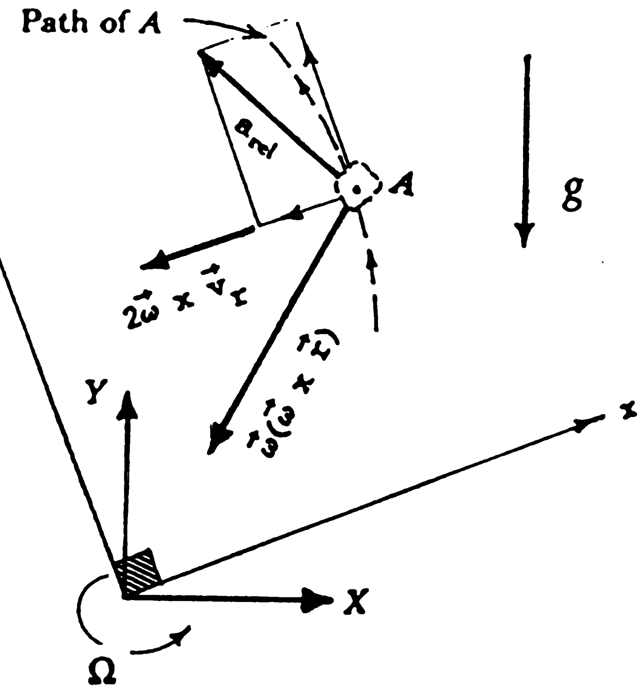

Figure 2.2 Fluid Element in a Rotational Frame of Reference

$$\mathbf{v}_{in} = \left[\frac{d\mathbf{r}}{dt}\right]_{in} = \left[\frac{d\mathbf{r}}{dt}\right]_{ro} + \boldsymbol{\omega}\times\mathbf{r}$$

$$= \mathbf{v}_{ro} + \boldsymbol{\omega}\times\mathbf{r} \tag{2.7}$$

and,

$$\left[\frac{D\mathbf{v}_{in}}{Dt}\right]_{in} = \left[\frac{D\mathbf{v}_{in}}{Dt}\right]_{ro} + \boldsymbol{\omega}\times\mathbf{v}_{in}$$

$$= \left[\frac{D}{Dt}\left(\mathbf{v}_{ro} + \boldsymbol{\omega}\times\mathbf{r}\right)\right]_{ro} + \boldsymbol{\omega}\times\left(\mathbf{v}_{ro} + \boldsymbol{\omega}\times\mathbf{r}\right)$$

$$= \left[\frac{D\mathbf{v}_{ro}}{Dt}\right]_{ro} + 2\,\boldsymbol{\omega}\times\mathbf{v}_{ro} + \boldsymbol{\omega}\times(\boldsymbol{\omega}\times\mathbf{r}) \tag{2.8}$$

where,

$$\boldsymbol{\omega} = -\,\Omega\mathbf{k} \tag{2.9}$$

is the angular velocity vector of the rotating *xyz*-reference frame, and the subscripts, *ro*, and, *in*, refer to the rotating and the inertial coordinate systems, respectively.

Substituting equations (2.7) and (2.8) into equations (2.1) and (2.2), the continuity and momentum equations can be described in the rotating frame of reference as follow:

$$\frac{\partial \rho}{\partial t} + \nabla\cdot(\rho\mathbf{v}_{ro}) = 0 \tag{2.10}$$

$$\rho\,\frac{D\mathbf{v}_{ro}}{Dt} + 2\rho\,\boldsymbol{\omega}\times\mathbf{v}_{ro} + \rho\,\boldsymbol{\omega}\times(\boldsymbol{\omega}\times\mathbf{r}) = -\,\nabla p + \rho\nu\,\nabla^2\,\mathbf{v}_{ro}$$

$$+\,\rho\,\frac{\nu}{3}\nabla\left(\nabla\cdot\mathbf{v}_{ro}\right) + \rho\,\mathbf{g} \tag{2.11}$$

where, ν is the kinamatic viscocity, and

$$\nabla \cdot \mathbf{v} = \nabla \cdot (\mathbf{v}_{ro} + \boldsymbol{\omega}\times\mathbf{r}) = \nabla \cdot \mathbf{v}_{ro}$$

$$\nabla^2 \mathbf{v} = \nabla^2 (\mathbf{v}_{ro} + \boldsymbol{\omega}\times\mathbf{r}) = \nabla^2 \mathbf{v}_{ro}$$

Note that two additional terms appear in the momentum equation as a result of rotation. These terms are, $\boldsymbol{\omega}\times(\boldsymbol{\omega}\times\mathbf{r})$, which represents the normal component of the centrifugal acceleration, and, $2\, \boldsymbol{\omega}\times\mathbf{v}_{ro}$, which represents the Coriolis acceleration.

In order to simplify the governing equations the fluid properties are assumed constant, except for density variations that drive the enclosure buoyant flows. This assumption is known as the *Boussinesq approximation*, which is shown by Zhong, Yang and Lloyd (1985) to be valid in the range of the temperature differences used in the present study. The *Boussinesq approximation* states that the density of the fluid is constant, except when multiplied by the centrifugal or gravitational accelerations in the equation of motion, where it can be represented by a linear function of temperature as follows:

$$\rho = \rho_0 \left[1 - \beta \left(T - T_0\right)\right] \tag{2.12}$$

where, $\beta = (1/\rho)\, (\partial\rho/\partial T)_p$, is the thermal expansion coefficient. For a perfect gas ($\rho = p/RT$) β is equal to $(1/T_0)$, where 0 refers to a reference condition. Therefore, in the absence of a heat source the simplified governing equations can be written as follows:

Mass Conservation

$$\nabla \cdot \mathbf{v}_{ro} = 0 \tag{2.13}$$

Momentum Conservation

$$\frac{D\mathbf{v}_{ro}}{Dt} - \nu\, \nabla^2\, \mathbf{v}_{ro} = -\,\frac{1}{\rho_0}\nabla p_k - 2\,\boldsymbol{\omega}\times\mathbf{v}_{ro} - \beta\,(T-T_o)\,\Omega^2\mathbf{r}_1$$

$$-\,\beta\,(T-T_0)\,]\,\mathbf{g} \tag{2.14}$$

Energy Conservation

$$\frac{DT}{Dt} = \alpha\,\nabla^2 T \tag{2.15}$$

where the thermal diffusivity $\alpha = k/\rho c_p$,

$$\boldsymbol{\omega}\times(\boldsymbol{\omega}\times\mathbf{r}) = -\,\Omega^2\mathbf{r}_1 \tag{2.16}$$

$$\mathbf{r}_1 = x\mathbf{i} + y\mathbf{j} \tag{2.17}$$

and, $p_k = p - \rho_0\mathbf{g} - \rho_0\,\Omega^2\mathbf{r}_1$, is defined as the kinetic pressure as it results from dynamic effects, realizing that gravity and centrifugal acceleration are conservative vector fields.

The boundary conditions are the no-slip condition at all walls for the velocity field, and prescribed temperatures at the isothermal walls along with zero heat flux at the adiabatic walls for the temperature field. With the origin ($x = y = z = 0$) located at the geometric center of the enclosure and the xyz coordinates positioned perpendicular to the enclosure surfaces as shown in figure 2.1, those boundary conditions can be written as follows:

$$x = +\,\frac{H}{2}\,, \qquad \mathbf{v}_{ro} = 0\,, \qquad T = T_C \tag{2.18a}$$

$$x = -\,\frac{H}{2}\,, \qquad \mathbf{v}_{ro} = 0\,, \qquad T = T_H \tag{2.18b}$$

$$y = \pm \frac{H}{2}\,, \qquad \mathrm{v}_{ro} = 0\,, \qquad \frac{\partial T}{\partial y} = 0 \tag{2.19}$$

$$z = \pm \frac{L}{2}\,, \qquad \mathrm{v}_{ro} = 0\,, \qquad \frac{\partial T}{\partial z} = 0 \tag{2.20}$$

2.3 Dimensionless Form of Governing Equations

The governing equations are usually normalized before performing an approximate analytical solution or numerical simulation in order to extract dimensionless groups of parameters that most likely govern the problem. The choice of appropriate characteristic scales requires appreciation of their physical effect, which becomes more difficult in enclosure natural convection since different scales can operate in different regimes of the flow, as pointed out by Yang (1987).

In the present formulation, the height of the enclosure, H, is used as the length scale, while α/H, H^2/α, $\rho\alpha\nu/H^2$ and the temperature difference $(T_H - T_C)$ are used as the velocity, time, pressure and temperature scales respectively. Conditions at the temperature of the cold wall are taken as reference conditions, i.e. $T_0 = T_C$ and $\rho_0 = \rho_C$, which was shown to be valid in enclosure flows for the Rayleigh number used in the present study (Zhong et al. 1985). This results in the following dimensionless variables:

$$\mathbf{r}^*_1 = \frac{\mathbf{r}_1}{H}$$

$$\mathbf{v}^*_{ro} = \frac{\mathbf{v}_{ro}}{\alpha/H}$$

$$t^* = \frac{t}{H^2/\alpha}$$

$$p_k^* = \frac{p_k}{\rho\alpha\nu/H^2}$$

$$\theta^* = \frac{T - T_C}{T_H - T_C}$$

$$\mathbf{g}^* = \frac{\mathbf{g}}{g}$$

and also,

$$\nabla^* = H\,\nabla \qquad \textit{and,} \qquad \nabla^{*2} = H^2\,\nabla^2$$

where, the asterisk (*) is used to identify dimensionless variables, and g is the magnitude of the gravity vector. Substituting all the above dimensionless variables in equations (2.13), (2.14) and (2.15) results in the following normalized form of the governing equations:

$$\nabla^* \cdot \mathbf{v}_{ro}^* = 0 \tag{2.21}$$

$$\frac{1}{Pr}\,\frac{D\mathbf{v}_{ro}^*}{Dt^*} - \nabla^{*2}\,\mathbf{v}_{ro}^* = -\,\nabla^*\,p_k^* + Ta^{\frac{1}{2}}\,(\mathbf{k}\times\mathbf{v}_{ro}^*) - Ra_r\,\theta^*\,\mathbf{r}^* - Ra\,\theta^*\,\mathbf{g}^* \tag{2.22}$$

$$\frac{D\theta^*}{Dt^*} = \nabla^{*2}\,\theta^* \tag{2.23}$$

The dimensionless groups in the momentum equation (2.22) are defined as follows :

Prandtl Number

$$Pr = \frac{\nu}{\alpha} \tag{2.24}$$

Rayleigh Number

$$Ra = \frac{g\, \beta\, (T_H - T_C)\, H^3}{\nu\alpha} \tag{2.25}$$

Rotational Rayleigh Number

$$Ra_r = \frac{\beta\, (T_H - T_C)\, \Omega^2\, H^4}{\nu\alpha} \tag{2.26}$$

Taylor Number

$$Ta = \frac{4\, \Omega^2\, H^4}{\nu^2} \quad . \tag{2.27}$$

Prandtl number is a function of fluid properties and it represents the ratio of the momentum to thermal difusivities. *Raleigh number* and *Rotational Rayleigh number* are measures of the gravitational and centrifugal buoyancies respectively as compared to the viscous shear forces, while *Taylor number* is the square of the ratio of Coriolis force to the viscous force.

CHAPTER 3

EXPERIMENTAL APARATUS AND DATA AQUISITION PROCEDURES

3.1 Experimental Facility

The experimental facility used in the present study is shown in figure 3.1. The basic facility consists of an enclosure which is rotated by an electric motor. The basic facility moves on rails and can be positioned inside the test leg of a Mach-Zehnder interferometer for temperature field measurements, or outside the interferometer for flow visualization using smoke and laser light. The active test section surfaces are also connected to two constant temperature water baths through a rotating coupler in order to control the temperatures of the isothermal walls, and are also connected to a digital temperature readout through precision slip rings for accurate wall temperature measurements. Simultaneous photography and observation of the temperature and the flow fields are done using a high speed video camera, and the images are stored on super VHS video tapes for later analysis.

3.1.1 Test Section

Figuer 3.2 shows a schematic of the test section. It consists of two aluminum plates and two plexiglas plates that form the four walls of a rectangular cavity. The aluminun plates and the appropriate plexiglas plates can be positioned to achieve the desired cross-sectional area and aspect ratio of the cavity.

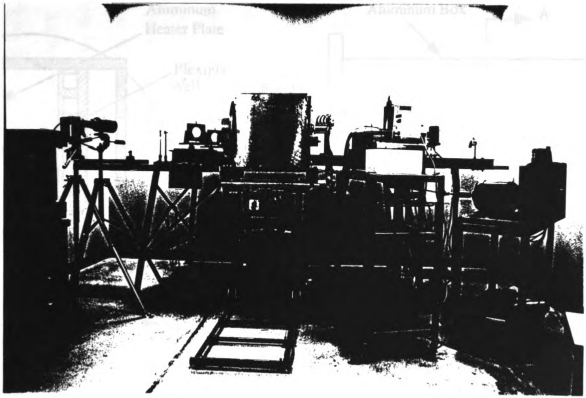

Figure 3.1 Experimental Facility

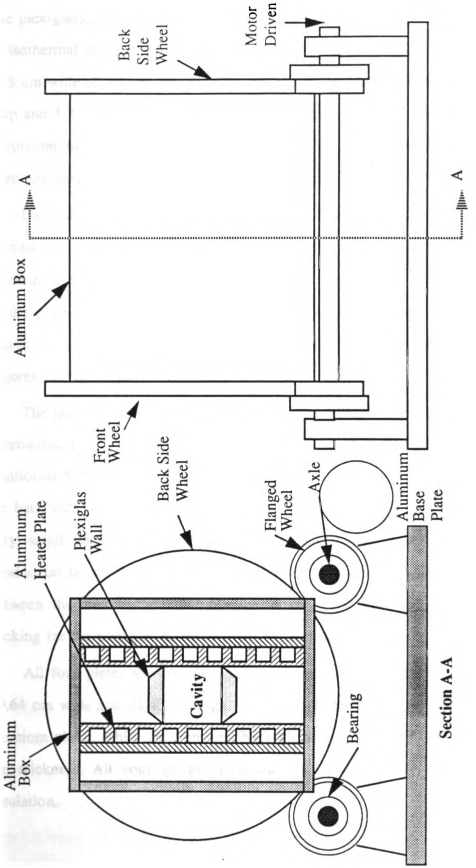

Figure 3.2 Schematic Diagram of the Test Section

The plexiglass plates function as insulated walls, while the aluminum plates are used as isothermal walls. Each isothermal wall was machined from a 50.8 cm long by 50.8 cm wide aluminum tooling plate of 2.54 cm thickness. Square channels 1.27 cm deep and 1.27 cm wide were milled into the back side of the aluminum plate for the circulation of cooling or heating fluid. The front surfaces of the aluminum plates were polished to a smooth finish of 25 μm flatness.

Each aluminum plate was fitted with 18 Copper-Constantan thermocouples to monitor the spatial and temporal variations in the actual wall temperature. The test junction of each thermocouple was cemented in a small hole drilled in the back side of the plate 2.4-4.0 mm away from the front surface. A detailed description of the design of the aluminum plates and the locations of the thermocouples is given by Bajorek (1981).

The insulated plates were made of plexiglas which has a thermal conductivity of approximately 0.5-1 W/mK. The plates are 50.8 cm long and 50.8 cm wide, and were positioned 5.08 cm apart to form a square cavity of side H= 5.08 cm. The edges of the back side of the plexiglas plates were milled at an angle of 60 degrees leaving a very small contact area with the aluminum plates in order to minimize lateral conduction in the insulated walls which will result from the temperature difference between the two isothermal plates. Also layers of fiber glass wool are used as backing for the plexiglas plates in order to decrease heat loss.

All four plates are housed inside a rectangular aluminum box, 51.43 cm long, 40.64 cm wide and 51.43 cm high. The sides of the box are made of 1.27 cm thick alumium plates, while the front and back plates are made of hard aluminum of 2.54 cm thickness. All void spaces inside the box are filled with fiber glass wool for insulation.

Two hard aluminum wheels of 61 cm diameter and 2.54 cm thickness are bolted to the front and back sides of the box. A plexiglas frame at the center of each end wheel holds a circular optical flat window tightly against each of the ends of the square cavity in order to seal the ends and to allow for longitudinal optical observations. The optical flats are made of high quality glass disks, 8.89 cm diameter and 2.54 cm thickness, with accuracy of 0.1 wavelengh. A detailed description of the design of the test section is given by Hamady (1987).

3.1.2 Rotation and Alignment

As shown in figure 3.2, each of the front and back side wheels of the enclosure box is supported on two flanged steel wheels 15.24 cm in diameter. The flanged wheels are grooved and fitted with rubber O-rings for enhanced traction with the test section wheels. Each pair of front and back flanged wheels is connected together by a steel axle 2 cm in diameter. The ends of each axle are mounted in heavy duty bearings, and the bearings are bolted to aluminum blocks which are in turn bolted to an aluminum base plate of 88 cm length, 61 cm width and 2 cm thickness.

One axle is directly driven by a 3/4 HP DC motor [Master Electric Co.] through a connecting rod and two universal joints. The motor is connected to a Variac Speed Control [Type 1702-A General Radio Co.] for easy adjustment of constant rotation speeds, and both units are mounted on a moving table.

As shown in figure 3.3 the base plate is carried on a heavy duty table and can be aligned in all three directions by adjustable screws. The heavy duty table [made by Economy Engineering] provides height adjustment and high capacity load carrying capability (approximately 2000 lb). The table is supported by V-grooved casters that ride on two rail tracks in order to position the test section inside a Mach-Zehnder interferometer for temperature field evaluation, or outside the interferometer for flow visualization experiments.

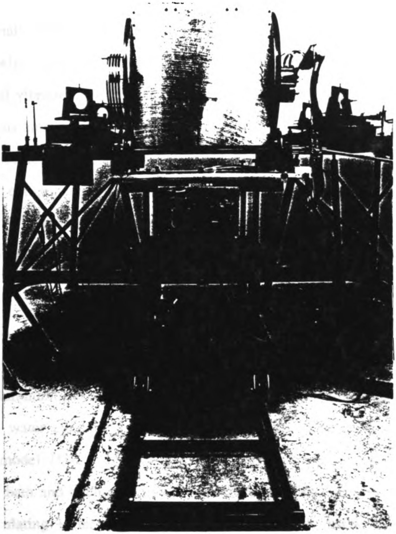

Figure 3.3 Test Section and Supporting Table

The rails are bolted to the floor, with rubber pads placed underneath them to minimize the transmission of the rotation induced vibrations to the optical components of the interferometer.

The small contact surface between the test section wheels and the supporting flanged wheels, in addition to carefully balancing the test section worked to minimize the unwanted vibration of the test section despite its heavy weight. However, a small yet deleterious amount of low frequency, high amplitude vibrations still resulted from the test section rotation at high rotation rates. These vibrations caused disturbances in the optical components and could smear the fringe patterns in interferometry experiments. Therefore, proper padding underneath the interferometer frame and high speed photography were used to solve the vibration problem as discussed later in this chapter.

3.1.3 Wall Temperature Control

The aluminum plates were maintained at uniform temperature by means of closed loop water circulation from constant temperature baths. A heating bath and circulator (model D3-L, HAAKE Co.) was used to heat one plate, while a low temperature bath and circulator (model 90, Fisher Scientific Co.) was used to cool the other. Circulating water from the constant temperature baths in and out of the aluminum plates during rotation required the design of a special high speed rotary water feeder.

Figure 3.4 shows a section in the four channel rotating water coupler used in the present study. The coupler consists of an aluminun cylinder (12.7 cm long x 6.8 cm I.D.) inside of which five equally spaced sealed bearings (FAFNIR 9108PP) were fitted and separated by means of four aluminum spacer rings that have the same outer diameter as the bearings.

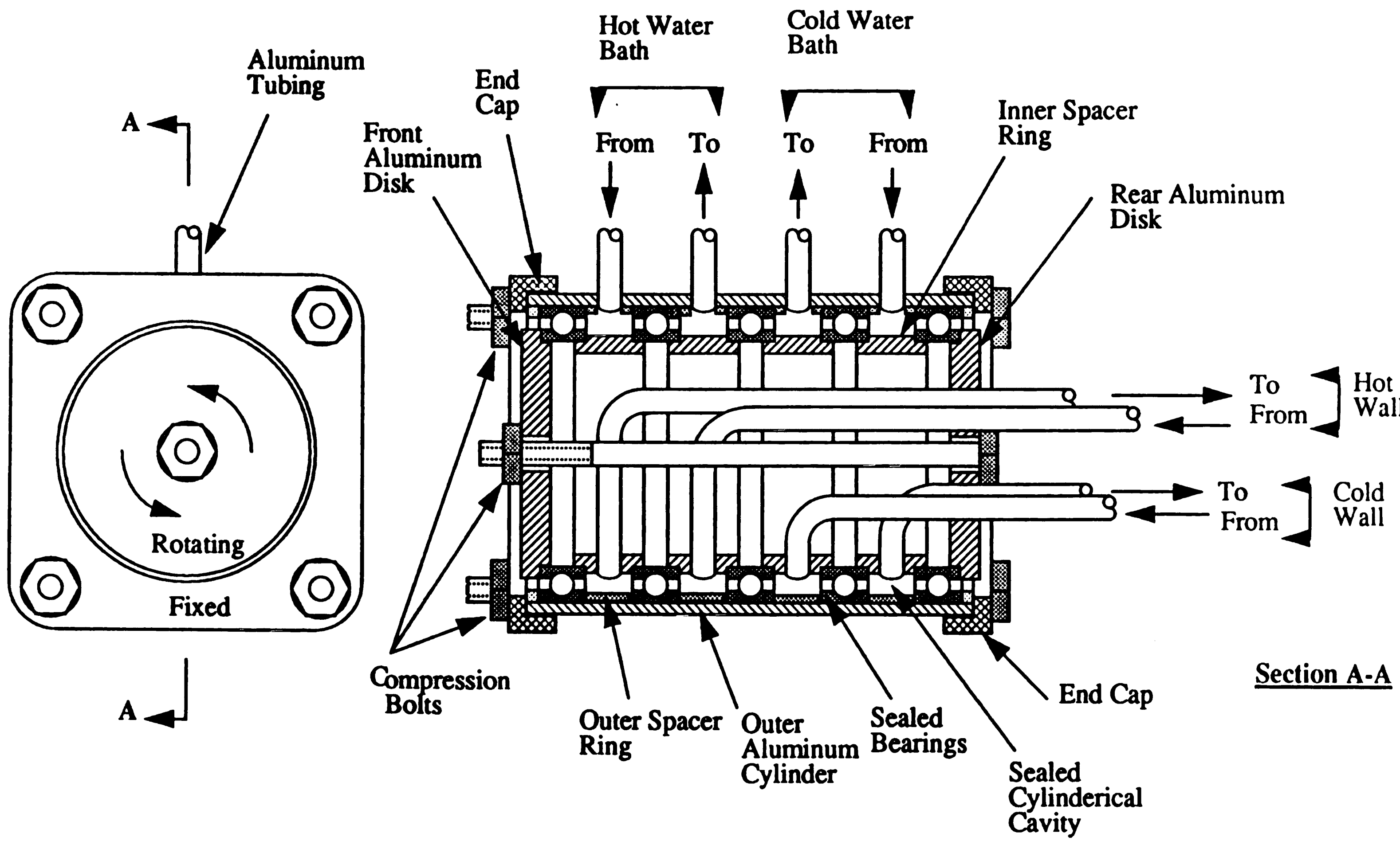

Figure 3.4 Schematic Diagram of Four Channel Rotary Water Coupler

The outer rings of the bearings and the outer spacer rings were compressed together by means of two aluminum end caps mounted on the ends of the cylinder and held together by four long compression bolts. Four concentric inner spacer rings, having the same inner diameter as the bearings and the same width of the outer spacer rings, were compressed between the inner rings of the bearings by means of two aluminum disks which were located at the ends of the assembly. Both disks were held together by an axial compression bolt.

The group of five bearings, four outer spacer rings and four inner spacer rings formed four sealed cylinderical compartments with one inlet and one outlet hole in each compartment for water circulation. The design allowed for independent rotation of the inner and outer cylinderical walls of the fixture. The rear disk of the coupler was bolted to the back wheel of the test section, and four holes were drilled through both parts to internally connect the inner four aluminum tubes (in the right hand side of the schematic) to the inlets and outlets of the isothermal walls by short pieces of tygon tubing. In the mean time, the outer four tubes (in the top of the schematic) were connected to the inlets and outlets of the constant temperature baths for closed loop water circulation.

The rotary water coupler was mounted on the back wheel of the test section as shown in figure 3.5 . The outer cylinder of the coupler was attached to the stationary base plate of the test section by means of a crank-rocker mechanism that keeps the outer part of the coupler in an almost upright position, and exerts a small uniform torque against the rotation of the enclosure.

3.1.4 Wall Temperature Monitoring

As mentioned previously, each one of the isothermal walls was fitted with 18 copper-constantan thermocouples for monitoring the variations in wall temperature.

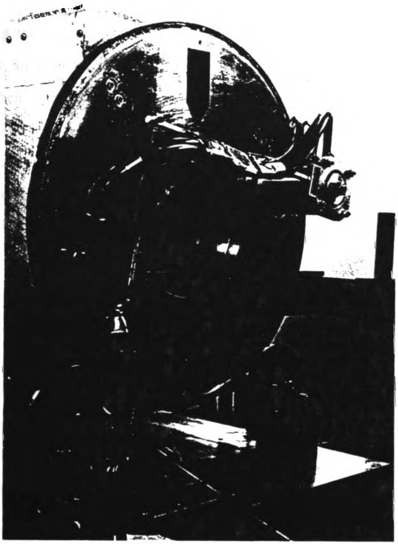

Figure 3.5 Rotary Water Coupler

Details of the wiring and connections of the thermocouples can be found in Hamady (1987). However it is of interest to briefly describe the system used in the present work for temperature data acquisition.

Testing the consistency of the measurements was done in two stages. First the readings of all thermocouples in each wall were compared at steady state without rotation. Then, one representative thermocouple from each wall was chosen and the stability of its readings during rotation was monitored. Measurement of temperature during rotation by means of stationary readouts required a system of rotating sliprings mounted on the test section and non-rotating contact brushes connected to the measuring instrument. Figure 3.6 shows a photograph of the slipring-brush assembly used in the present study as mounted on the front side of the test section.

In the no rotation case extension wires from all functioning thermocouples in each wall (about 15-16 thermocouples in each) were connected to the input leads of a rotary switch [made by Minneapolis Honeywell Regulator Co.] , and the switch output was connected to a microprocessor-based thermocouple meter [Omega Engineering, Inc., model 680/A] with 0.1 °C resoluion and ± 0.4 °C accuracy. Variations in the readings of all termocouples in each wall at steady state were found to be within ± 0.1 °C.

For the rotation case, one representative thermocouple with readings close to the average of all thermocouples in each wall (in the no rotation case) was selected. Each one of the extension wires from the two representative thermocouples was connected to a silver plated copper slipring (two sliprings for each thermocouple). Each slipring is 28.58 cm in diameter with a square cross section of 0.64 cm by 0.64 cm. As shown in figure 3.7, the sliprings were mounted axially on the front wheel of the test section by means of five flanged plexiglass rings bolted to the wheel. The plexiglas flanges held the sliprings and kept them 0.64 cm apart from each other and 3.81 cm from the aluminun body of the test section.

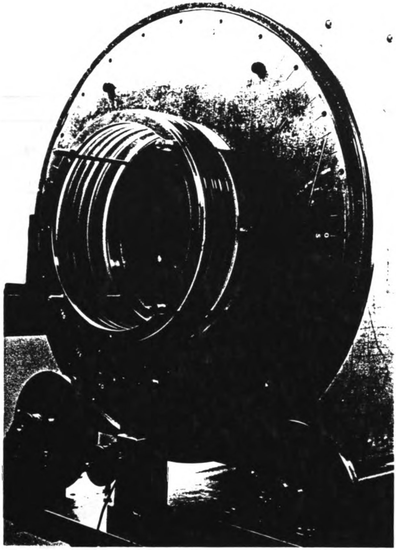

Figure 3.6 Slipring- Brush Assembly

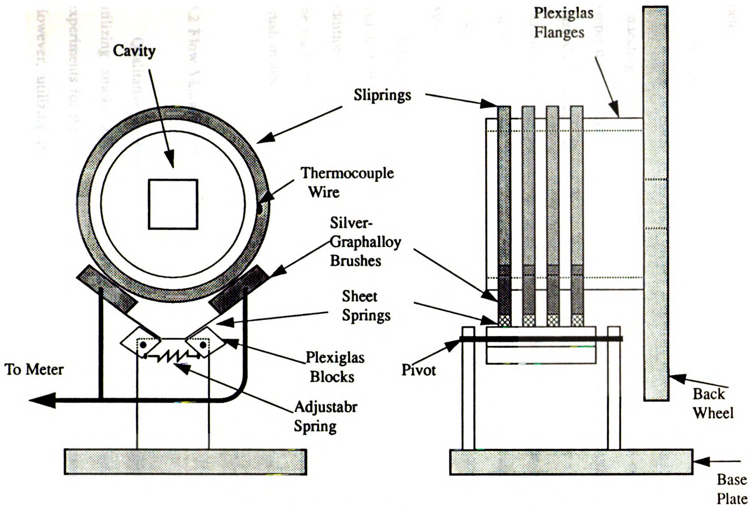

Figure 3.7 Schematic Diagram of Slipring-Brush Assembly

The four pairs of brushes (one pair for each lead wire) were made of Silver Graphalloy [type TS-109096-6 grade, Graphite Metallizing Corporation] and were used to transmit the thermocouple voltage signals from the sliprings to the Omega meter.

As shown in figure 3.7, each pair of brushes was in contact with a slipring, one on each side in order to maintain proper continous electrical connection. The wires connecting pairs of brushes (two for each thermocouple) were connected to the temperature readout through a two way switch. Each brush was attached to a small brass sheet spring , and each set of four springs on one side of the slipring assembly was bolted to a plexiglas holder. The holders were mounted on the base plate of the test section opposite to each other, and an adjustable spring in between the plexiglas holders was used to exert enough pressure to keep the brushes in continuous contact with the sliprings during rotation.

Variations in the steady state wall temperature readings during rotation were within ± 0.1 °C for all rotation rates used in the present experiments. However, additional external pressure on the contact brushes was necessary for the stability of the readings during high rotation, which showed the need for improved design of the brush mounts for future work.

3.2 Flow Visualization Technique

Qualitative observations of the flow field in the rotating enclosure were done utilizing smoke and laser sheet. The technique is widely used in laboratory experiments for the visualization of flow movement in stationary frames of reference. However, utilizing the technique in rotating reference frames is hindered by the complexity of constructing and alligning a set of mirrors capable of simultaneously bending, rotating, and focusing a laser beam on a cylinderical mirror which rotates

with the enclosure.

3.2.1 Fiber Optics Rotating Connection

Figure 3.8 shows a schematic diagram of the flow visualization system used in the present study for making use of fiber optics technology to transmit a laser beam inside the test section during rotation. The system consists of a flexible incoherent fiber optic cable [model 77526, ORIEL Corporation], 0.617 cm in diameter and 121.9 cm in length. As shown in figure 3.9, the cable was constructed of a bundle of glass fibers, 0.32 cm in diameter, which was protected by a non-magnetic interlocking stainless steel sheathing. The ends of the cable were fitted with hard steel ferrules, 1.1 cm in diameter. One end of the cable was mounted axially in a plexiglas holder which was bolted to the back wheel of the test section and was backed by a black insulating cover to protect the back side optical window. The exposed surface of the cable end was positioned perpendicular to and concentric with the axis of rotation, while the other end of the cable was inserted inside the aluminum box of the test section through a small hole in the back wheel.

Inside the test section, the end of the cable was mounted in a Lens-Cable assembly that focused the transmitted laser beam at the axis of a cylinderical lens for generating a sheet of laser light perpendicular to the axis of rotation at the midplane of cavity. The assembly was attached to the body of the test section by aluminum brackets that restrained it from moving during rotation of the test section. The assembly was fitted into the space between the isothermal plates and rode on the back side of the transparent plexiglass wall of the cavity with the cyliderical lens parallel to the axis of rotation.

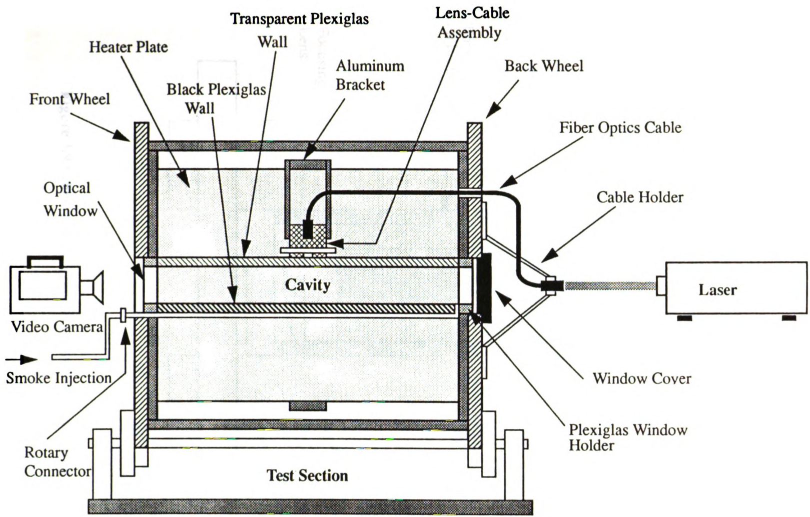

Figure 3.8 Schematic Diagram of Flow Visualization System

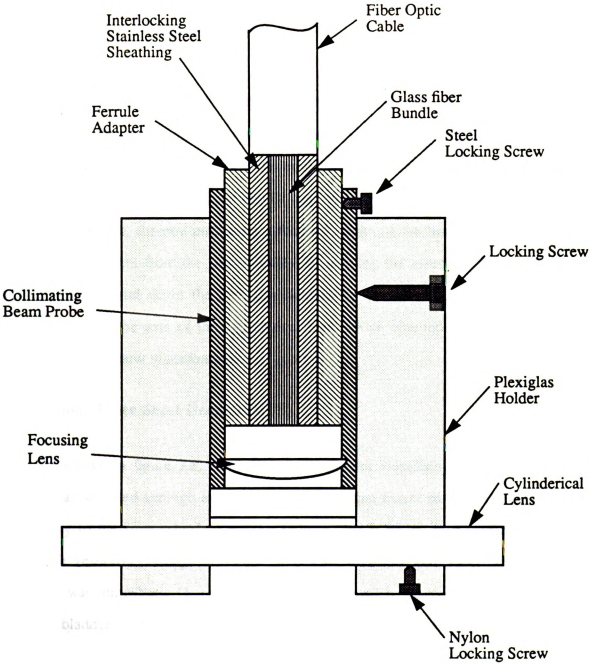

Figure 3.9 Schematic Diagram of Lens-Cable Assembly

The lens-cable assembly shown in figure 3.9 was machined out of a plexiglas block, 5.08x7.62x4.45 cm. The block had a small hole for holding a cylinderical lens 0.64 cm in diameter, and a larger hole perpendicular to the axis of the cylinderical lens for holding a collimating beam probe 1.5 cm I.D. [model 77644, ORIEL Corporation].

The probe tube held an f/1.7 lens (19 mm focal lengt, 11 mm clear diameter) by means of an expanding spring ring. A ferrule attached to the end of the fiber optic cable fit inside the tube, and this cable could then be positioned to set the distance between the surface of the fiber bundle and the probe lens greater than the focal length of the lens, thereby producing a focused image of the laser light at a distance greater than 7.5 cm from the lens. Finally, by moving the assembeled cable end and beam probe up and down the plexiglas holder, the focused image of the laser light was adjusted at the axis of the cylinderical lens, which resulted in the sheet of light required for the flow visualization.

3.2.2 Smoke-Laser Sheet Generation

As shown in figure 3.8, the smoke necessary for visualising the flow inside the cavity was supplied through a small injection tube that extended from the rear end of the cavity to the front wheel of the test section. The injection tube was connected to a smoke reservoir through a rotary connector and a tygon tube. The reservoir pressure was atmosheric (same as the cavity), and was connected by a tygon tube to a small bladder type hand pump that was used to manually deliver small volumes of smoke to the cavity when needed.

An argon ion laser [model 94, LEXEL Corporation] was used to generate a low power beam of light, which could be targeted on the exposed rotating end of the fiber optic cable to generate a light sheet inside the cavity. The light sheet combined with the injected smoke revealed the details of motion of the flow during rotation at the midplane of the cavity, and a video camera connected to a monitor was used for simultaneously observing and recording the flow patterns through the front optical window (See 3.4.2 Photography).

3.3 Mach-Zehnder Interferometer

Interferometry is widely used for non-invasive temperature field measurements in convection heat transfer and aerodynamic studies. The technique is based on the fact that the refractive index of a medium changes as its density changes. Consequently for gases, if the pressure is held constant the complete temperature field, which produces the density changes, can be evaluated. A Mach-Zehnder interferometer was used in the present study because it permits the continous observation of a two dimensional temperature field, and therefore, provides the required temperature as well as heat transfer data during rotation.

ps 12 3.3.1 Interferometer Components

A schematic diagram of the Mach-Zehnder interferometer is shown in figure 3.10 . It basically consists of two beam splitters and two mirrors, which are used to split a collimated beam of light in two different paths. One part continues undisturbed and is called the reference beam, while the other part, called the measuring beam, passes through the test section to be altered by the temperature variations in the beam path. When the two beams are finally recombined, interference fringes result from phase differences between the undisturbed reference beam and the measuring beam.

A 70-Watt high pressure mercury vapor lamp which emits white light was mounted in a lamp housing with a small aperature (about 2 mm) and was used as the interferometer's light source. The white light then passed through a narrow band filter

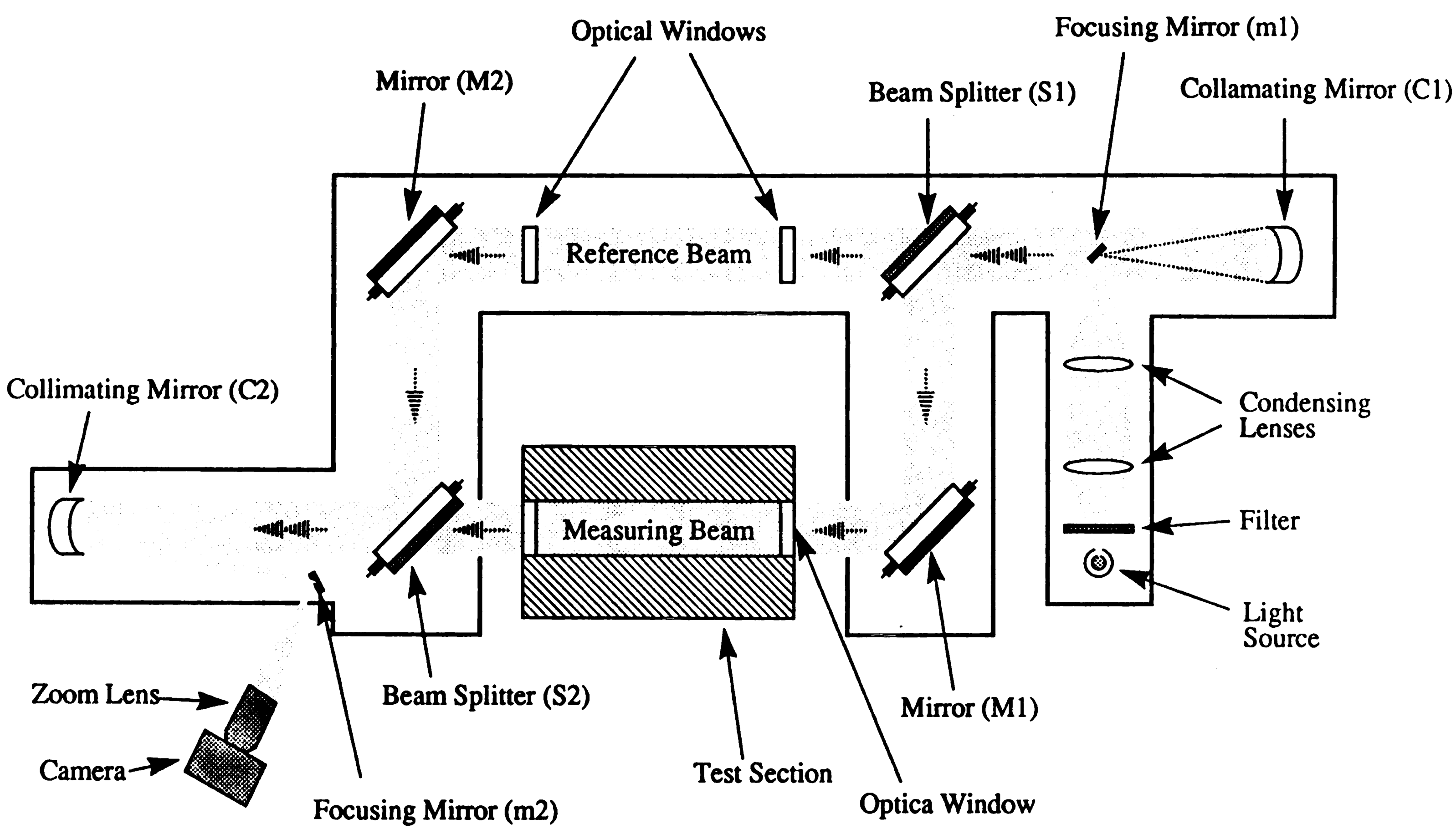

Figure 3.10 Schematic Diagram of Mach-Zehnder Interferometer

which was mounted in front of the light source to select only green light (5461Å). The light then passed through two condensing lenses and was focused on a small mirror (m1) which acted as a near point source at the focal point of a 10.16 cm diameter spherical mirror (C1).

Mirror (C1) reflected a collimated beam of light onto beam splitter (S1), which reflected 50% of the original beam to mirror (M1) and transmited the other 50% through to mirror (M2). The measuring beam was reflected by M1 and passed through the test cavity to beam splitter (S2), which in turn transmited it plus the the beam reflected by (M2) to the spherical mirror (C2). Two optical window plates identical to the ones mounted on the test cavity were placed in the pathway of the reference beam between partial mirror (S1) and full mirror (M2) for compensation.

The measuring and reference beams were combined at mirror (C2) and focused on a small mirror (m2), which in turn focused the reflected image through a large zoom lens onto the picture element of a high shutter speed video camera connected in series to a S-VHS recorder and a high resolution TV monitor.

All optical components were carried on a heavy gauge flat horizontal steel platform supported by rigidly constructed steel tubing legs. Two layers of thick rubber pads and felt cushions were used underneath the legs to minimize the transmision of vibrations from the floor to the optical components.

3.3.2 Alignment and Focusing

Aligning the optical components of the interferometer is a time consuming process that may seem tedious at the beginning, but becomes less complex as detailed pocedures are developed for coarse adjustment of relative positions and fine tuning of individual components. Comprehensive discussion of all important aspects of the basic theory, design and adjustment of a Mach-Zehnder interferometer can be found in Goldstein (1976). However, it is appropriate to discuss the basic principles utilized in the present study.

The main idea is to ensure that (i) the original light beam is bright and collimated, (ii) the reference and measuring beams are closely parallel and their path lenghs are approximately the same, and (iii) the recombined parts of the reference and measuring beams are accurately parallel. In order to do that, all components are placed on the horizontal platform in the arrangement shown in figure 3.10, and all distances and angles are adjusted using accurate measuring tools and light projections and reflections.

The light source, filter and condenser lenses are mounted such that a small bright sharp spot is focused on a small flat mirror (m1). Mirror (m1) is positioned at the focal point of sperical mirror (C1) to ensure that the width of the collimated beam reflected by C1 is constant. This is checked by projecting the beam on a flat screen positioned perpendicular to the beam at increasing distances. The mirrors and beam splitters are then arranged at the the four corners of a rectangle and set at 45° as shown.

The parallelism of the two beams is achieved by, aligning the images of two objects located before (S1) along the original beam and separated by a large distance. The two objects are chosen to be the bright point light source, which is located at infinity, and the boundaries of the small mirror (m1) together with the vertical wire used to suspend it. A small telescope is used to look into beam splitter (S2) to see the images, and the alignment is done by slight rotation of S2 and M2, which are mounted in gimbal mounts that allow for precise tilt about two orthogonal axes.

When the beams are almost parallel, fringes with finite spacing will appear in the recombined beam which is projected on mirror (C2). By further minute rotation of S2 and M2 infinite fringe spacing can be achived, in which case the two beams will be perfectly parallel and the field of view completely iluminated. This mode of operation is called "infinite fringe setting".

In the infinite fringe mode used in this work, density gradients initiated by heat transfer in the test section will result in disturbances in the path lengh of the measuring beam which in turn produce interference fringes that represent lines of constant refractive index or temperature inside the test cavity.

Finally, the image reflected by mirror (C2) is focused at the picture element of a video camera through the small flat mirror (m2). A video camera with high speed shutter [COHU, model 6415] is used to avoid the distortion of fringes by the small vibrations transmitted to the optics. The camera shutter can time each frame up to 1/2000 of a second, which is higher than the frequency of any remaining vibrations in the interferometer system.

3.4 Experimental Procedures

The nature of experimental work does not provide the levels of accuracy and precision required for controlling all involved parameters to obtain exact experimental results. However, several steps were taken before each experimental run to ensure acceptable and known boundary conditions and accurate, repeatable data aquisition. Prescription of the boundary conditions required knowledge of the temperature of the two opposite isothermal walls and elemination of any heat flux to the other two walls. It also required steady rotation about the central horizontal axis at a known rate. The data included accurate measurements of the temperature field and a clear picture of the flow field.

3.4.1 Preparation

Prior to performing an experiment the constant temperature hot water ciculator was set at a temperature slightly higher than required, while the cold water ciculator was set at a temperature slightly lower than required. The hot and cold temperatures were chosen such that their average was close to ambient temperature in order to minimize temperature gradients through the optical windows. The optical windows were covered with insulating foam covers during start up to minimize convective currents which result from heat loss to the surroundings, and water circulation would be started with the heated plates in a vertical position. The stationary enclosure would be left for 3 to 4 hours and then would be rotated for at least another 1½ to 2 hours until wall temperatures reached steady state. Steady state temperature was defined when the variation of the temperature of each wall would not exceed ± 0.1° C over a period of 15 to 20 minutes. The wall temperature was measured using a representative thermocouple from each wall connected to the Omega digital readout as explained previously in this chapter. The rotation rate was counted and timed several times using a stop watch, and an average was taken.

To perform the flow visualizations during rotation, the laser was triggered, a steady beam of light was targeted on the exposed end of the fiber optic cable, and then the smoke reservoir was connected to the injection tube through the rotary connector. The cover of the front optical window was removed, a small amount of smoke was injected, and the flow motion inside the rotating cavity was recorded on video tape for 2 to 3 minutes. The exposed end of the fiber optic cable and the rotary water coupler were both mounted on the back wheel of the test section, which resulted in a black field of view in the cavity every time the tubes connected to the coupler intercepted the laser beam. The blackout of the flow field occured over an angle of less than 15° while the flow patterns were visible for the rest of the cycle.

In the interferometry experiments, the test section was positioned inside the interferometer prior to starting water circulation, and the interferometer was adjusted for the infinite fringe mode. The optical windows were then covered and water circulation started in the stationary enclosure as described above. After 3 to 4 hours the window cover would be removed, and the fringe pattern checked. Since the walls were isothermal, fringes near the walls must be parallel to them. However, small temperature gradients in the optical windows resulted in slight deviations, which required minor adujstment of mirror (M2) and/or beam splitter (S2) in order to correct the fringe orientation. Then the windows were covered and steady rotation was held for at least 1 hour. After the wall temperatures again reached steady state (typically o.2 °C less than the stationary steady state temperature) the window covers were removed and the fringe patterns were recorded on video tape for 2 to 3 minutes of rotation.

3.4.2 Photography

Flow visualization and interferometry experiments were recorded on S-VHS video tapes using a MITSUBISHI twin digital U-70 VCR. The video tapes were played back in single frame mode and displayed on a Panasonic model WV-5410 high resolution monitor. The best frames at the desired angles of rotation were photographed off the monitor using a 35 mm still camera loaded with a 400 ASA color film. The analysis of the interferograms was done on an X-Y traveling microscope built by GAERTNER SCIENTIFIC Corporation with resolution up to 0.0001 inch.

CHAPTER 4

RESULTS AND DISCUSSION

4.1 Flow Field, Temperature Field, and Nusselt Number

The experimental results of this study are presented in the form of flow visualizations, isotherms and local and mean Nusselt numbers at instantaneous angles during rotation of the air filled differentially heated square enclosure. The flow pictures obtained using smoke and laser light represent the streak lines and are used for the qualitative analysis of the enclosure convective currents, while the isotherms obtained using a Mach-Zehnder interferometer show the entire temperature field and are used to calculate the tempereature gradients at the isothermal walls. The local Nusselt numbers are derived from the wall temperature gradients as described in Appendix (B).

The quantitative results in the form of local Nusselt number distributions along the isothermal walls and mean Nusselt number values are used to determine the suppression or enhancement of heat transfer as a function of the increasing speed of rotation. The mean Nusselt numbers were calculated by integrating the local Nusselt number values over the height of the isothermal wall. Both flow visualization and interferometry experiments were recorded in real time mode on S-VHS video which allows the storage of 60 frames every second, i.e. one picture every 2°-12° of the enclosure rotation for rotational rates of 20-120 rpm respectively. This makes available a large volume of preprocessed information which can provide a comprehensive data base, however the time consuming method of reading the interferograms makes it difficult to analyze every single one of them. In addition the periodic nature of the problem allowed for the selection of fewer angular positions for data reduction at every rotational speed. Four angular positions were chosen because of their relevance to a great deal of the existing literature on rectangular enclosures. These four positions are 0° which represents the case of the enclosure heated from above, 90° which represents the case of a vertical enclosure heated from the left side, 180° which represnts the case of the enclosure heated from below, and 270° which again represents the vertical enclosure but heated from the right side. In some cases however data at the angular position of 180°or 90° could not be obtained because the field of view was obstructed by the tubes connected to the rotary water coupler. Note that the overall mean Nusselt number at a certain rotational speed represents the average of the mean Nusselt number values at these selected angular positions.

In this study the data is presented as a function of Taylor number $6.34\times10^5 \leq Ta \leq 1.75\times10^7$, the rotational Rayleigh number $5.3\times10^3 \leq Ra_r \leq 1.4\times10^5$, and Rayleigh number $Ra = (1.77\pm0.07)\times10^5$. These parameters correspond to rotational rates of 22.5 $rpm \leq \Omega \leq 118.0$ rpm and a temperature difference between the isothermal walls of $(T_H-T_C) = 13.3\pm0.5$ °C.

Although the above parameters can be used to predict the individual effects of the gravity and rotational forces on the enclosure flows, the combined effect of these forces plus the inertial and viscous shear forces in a particular enclosure configuration can not be directly forseen. Therefore the present study was necessary to reveal the effect of the interaction of these forces on the flow and hence the convection heat transfer in a rotating enclosure. And the simple model of the differentially heated square cavity was selected for its wide use in the literature on natural convection in enclosures. Most of the published studies on rotating enclosures however deal with different configurations and orientations with respect to the gravity vector. In addition to the experimental results of the prsent study the numerical calculation of the same problem done by K.T. Yang of University of Notre Dame (1990) is presented in some cases for the purpose of correlation. This numerical algorithm is based on the governing equations (2.21)-(2.23) and utilizes the QUICK (quadratic upstream interpolation for convection kinematics) finite difference scheme to calculate the velocity field, the temperature field and the Nusselt number among other variables. See H.Q. Yang (1986) for further details on the numerical algorithm.

In the case of a vertical stationary enclosure differentially heated from the sides, gravitational buoyancy produces circular fluid motion near the boundaries while the slower fluid in the core region plays a small role in the convection process. As the enclosure is tilted toward the heated from below position instability of the core region enhances the mixing of the fluid and thereby the heat transfer. On the other hand, as the enclosure is tilted toward the heated from above position the fluid becomes more stratified and the heat transfer drops until the process becomes dominated by conduction.

In the present study the square enclosure of aspect ratio Ax=1.0 rotates in the clockwise direction about the horizontal *Z–axis* at steady rates, which induce uniform rotational buoyancy forces. However when these forces interact with the periodic gravity field they result in unsteady complex flow patterns. At slow rotation rates gravity is expected to dominate the motion of the fluid with primary cellular flow near the walls of the enclosure. In addition the Coriolis force recirculates the boundary region fluid toward the core region and therefore improves the mixing of the fluid and enhances the heat transfer. As the speed of rotation increases the centrifugal force and the wall shear are expected to have increased influence, where the viscous shear migrating inward from the wall works to produce solid body rotation and reduce the heat transfer to pure conduction in air, while the centrifugal buoyancy works to produce symmetric flows relative to the rotating coordinate system and therefore increase the convective heat transfer. In the following subsections the flow patterns which result as the speed of rotation increases are presented, and their influence on the temperature field and the Nusselt number distribution is discussed. Estimates of the errors associated with data acquisition and reduction are presented in Appendix (C).

4.1.1 At Rotational Speed 22.5 rpm

Parts (b) and (c) of figures 4.1 through 4.3 show the resulting isotherms and local Nusselt number distributions at rotational speed Ω=22.5 *rpm* (Ta=6.34×10^5, Ra=1.84×10^5, and Ra_r=5.3×10^3) for the angular positions of, 2° (heated from above), 270° (vertical), and 182° (heated from below) respectively. Flow pictures at the same rotation rate are not available, however, flow pictures at rotation rates of 17.0 rpm and 28.5 rpm for the corresponding angular positions are shown in part (a) of the aforementioned figures to help predict the flow patterns at 22.5 rpm. Figure 4.1a shows the flow pattern when the hot wall is on top during clockwise rotation. The pictures show the counter rotation of the core region fluid while the fluid near the isothermal walls forms a slower boundary layer and clockwise rotating vortices at the four corners. It can also be observed that the core fluid is being well mixed which agrees with the nearly uniform temperature in the midsection of the enclosure shown in figure 4.1b. The isotherms of figure 4.1b also show the thickness of the boundary layer and the vortical motion at the lower corner (L.H.S.) of the hot wall and the opposite corner on the cold wall. It is also clear from the interferogram the existance of thermal gradients at the plexiglas walls which shows that they are not perfectly insulated. In figure 4.1c the local Nusselt number is plotted vs. the non-dimensional height of the isothermal walls [Y^*=(2Y+H)/2H],

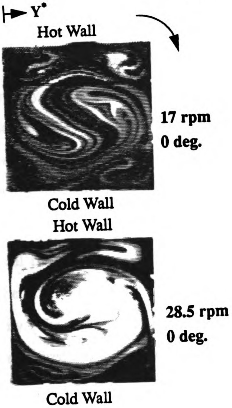

(a) Flow Field

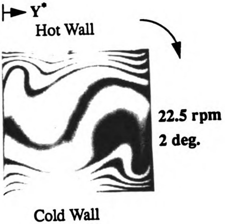

(b) Temperature Field

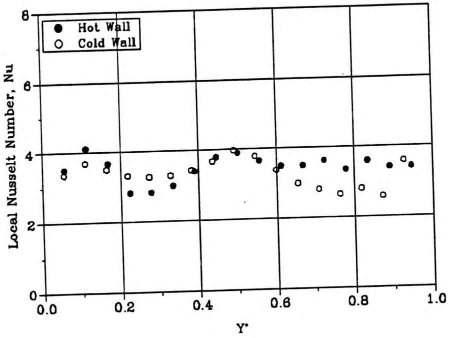

(c) Ω=22.5 rpm, Ra=1.84x10^6
ϕ=2° (heated from above)
[Picture 6]

Figure 4.1 Effect of Rotational Speed of 22.5 rpm at ϕ = 0 degrees, Ta = 6.34x10^5

where $Y^*=0$ is at the lower end of the walls when the hot wall is on the left and the cold wall is on the right. In this case the Nusselt number distribution is symmetric and nearly uniform, however a mean value of 3.1 is significantly higher than that of the stationary enclosure heated from above (approximately 1.0) ,which can be related to the rotation induced mixing of the core region, which would otherwise be formed of nearly stagnant layers of stratified fluid.

As can be seen from figure 4.2a, as the hot wall rotates clockwise toward the vertical position ($\phi=270°$) the boundary layer thickens and the corner vortices move up the hot wall (toward $Y^*=0.0$) and down the cold wall (toward $Y^*=1.0$) because of gravity. The core region is squeezed, and a review of the video tape shows it to reverse direction and rotate with the enclosure. The isotherms in figure 4.2b also show the increase in the boundary layer thickness and the increased non uniformity of the core region temperature. The influence of the gravitational buoyancy is apparent in the local Nusselt number profiles shown in figure 4.2c, where the local Nusselt number reaches a minimum near the lower end of the hot wall and a maximum near the upper end, while the cold wall exhibits a reversed distribution. The mean Nusselt number however remains almost unchanged from that of the previous angular position ($\phi=0°$).

Figure 4.3a shows the flow pattern at angular position $\phi=182°$ when the enclosure reaches the heated from below position. The vortices are released from the opposite corners and driven toward the core by the Coriolis force which greatly enhances the mixing of the core fluid and therefore enhances the convection heat transfer. The isotherms in part (b) also show the large thermal gradients at the isothermal walls and at the core region. Note the inverted bell shape of the local Nusselt number distributions with a maximum near mid-wall and minimum values near the corners. This is attributed to the formation of new vortex tubes near the four corners which replace the ones swept to the core.

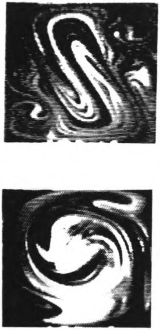

(a) Flow Field

(b) Temperature Field

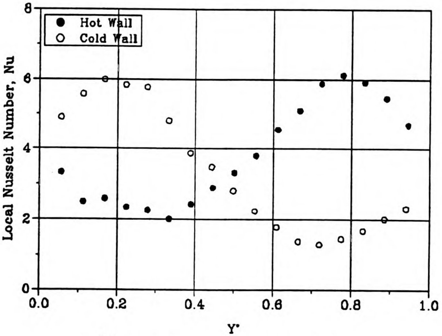

(c)

Ω=22.5 rpm, Ra=1.84x10^{5}
ϕ=270° (vertical enclosure)
[Picture 1]

Figure 4.2 Effect of Rotational Speed of 22.5 rpm at ϕ= 270 degrees, Ta = 6.34x10^5

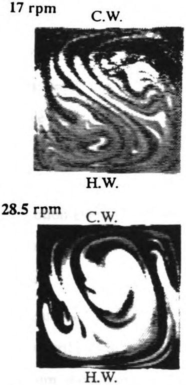

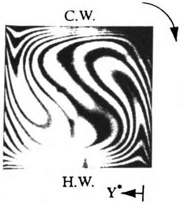

(b) Temperature
Field at ϕ = 182 deg.
22.5 rpm

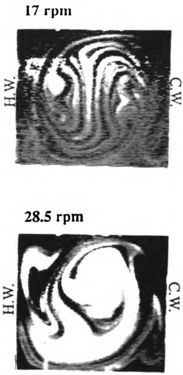

(a) Flow Field at ϕ = 182 deg.

(d) Flow Field at ϕ = 90 deg.

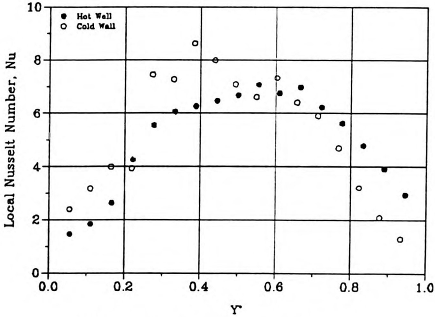

(c) Ω=22.5 rpm, Ra= 1.84×10^6
ϕ=182° (heated from below)
[Picture 4]

Figure 4.3 Effect of Rotational Speed of 22.5 rpm at ϕ = 182 degrees, Ta = 6.34×10^5

The mean Nusselt number reaches a high of 4.64 which reflects more than 50% increase over the previous angular position.

At ϕ=90° the interferogram and the local Nusselt number distributions are not available because of reasons explained at the beginning of this chapter, but the flow pictures of figure 4.3d show the initiation of the counter rotation of the core region and the growth of the secondary vortical flow at the four corners. This pattern of fluid motion eventually develops during the rest of the cycle untill the enclosure once again reaches the heated from above position, then the same sequence of events is repeated.

Figure 4.4 shows the effect of the angular position (orientation of the hot wall) on the distribution of the mean Nusselt number in one cycle of the enclosure rotation. The figure shows good agreement between the experimental mean Nusselt numbers and the numerical calculation of K.T. Yang (1990). The largest difference between both seems to be at 270° where the calculated value at the hot wall is about 16% less than the experimental value, but it is clear that the trend is the same. The sinusoidal behavior shown in this figure illustrates the influence of the gravitational buoyancy at 22.5 rpm (Ta=6.34×10^5), where the mean Nusselt number reaches its maximum in the vicinity of the heated from below position (ϕ=180°). The figure also shows the deacrease in the mean Nusselt number near ϕ=270° or when the relative velocity of the buoyant fluid near the isothermal walls becomes small. This also explains the significant increase in the mean Nusselt number at the opposite vertical position (ϕ=90°) where the relative fluid velocity at the wall is expected to be higher.

4.1.2 At Rotational Speed 32.0 rpm

Figures 4.5 through 4.8 illustrate the flow and temperature fields at rotational speed of 32.0 rpm (Ta=1.28×10^6 , Ra=1.72×10^5, and Ra_r=1.0×10^4). At the heated from above position (ϕ=0°) the counter clockwise rotation of the core region can still

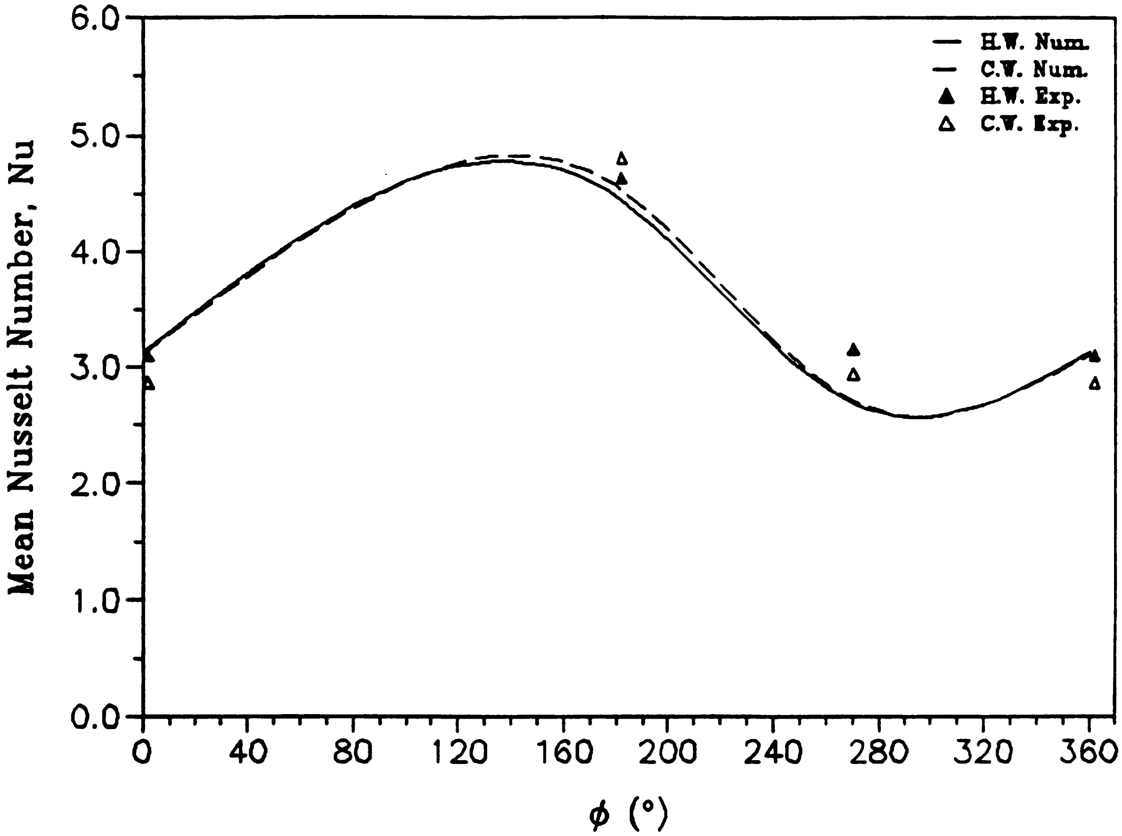

Figure 4.4 Mean Nusselt Number vs. Angular Position at 22.5 rpm, Ta=6.34x10^{6}, Ra=1.84x10^{6}

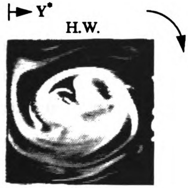

(a) Flow Field

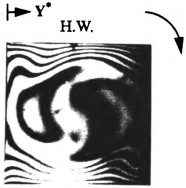

(b) Temperature Field

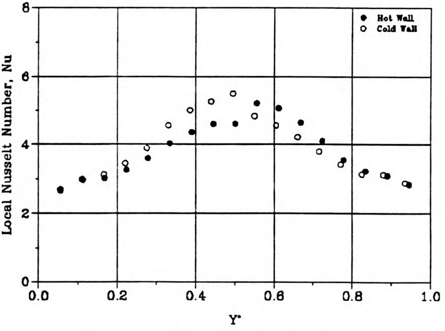

(c) Ω=32 rpm, Ra=1.72×10^6
ϕ=0° (heated from above)
[Picture 7]

Figure 4.5 Effect of Rotational Speed of 32 rpm at ϕ = 0 degrees, Ta = 1.28×10^6

be seen in figure 4.5a, however the velocity of the core fluid relative to the enclosure seems to be less than that of the slower angular speed of 28.5 rpm (comparing the real time motion on the video tape). The boundary layer and the corner vortices can still be seen too, with no notable change in their sizes. Some change can be recognized in the isotherm structures of figure 4.5b when compared to those of the corresponding angular position at 22.5 rpm. It can be seen that the thermal boundary layer is thiner in the middle region and thicker near the edges of both isothermal walls which leads to increased heat transfer near the center of the wall and decreased heat transfer near the corners. The figure also shows that the core region is composed of two counterrotating cells. Figure 4.5c shows the distribution of the local Nusselt number which conforms with the shape of the thermal boundary layer where the local Nusselt numbers are significantly higher near mid-wall, with approximately 15% increase in the mean Nusselt number over that at 22.5 rpm.

At $\phi=270°$ (vertical position) the flow picture of figure 4.6a shows slight increase in the boundary layer thickness, it also indicates less mixing of the core region fluid which suggests decreased influence of the Coriolis force. It is important to note here that the viscous shear forces at all four walls stretch the corner vortices in a clockwise motion despite the gravitational buoyant force that works to impose a counterclockwise circulation on the boundary layer flow. This flow pattern shows the increased influence of the shear forces which work to reduce the relative velocity between the boundary layer fluid and the wall and therefore is expected to reduce the convection heat transfer. The motion of the core region also confirms the increase in the shear forces, where the fluid continues to rotate counterclockwise as it did at slower angular speeds but at a slower and more uniform fashion. In the mean time the isotherms of figure 4.6b show a generally more uniform and thicker thermal boundary layer and a nearly isothermal core region. The predicted drop and uniformity of the heat transfer is illustrated in figure 4.6c, where the amplitude of the

(a) **Flow Field at ϕ = 270 deg.**

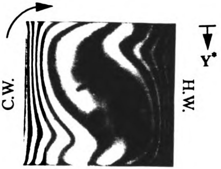

(b) Temperature Field at ϕ = 270 deg.

(d) Flow Field at ϕ = 180 deg.

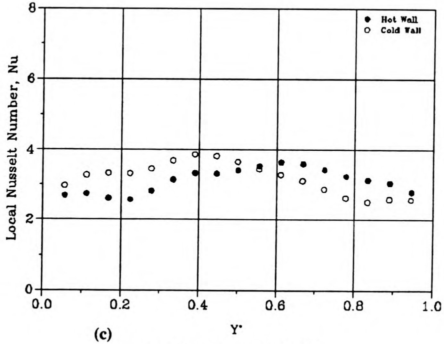

(c)

Ω=32 rpm, Ra=1.72×10^{6}
ϕ=270° (vertical)
[Picture 8]

Figure 4.6 Effect of Rotational Speed of 32 rpm at ϕ = 270 degrees, Ta = 1.28×10^{6}

sinusoidal shape of the local Nusselt number distribution is less than that of the corresponding angular position at 22.5, rpm and the maxima and minima are closer to the center of the isothermal walls. The mean Nusselt number is approximately 19% less than that of the previous ϕ=0° position, and 11% less than that of ϕ=270° at 22.5 rpm.

Figure 4.7a shows the flow pattern as the enclosure reaches the opposite vertical position (ϕ=91°). At this position the relative velocity of the flow along the isothermal walls is enhanced by the aiding gravitational buoyancy, and the wall fluid is swept toward the core more rapidly, while the core region fluid continues to rotate counterclockwise thereby enhancing the slushing action of the fluid and consequently the convection process. Figure 4.7b shows the steep thermal gradients near the walls and the wraping around of the thermally stratified fluid which agree with the flow pattern and gives indication to a significant increase in the convection heat transfer. The local Nusselt number distribution of figure 4.7c shows the remarkably high values of the bell shaped curve at both the hot and cold walls compared to the opposite vertical position (ϕ=270°) which illustrate the combined influence of the shear forces and the assisting gravitational buoyancy. In addition, the shift of the maximum values toward the center of the walls is a direct result of the swirling motion induced by the Coriolis force. It is therefore reasonable to conclude that the heat transfer at that angular position is the maximun during the cycle since the wall shear, the gravitational buoyancy and the Coriolis force are all in favor of the convective currents. This is illustrated in figure 4.8 by an increase in the mean Nusselt number of approximately 91% over that of the ϕ=270° position and 55% over that of the ϕ=0° position. Also note that as shown in figure 4.8 the mean Nusselt number at the heated from above position (which is usually the lowest value during the cycle in slow angular speeds) is higher than the mean Nusselt number at the vertical position ϕ=270°, which shows a phase shift that result from increasing

(a) Flow Field at ϕ = 90 deg.

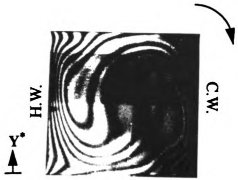

(b) Temperature Field at ϕ = 91 deg.

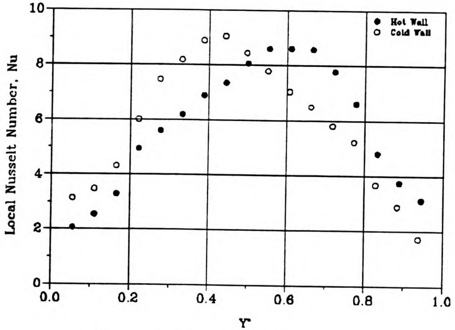

(c) Ω=32 rpm, Ra=1.72x10^6
ϕ=91° (vertical)
[Picture 8a]

Figure 4.7 Effect of Rotational Speed of 32 rpm at ϕ = 90 degrees, Ta = 1.28x10^6

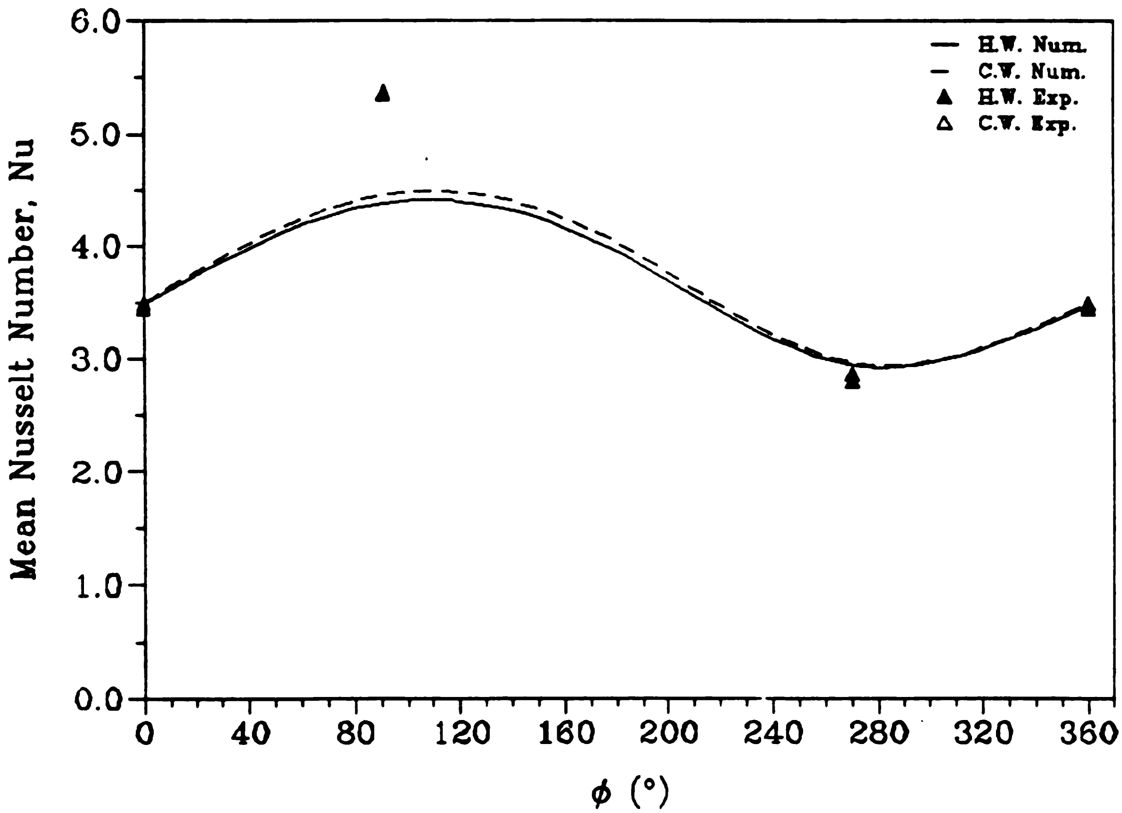

Figure 4.8 Mean Nusselt Number vs. Angular Position at 32 rpm, Ta=1.28×10^{6}, Ra=1.72×10^{5}

the rotation rate. The same behavior is also shown in the numerical results, however at ϕ=90° the numerical prediction is not as high as the experimental result.

4.1.3 At Rotational Speed 38.0 rpm

At 38 rpm (Ta=1.81×10^6) the picture of the flow in the heated from above position (ϕ=0°) shown in figure 4.9a reveals a rather indistinct flow pattern. Fluid rotation can barely be seen near the center of the enclosure while the relative velocity of the fluid near the walls is very small. This flow pattern suggests a state of quasi-balance between two or more of the buoyant and the retardant forces, and based on the observations discussed above for the angular speed of 32 rpm it is reasonable to say that the dominant forces in this balance are the gravitational buoyancy and the viscous shear migrating inward from the enclosure walls. Furthermore the low velocities in the core and the nearly stagnant fluid near the walls suggests a drop in the heat transfer which is also supported by the temperature field of figure 4.9b. The isotherms show nearly flat layers of thermally stratified fluid and little mixing in the core region, however the influence of gravity can still be seen in the nonuniform shape of the thermal boundary layer. A drop in the heat transfer with the increase in the angular speed can be seen when comparing the distriution of the local Nusselt number of figure 4.9c to that of figure 4.5c for the angular speed of 32 rpm. The minimum values near the corners are slightly lower, while the maxima near the center of the walls are significantly less than those of 32 rpm. This reflects a decrease in the mean Nusselt number of approximately 28%.

Review of the real time fluid motion recorded on the video tape shows periodic motion of the core region relative to the enclosure walls, where the fluid is streched in a tube like shape between two opposite corners as the hot wall moves from top to bottom then the tube is bent in an S-shaped curve during the other half of the cycle. Figure 4.10a shows the flow field as the enclosure reaches the vertical position

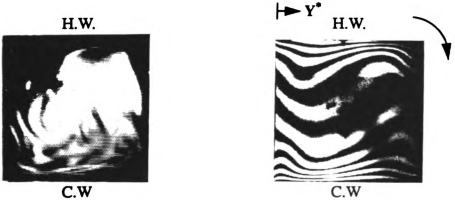

(a) **Flow Field** (b) **Temperature Field**

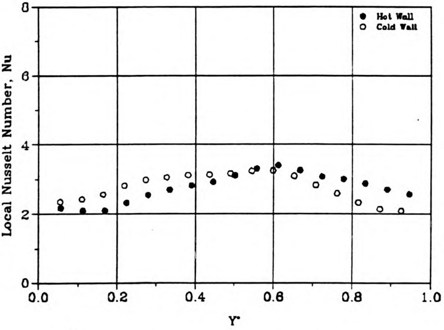

(c) $\Omega=38$ rpm, $Ra=1.84\times10^{5}$
$\phi=0°$ (heated from above)
[Picture 13]

Figure 4.9 Effect of Rotational Speed of 38 rpm at ϕ = 0 degrees, Ta = 1.81×10^{6}

(a) Flow Field

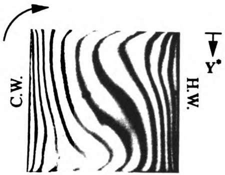

(b) Temperature Field

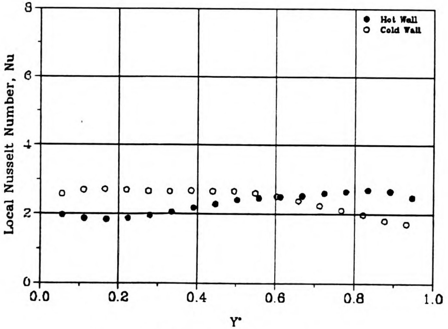

(c) Ω=38 rpm, Ra=1.84x10^{6}
ϕ=270° (vertical)
[Picture 12]

Figure 4.10 Effect of Rotational Speed of 38 rpm at ϕ = 270 degrees, Ta = 1.81x10^6

(ϕ=270°), where the flow pattern near the enclosure walls remains indistinct and slow and its shape is almost unchanged from the previous angular position (ϕ=270°) while the fluid in the core starts to stretch. Moreover, the isotherms and local Nusselt number distributions of figures 4.10b&c also match those of the previous angular position of ϕ=0°, with approximately 12% decrease in the mean Nusselt number. This suggests that the shear forces during this half of the cycle (the hot wall rotating clockwise from top to bottom) balance the gravitational buoyancy and suppress the convection heat transfer.

The effect of gravity however shows in the next figure (4.11) at the opposite angular position (ϕ=88°) when both the gravitational buoyancy along the isothermal walls and the shear forces act in the same direction. The mixing of the core region fluid can be detected in the flow picture of figure 4.11a and its effect can be clearly demonstrated in the shape of the thermally stratified fluid layers of part (b). Figure 4.11c shows the local Nusselt number distributions which are therefore expected to be higher than those of the other two positions presented above at the same angular speed (figures 4.9 and 4.10). As expected the mean Nusselt number at this angle (ϕ=88°) shows 64% increase over that of the heated from above position (ϕ=0°), and 87% increase over that of the opposite vertical position (ϕ=270°). Also note that these distributions along the isothermal walls are opposite and identical, with their minima near the corners as a result of the low relative fluid velocities and the disappearance of secondary corner flows, and their maxima shifted away from the centers of the walls indicating a decline in the influence of the Coriolis force.

The observations and discussion in this subsection show that the rotation speed of 38 rpm (Ta=1.81×10^6, Ra=1.84×10^5, and Ra_r=1.5×10^4) marks a transition region in the interaction of gravitational and rotational forces. A transition from well defined primary and secondary enclosure flows dominated by the gravity effects and Coriolis acceleration throughout the cycle at lower angular speeds, to another region

(a) Flow Field at ϕ = 90 deg.

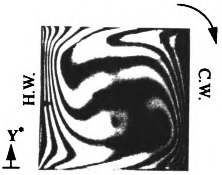

(b) Temperature Field at ϕ = 88 deg.

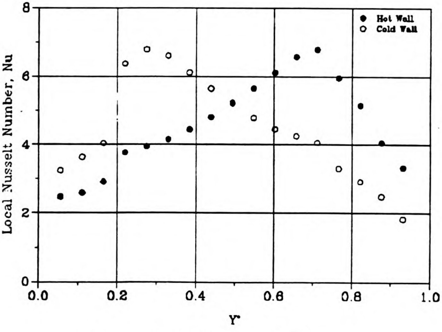

(c) Ω=38 rpm, Ra=1.84x10⁵ φ=88° (vertical) [Picture 12a]

Figure 4.11 Effect of Rotational Speed of 38 rpm at ϕ = 88 degrees, Ta = 1.81×10^{6}

dominated by shear forces that tend to induce solid body rotation and suppress the heat transfer to near pure conduction independent of the angular position. However, figure 4.12 shows that at 38 rpm gravity still has a significant effect on the mean Nusselt number, especially at $\phi=90°$ where it reaches a relatively higher value. Nevertheless, the overall mean Nusselt number is 26% less than that of angular speed 32rpm, which shows the increasing effect of the shear forces. The numerical results shown in figure 4.12 however illustrate more uniformity and earlier independence of the angular position than the experimental results.

4.1.4 At Rotational Speed 47.0 rpm

The preceding discussion seems to suggest that the boundary layer thickness will increase with the angular speed until the entire enclosure fluid rotates as a solid body and the local and mean Nusselt numbers become equal to a value of one which correspond to pure conduction. But interestingly enough, the influence of the centrifugal force begins to show in the form of a non-boundary layer, 2-cell type, buoyant flow that works to enhance the convection heat transfer. Figures 4.13 through 4.17 will illustrate the interaction of the centrifugal buoyancy with the dominant shear forces at $\Omega=47rpm$ ($Ta=2.77\times10^6$, $Ra=1.71\times10^5$, and $Ra_r=2.14\times10^4$).

An interesting flow pattern is shown in figure 4.13a at the angular position $\phi=358°$ (*or* $\phi=-2°$). The streak lines form two cells, a dominant cell which occupies more than ¾ of the enclosure and contains two vortical structures which possess very little circulation, and a smaller cell located at the lower end of the cold wall which seems to be so stagnant that the smoke does not penetrate into it. This type of fluid motion which can be characterized as potential flow in addition to the uniformly spaced isotherms of figure 4.13b indicate continued decline in the corresponding Nusselt number values. Part (c) shows the local Nusselt number distributions which conform with the flow and temperature fields. Note that the distributions along the

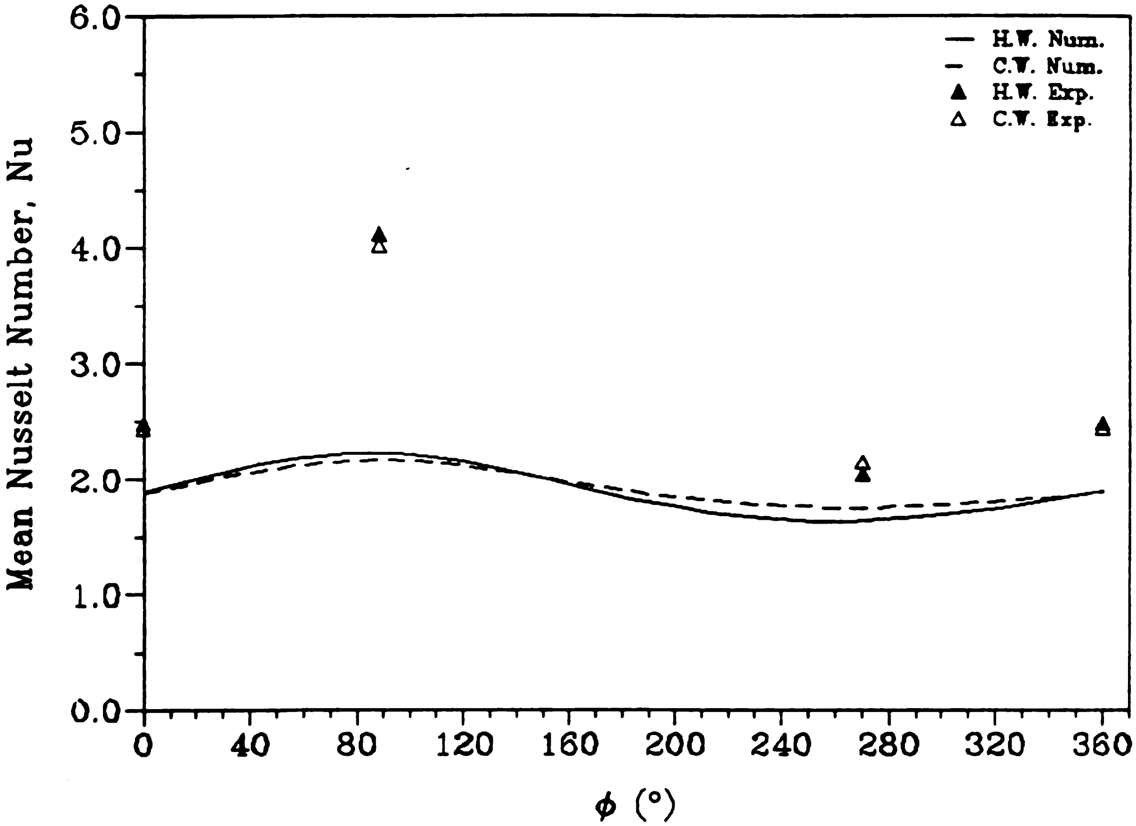

Figure 4.12 Mean Nusselt Number vs. Angular Position at 38 rpm (cw rotation), $Ra=1.84\times10^6$ **$Ta = 1.81\times 10^6$**

H.W.

C.W.

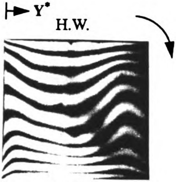

C.W.

(a) Flow Field at ϕ = 0 deg.

(b) Temperature Field at ϕ = 358 deg.

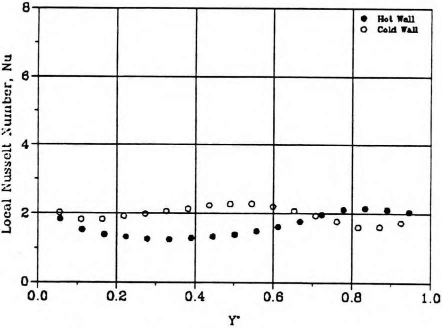

(c) Ω=47 rpm, Ra=1.71x10^5
ϕ=358° (heated from above)
[Picture 21]

Figure 4.13 Effect of Rotational Speed of 47 rpm at ϕ = 0 degrees, Ta = 2.77x10^6

isothermal walls are no longer mirror images of each other due to the asymmetric nature of the flow field. Also note the uniform shape of the curves and the low Nusselt numbers which approach unity near mid-section of the hot wall. It should be noted here that the mean Nusselt number of the cold wall is about 19% higher than that of the hot wall. This is explained by the fact that the conductivity of the plexiglass walls is higher than that of the contained air which result in a higher heat flux at the cold wall (heat flux in the plexiglas is estimated to be approximately twice that in air). Therefore the mean Nusselt numbers of the hot wall will be used for comparison throughout the text. And as expected the mean Nusselt number for this angular position (heated from above) is found to be 42% lower than that of the corresponding angular position at Ω=38*rpm*.

A comparison between, parts (a), (b) and (c) of figure 4.13, and those of figures 4.14, 4.15 and 4.16 shows very little change in the flow and isotherm patterns throughout the cycle, and slight redistribution of the local Nusselt number values along both isothermal walls. The only difference that can be seen in the flow pictures (more recognizable on the video tape) is the change in the shape of the smaller cell at the lower end of the cold wall which becomes elliptic as the hot wall moves from bottom to top (ϕ=180° to 0°) and takes a more circular shape during the second half of the cycle. This small oscillating motion and also the little change in the local Nusselt number distribution from one angular position to the other indicate that gravity has little influence on the covection process at this speed. Finally, comparing figure 4.17 with figure 4.12 it becomes obvious that the mean Nusselt number values at the current angular speed are almost independent of the angular position with an overall mean Nusselt number of 1.487 , which is almost 50% lower than that of 38 rpm but still higher than unity. The largest drop in the mean Nusselt number however occurs at ϕ=90° where the traditionally higher value decreases by about 60%. This indicates that the viscuous shear forces have overcome the

(a) Flow Field at ϕ = 270 deg.

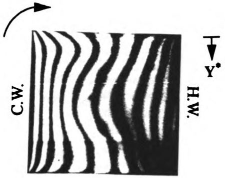

(b) Temperature Field at ϕ = 268 deg.

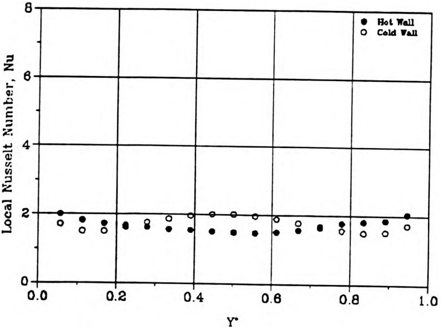

(c) Ω=47 rpm, Ra=1.71x10^5
ϕ=268° (vertical)
[Picture 19]

Figure 4.14 Effect of Rotational Speed of 47 rpm at ϕ = 270 degrees, Ta = 2.77x10^6

(a) Flow Field

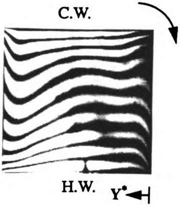

(b) Temperature Field

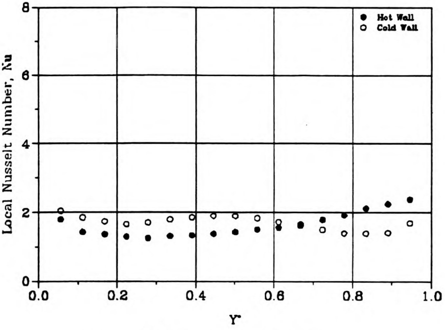

(c) Ω=47 rpm, Ra=1.71x10^5
ϕ=180° (heated from below)
[Picture 18]

Figure 4.15 Effect of Rotational Speed of 47 rpm at ϕ = 180 degrees, Ta = 2.77x10^6

(a) Flow Field at ϕ = 90 deg.

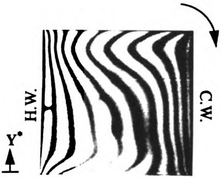

(b) Temperature Field at ϕ = 91 deg.

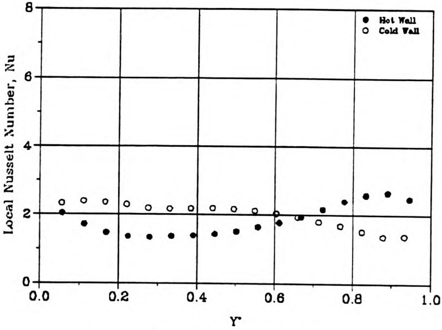

(c) Ω=47 rpm, Ra=1.71x10^{5}
ϕ=91° (vertical)
[Picture 20]

Figure 4.16 Effect of Rotational Speed of 47 rpm at ϕ = 90 degrees, Ta = 2.77x10^{6}

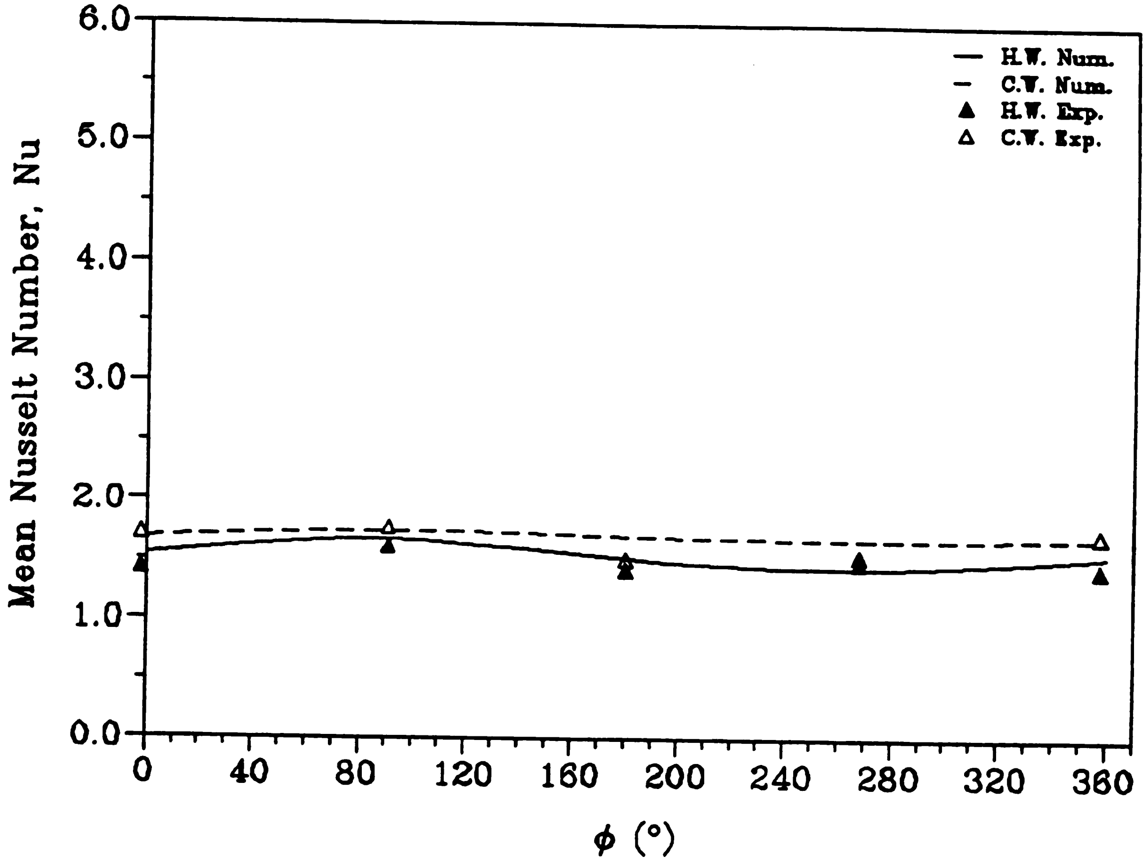

Figure 4.17 Mean Nusselt Number vs. Angular Position at 47 rpm (cw rotation), $Ra=1.71\times10^6$

$Ta = 2.77\times10^6$

influence of gravity throughout the cycle and that the periodic nature of the flow field has become insignificant. This also marks the transition to a new flow regime where the centrifugal buoyancy works to re-establish the convection heat transfer. Again at Ω=47*rpm* the numerical prediction are in excellent agreement with the experimental results as shown in figure 4.17.

4.1.5 At Rotational Speed 53.0 rpm

At Ω=53*rpm* ($Ta=3.52\times10^6$, $Ra=1.83\times10^6$, and $Ra_r=2.92\times10^4$) the slow quasi-steady motion seen at 47 rpm continues to dominate the flow. In figure 4.18a the flow field at $\phi=0°$ looks the same as that of figure 4.13a, however the video tape shows less oscillation in the shape of the small cell, and a larger area of stagnation at the center of the larger cell. The temperature field and the local Nusselt number distributions of parts (b) and (c) are almost identical to those of figure 4.13 too, with less than 5% decrease in the mean Nusselt number which lies within the experimental error margin. Note that the isotherms of figure 4.18b show increased outward fluid motion from the mid region of the hot wall. Figure 4.18 also shows the numerically predicted temperature field, where the isotherms are almost identical to those of the experiment. An agreement that is also illustrated in the local Nusselt number distributions of figure 4.18c, however, the drop of the numerical values near the middle of the hot wall below one (pure conduction) may indicate some error in them.

At figure 4.19 the flow field is shown to be identical to that of figure 4.18, while the isotherms are more symmetric and so are the local Nusselt number distributions. The numerical prediction is again in good agreement with the experiment but the Nusselt number profile is not as symmetric and the local values are slightly lower near the lower end of the hot wall. Figures 4.20 and 4.21 also show the stable flow field which is identical to those of figures 4.18 and 4.19, howevere, the flow fields and Nusselt number profiles at these positions ($\phi=180°$, and92°) show some change

(a) Flow Field
(experimental)

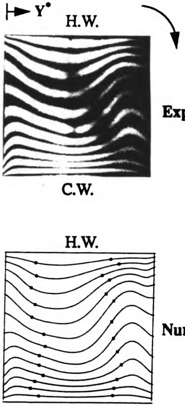

(b) Temperature Field

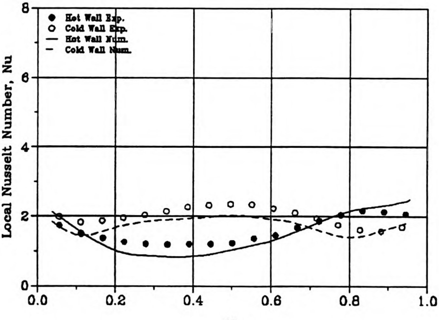

(c) Ω=53 rpm, Ra=1.83x10^6
ϕ=0° (heated from above)
[Picture 24]

Figure 4.18 Effect of Rotational Speed of 53 rpm at ϕ = 0 degrees, Ta = 3.52x10^6

(a) Flow Field
(experimental)

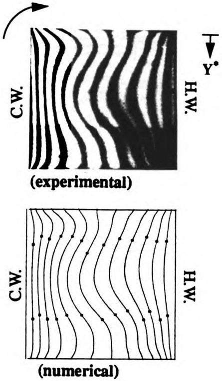

(b) Temperature Field

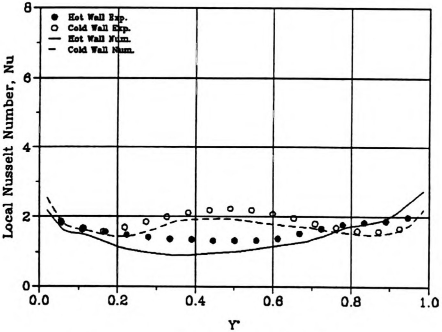

(c) Ω=53 rpm, Ra=1.83x10^5
ϕ=270° (vertical)
[Picture 23]

Figure 4.19 Effect of Rotational Speed of 53 rpm at ϕ = 270 degrees, Ta = 3.52x10^6

C.W.

H.W.

(a) Flow Field
ϕ = 180 deg.
Experimental

C.W.

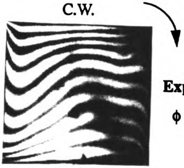

H.W.

Y* ◄┤

C.W.

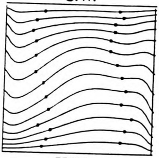

H.W.

Experimental
ϕ = 177 deg.

Numerical
ϕ = 180 deg.

(b) Temperature Field

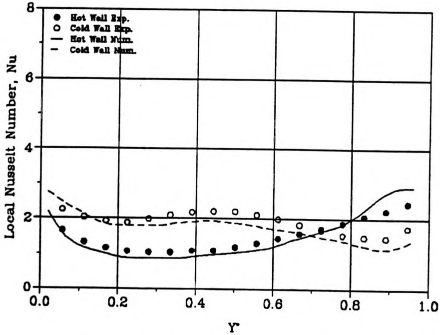

(c) Ω=53 rpm, Ra=1.83x10^8
ϕ=177° (heated from below)
[Picture 25]

Figure 4.20 Effect of Rotational Speed of 53 rpm at ϕ = 180 degrees, Ta = 3.52x10^6

(a) Flow Field
ϕ = 90 deg.
Experimental

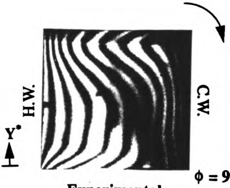

ϕ = 92 deg.
Experimental

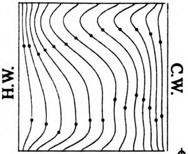

ϕ = 90 deg.
Numerical

(b) Temperature Field

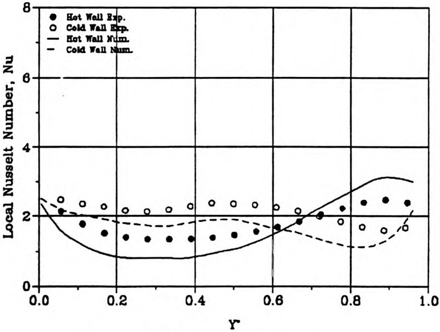

(c) Ω=53 rpm, Ra=1.83x10^6
ϕ=92° (vertical)
[Picture 22]

Figure 4.21 Effect of Rotational Speed of 53 rpm at ϕ = 92 degrees, Ta = 3.52x10^6

which is believed to be due the persistent influence of gravity. The excellent agreement between the experimental and the numerical temperature fields and local Nusselt number distributions is also clear in parts (b) and (c) of these figures. Figures 4.19 through 4.21 also show similar characteristics to figures 4.14 through 4.16 of 47 rpm, respectively, which indicate the stability of the enclosure flow at this region of the controlling parameters (namely Taylor and Rayleigh numbers). The increase in heat transfer near the ends of the isothermal walls in all these figures is attributed to the conduction in the insulated walls, but it can be seen that the values near the center of the hot wall approach pure conduction.

Figure 4.22 shows that at a Taylor number of 3.52×10^6 the field is greatly dominated by the wall shear, which as mentioned before, induces solid body rotation and limits the transfer of heat to the pure conduction mode. The numerical calculation also predicts the same uniform profile of the mean Nusselt number. The profile however is not completely flat which again indicates that the influence of gravity can still be detected at the current rotational speed. Comparing figure 4.22 to figure 4.17 it can be seen that the mean Nusselt number retains the same uniform distribution as a function of the angular position but the overall mean is decreasing slightly (<6%) with increasing rotation rate.

4.1.6 At Rotational Speed 62.0 rpm

The effect of increasing the speed of rotation to 62 rpm (Ta=4.82×10^6, Ra=1.7×10^5, andRa_r=3.7×10^4) is shown in figures 4.23 through 4.27. Figure 4.23a shows the responce of the flow field to the increase in the rotation rate Ω where it forms two equivalent cells that extend between the two isothermal walls. One of these cells (extends between the lower end of the walls) contains the stagnation region which was observed near the lower end of the cold wall at slower speeds of rotation, and the fluid circulates around it unable to penetrate into it.

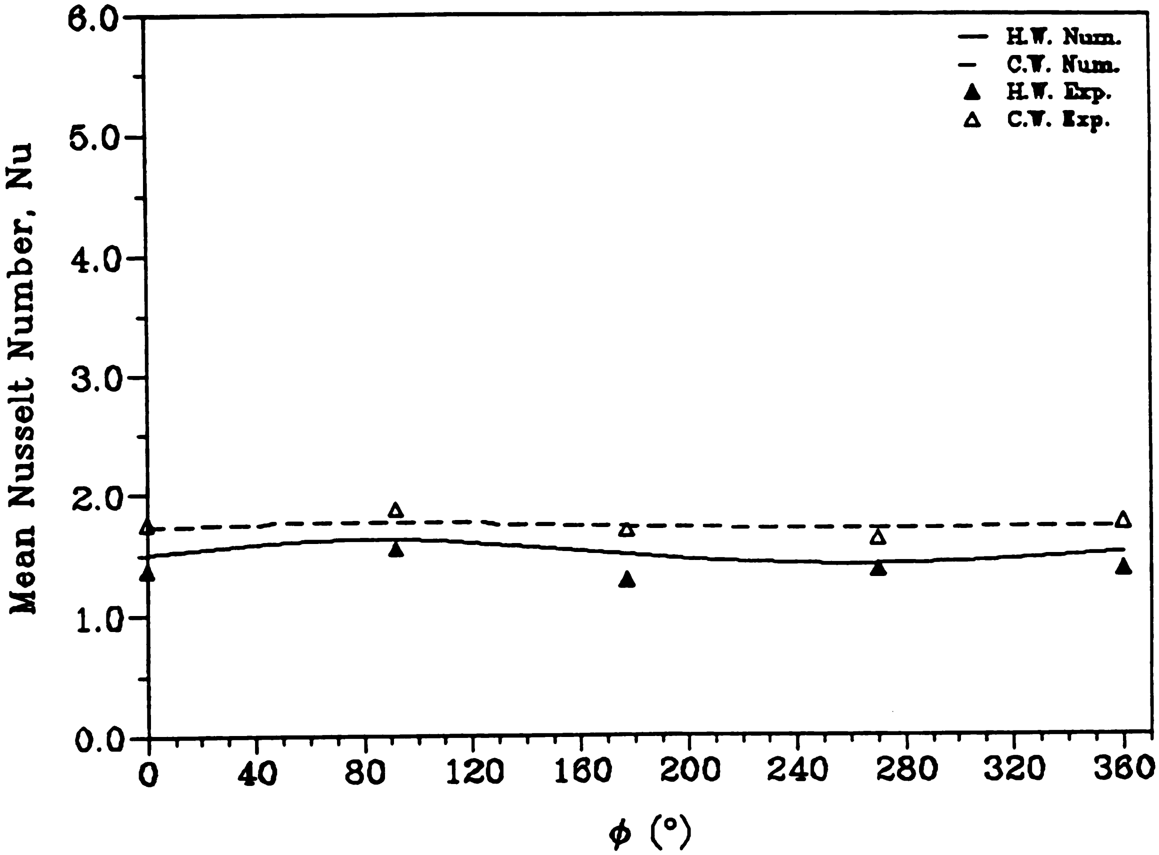

Figure 4.22 Mean Nusselt Number vs. Angular Position at 53 rpm (cw rotation), $Ra=1.83\times10^6$
$Ta = 3.52\times10^6$

H.W.

C.W.

(a) Flow Field
$\phi = 0$ deg.

$\vdash\!\!\blacktriangleright Y^*$ H.W.

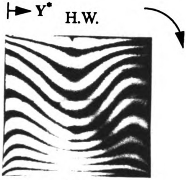

C.W.

(b) Temperature Field
$\phi = 358$ deg.

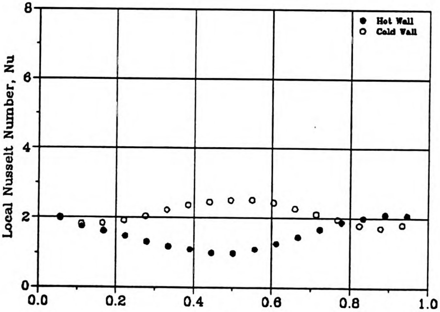

(c) Ω=62 rpm, Ra=1.70x10^5
ϕ=358° (heated from above)
[Picture 28]

Figure 4.23 Effect of Rotational Speed of 62 rpm at ϕ = 358 degrees, Ta = 4.82x10^6

Though the two cells are not identical they are almost equal in size, and they both emanate from the central region of the hot wall with outward opposite circulation at their outer boundaries. Again this interesting flow pattern is independent of the angular position as can be seen from part (a) of figures 4.24, 4.25 and 4.26, however some variation can still be seen in the isotherm patterns especially at $\phi=180°$ and 90° (figures 4.25b and 4.26b) which points out the persistance of the influence of gravity. The slow counter circulation of the two cells result in an area of stagnant fluid near the center of the hot wall which in turn suppresses the heat transfer in this region to pure conduction as can be seen from the local Nusselt numbers of parts (c) of the aforementioned figures. The bending of the isotherms shown in parts (b) also indicates circulation in the direction perpendicular to the isthermal walls which results in the increase of Nusselt number near the ends of the hot wall because the cold air moves down the insulated walls and impinges on both ends of the hot wall. The Nusselt numbers near the ends of the cold wall however are higher than what they should be because of the conduction in the insulated walls. Figure 4.27 illustrates the characteristics of the mean Nusselt number at the current rotational speed where the independence of the angular position and the low values indicate the beginning of the complete domination of the centrifugal buoyancy, which is also supported by the matching numerical calculations.

Note that the interesting two cell flow configuration encountered here arises from the domination of the imposed uniform centrifugal force which creates a highly stable two dimensional cellular flow pattern (may form multi-cellular patterns in a more shalow enclosure) that resembles the classical type of stable Benard convection (in a stationary heated from below enclosure) as predicted by Edwards(1967). Therefore, as the speed of rotation increases the two cells are expected to become more like a mirror image of each other and the circulation is expected to increase, thus increasing the heat transfer.

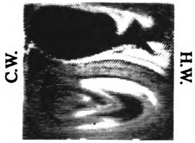

(a) Flow Field
ϕ = 270 deg.

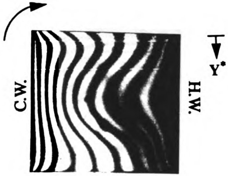

(b) Temperature Field
ϕ = 269 deg.

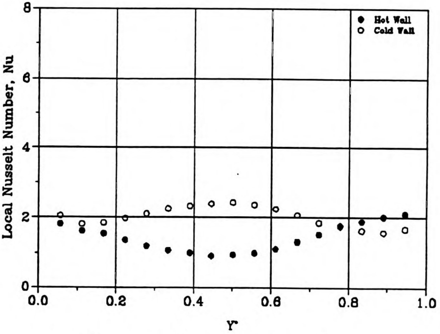

(c) Ω=62 rpm, Ra=1.70x10^5
ϕ=269° (vertical)
[Picture 29]

Figure 4.24 Effect of Rotational Speed of 62 rpm at ϕ = 269 degrees, Ta = 4.82x10^6

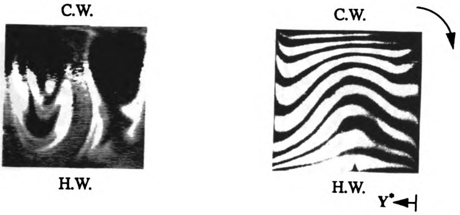

(a) Flow Field

(b) Temperature Field

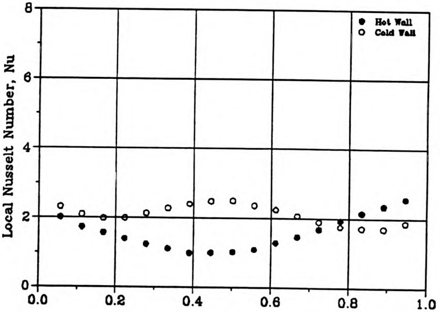

(c) Ω=62 rpm, Ra=1.70x10⁵
φ=180° (heated from below)
[Picture 31]

Figure 4.25 Effect of Rotational Speed of 62 rpm at ϕ = 180 degrees, Ta = 4.82×10^6

(a) Flow Field
$\phi = 90$ deg.

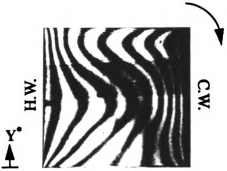

(b) Temperature Field
$\phi = 87$ deg.

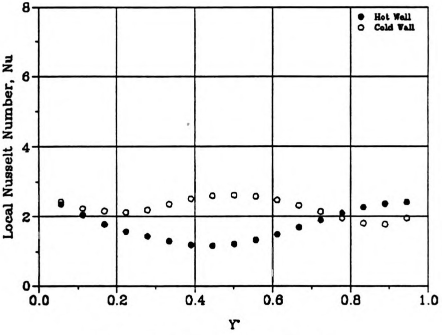

(c) $\Omega=62$ rpm, $Ra=1.70 \times 10^5$
$\phi=87°$ (vertical)
[Picture 30]

Figure 4.26 Effect of Rotational Speed of 62 rpm at $\phi = 87$ degrees, $Ta = 4.82 \times 10^6$

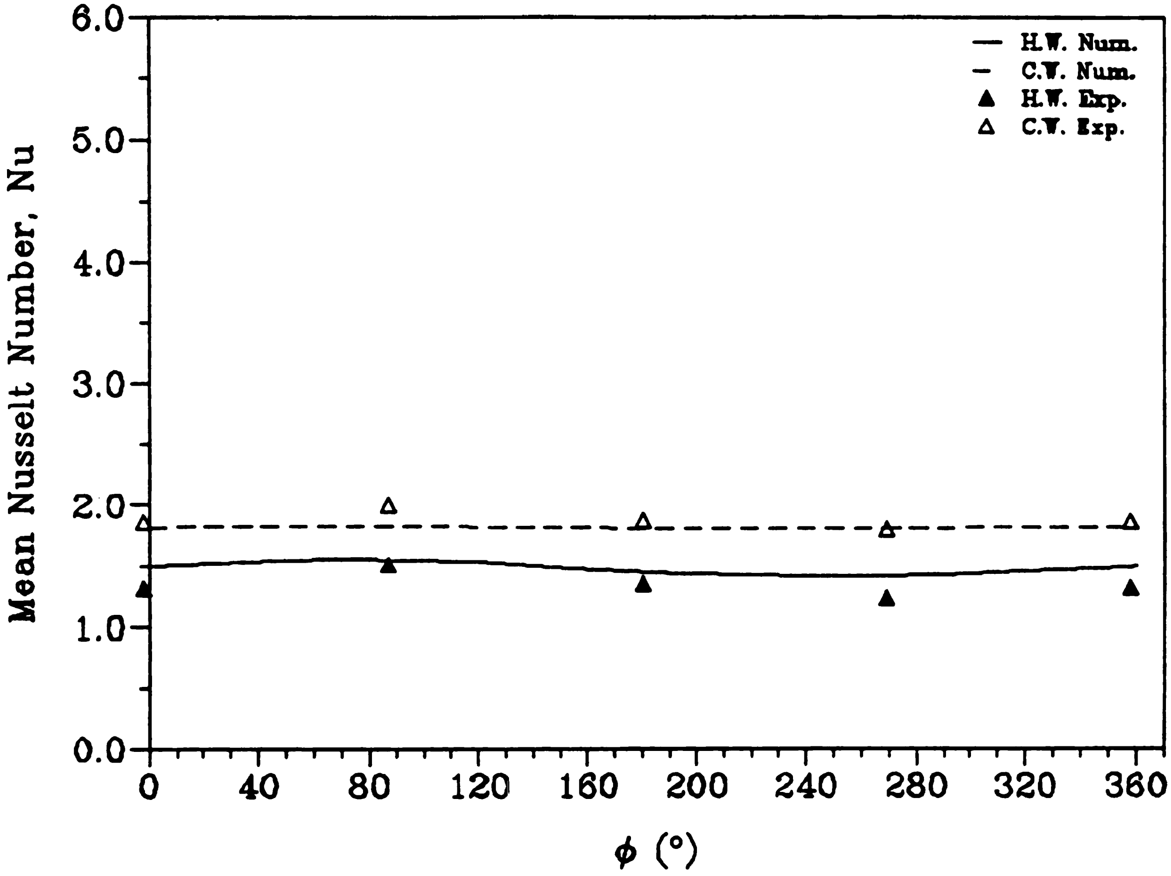

Figure 4.27 Mean Nusselt Number vs. Angular Position at 62 rpm (cw rotation), $Ra=1.70x10^6$
$Ta = 4.82x10^6$

Also as the speed of rotation increases the temperature field is expected to simulate the situation of a hot plume rising from a horizontal surface into cooler air.

4.1.7 At Rotational Speed 76.0 rpm

The two identical cell configuration predicted above is clearly illustrated in figures 4.28 through 4.31, where the effect of increasing the rotational speed to 76 rpm (Ta=7.24$\times10^6$, Ra=1.7$\times10^5$, and Ra_r=5.56$\times10^4$) is presented. The flow pictures in parts (a) of these figures belong to a slower rotational speed of 73 rpm, however they show the two equal cells to continue to circulate outward from the hot wall as a result of the centrifugal buoyancy. The difference in the brightness of these two cells is due to the injection of the smoke near the center of one of the insulated the insulated walls. The isotherms of parts (b) are also identical and symmetric at all angular positions thereby confirming the stability of the centrifugally driven buoyant flow. However the most interesting feature about this buoyant flow regime is its resemblance to the stable condition of heated from below. The only difference between the two is that the heated from below temperature field is affected in the vertical direction only by gravity, therefore it is expected to stretch or elongate vertically, while in the present situation it is influenced by the circumferencially uniform centrifugal force, therefore it is expected to stretch outward uniformly and become more like a mushroom stemming from the hot wall as the rotational speed is further increased.

The local Nusselt number distributions along the isothermal walls at the four designated angular positions are shown in part (c) of figures 4.28 through 4.31. Since all four profiles are identical it is no longer necessary to compare them to each other. However by comparing them to the corresponding profiles at rotational speed of 62 rpm (figures 4.23c through 4.26c) it can be seen that they are more symmetric about the median to the isothermal walls which further affirms that the two flow cells are

H.W.

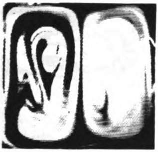

C.W.

(a) Flow Field
$\phi = 0$ deg.

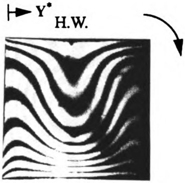

C.W.

(b) Temperature Field
$\phi = 358$ deg.

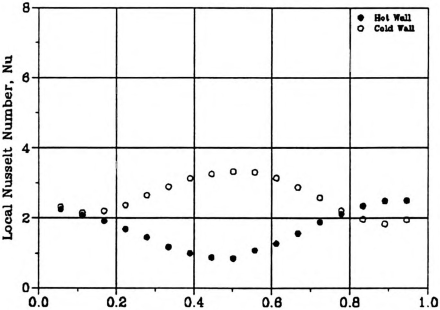

(c) Ω=76 rpm, Ra=1.70x10^5
ϕ=358° (heated from above)
[Picture 345]

Figure 4.28 Effect of Rotational Speed of 76 rpm at ϕ = 358 degrees, Ta = 7.24x10^6

(a) Flow Field
ϕ = 270 deg.

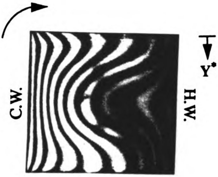

(b) Temperature Field
ϕ = 268 deg.

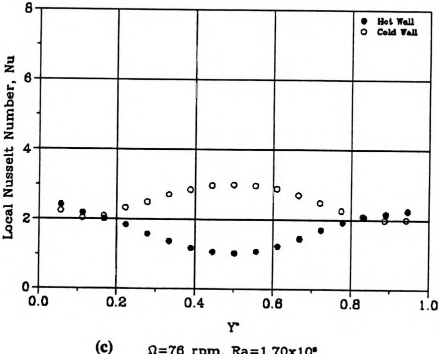

(c) Ω=76 rpm, Ra=1.70x10^{8}
ϕ=268° (vertical)
[Picture 340]

Figure 4.29 Effect of Rotational Speed of 76 rpm at ϕ = 268 degrees, Ta = 7.24x10^{6}

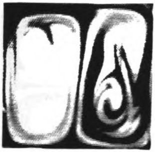

(a) Flow Field
ϕ = 180 deg.

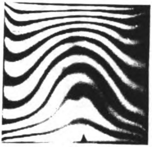

(b) Temperature Field
ϕ = 178 deg.

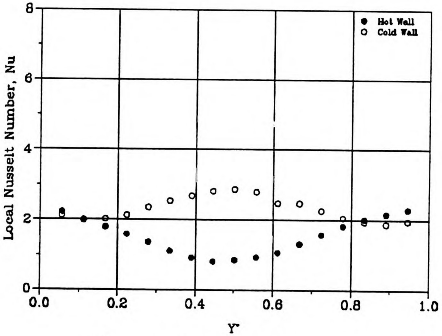

(c) Ω=76 rpm, Ra=1.70x10^6
ϕ=178° (heated from below)
[Picture 342]

Figure 4.30 Effect of Rotational Speed of 76 rpm at ϕ = 178 degrees, Ta = 7.24x10^6

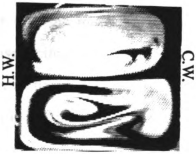

(a) Flow Field

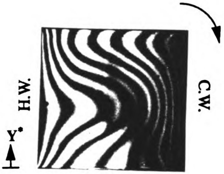

(b) Temperature Field

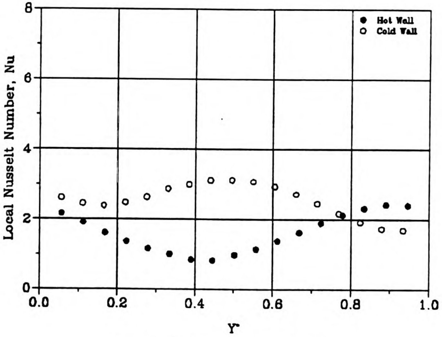

(c) Ω=76 rpm, Ra=1.70x10^5
ϕ=90° (vertical)
[Picture 343]

Figure 4.31 Effect of Rotational Speed of 76 rpm at ϕ = 90 degrees, Ta = 7.24x10^6

identical in size and flow velocities. It can also be seen that the hot wall profiles are becoming more concave in the middle region and higher near the ends (almost 100% higher than the middle) with the opposite profile on the cold wall, which points to increased circulation in the flow cells. Finally, the mean Nusselt number values shown in figure 4.32 are as uniform as expected, with an overall mean value of 1.4 which is less than 4% higher than that of the previous rotational speed (62 rpm).

4.1.8 At Rotational Speed 90.0 rpm

Figures 4.33 through 4.36 show the effect of a rotational speed Ω=90*rpm* (Ta=1.02×10^7, Ra=1.82×10^5, and Ra_r=8.35×10^4) on the flow and temperature fields and the Nusselt number distributions, the flow visualization pictures however are for a lower rotational speed of 83 rpm. Again the figures show a continuation of the trend of no dependance on the angular position, and the flow continues to be steady and highly stable as can be seen from part (a) of the above figures and from the continuous motion recorded on video tape. The shape of the isotherms of part (b) indicates smaller temperature gradients near mid-hot wall and higher gradients on the sides which means increased circulation. Also note that the pocket of hot air emanating from the hot wall extends further towards the cold wall as predicted. The numerical calculation of the flow and temperature fields shown in parts (a) and (b) again agrees with the experiment, however it should be noted that gravity was neglected in the numerical model in order to match the flow field.

By comparing the local Nusselt number profiles of figures 4.33c to 4.35c with those of figures 4.28c to 4.31c it can be seen that the lowest nusselt number values near the middle of the hot wall are almost the same as those of the lower rotational speed of 76 rpm (approximately equal 1 which correspongs to pure conduction) while the maxima near the sides are higher, which amounts to a 13% to 20% increase in the mean Nusselt number values shown in figure 4.36 over the corresponding

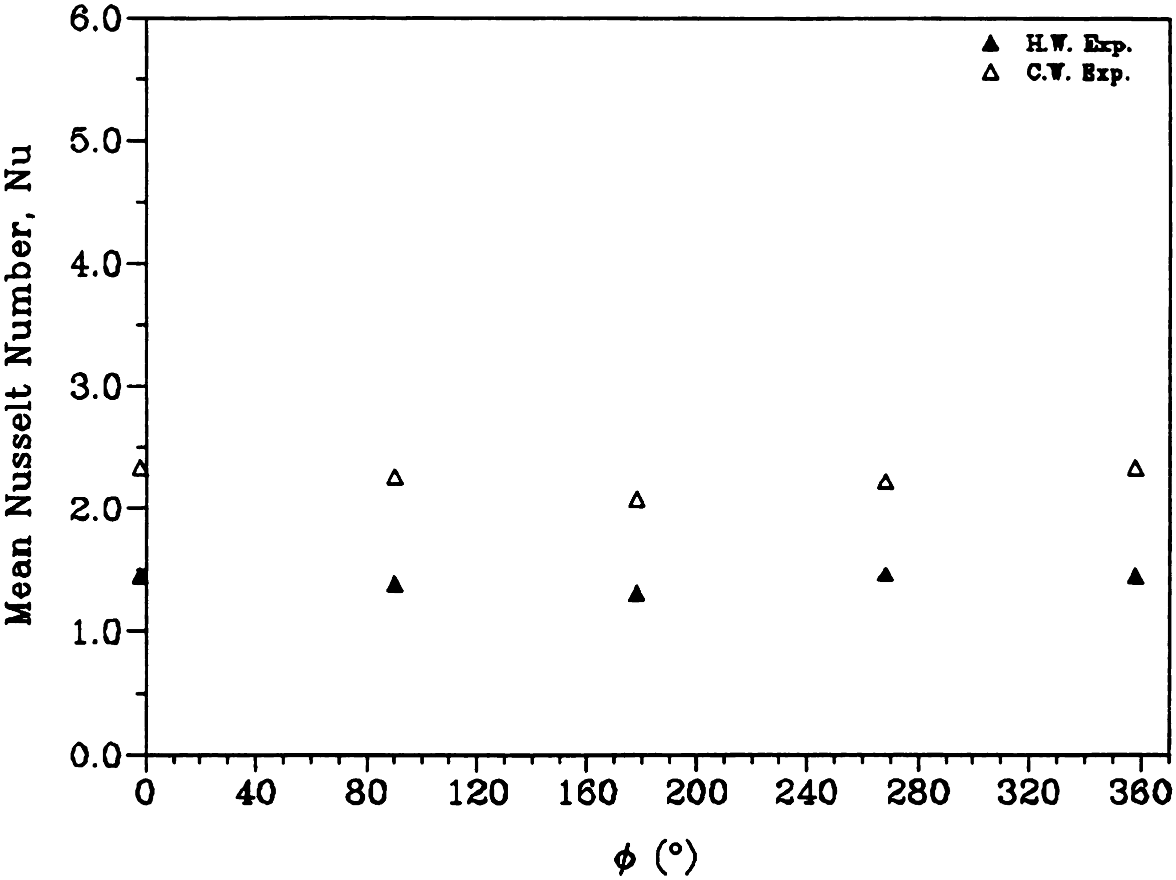

Figure 4.32 Mean Nusselt Number vs. Angular Position at 76 rpm (cw rotation), $Ra=1.70x10^6$
$Ta = 7.24x10^6$

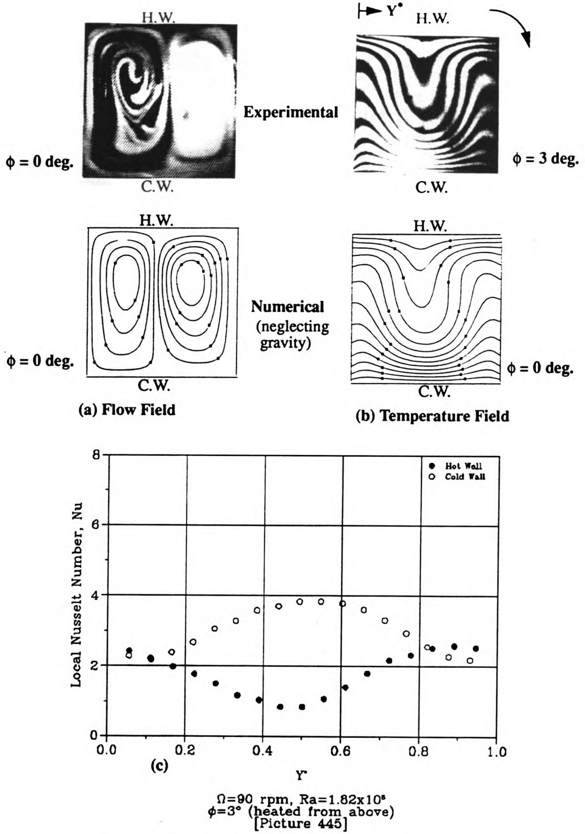

Figure 4.33 Effect of Rotational Speed of 90 rpm at $\phi = 3$ degrees, Ta = 1.02×10^7

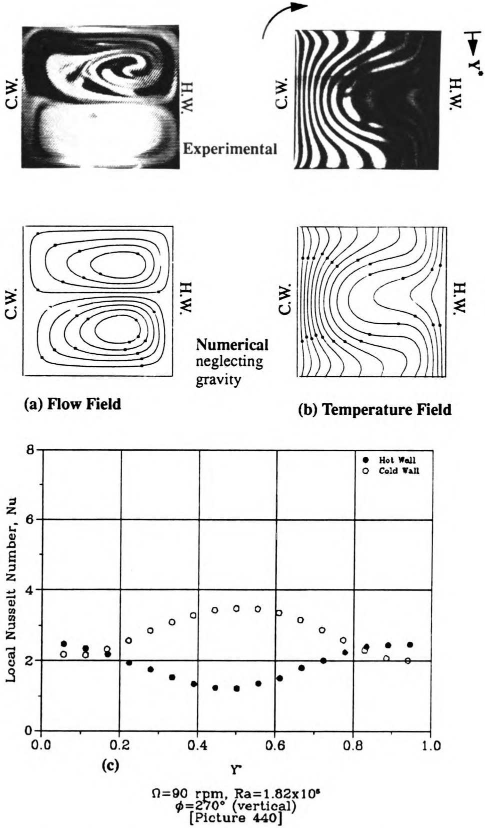

Figure 4.34 Effect of Rotational Speed of 90 rpm at ϕ = 270 degrees, Ta = 1.02×10^7

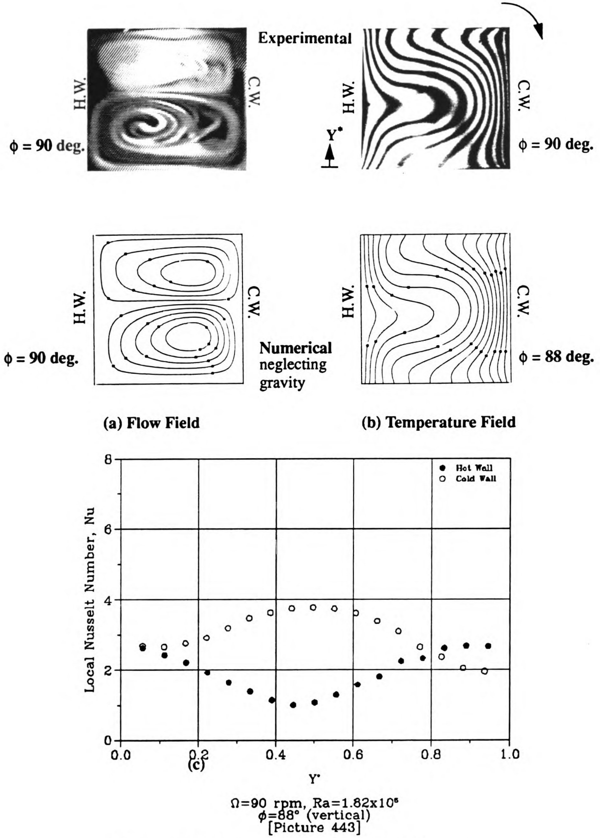

Figure 4.35 Effect of Rotational Speed of 90 rpm at ϕ = 88 degrees, Ta = 1.02×10^7

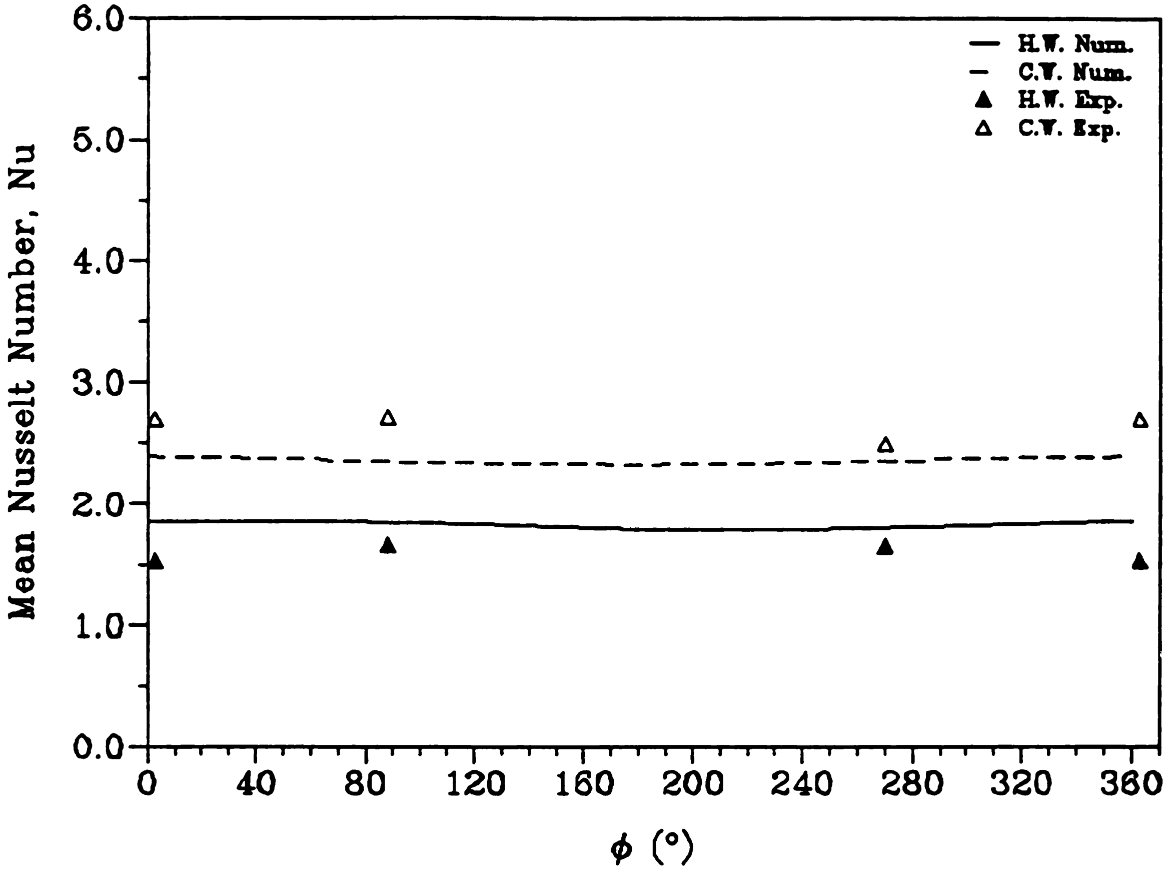

Figure 4.36 Mean Nusselt Number vs. Angular Position at 90 rpm (cw rotation), $Ra=1.82\times10^6$ **$Ta = 1.02\times10^7$**

values shown in figure 4.32 for $\Omega=76rpm$. Figure 4.36 also shows flat experimental and numerical mean Nusselt number profiles which shows the centrifugal buoyancy to continue to be the dominant force, and the influence of gravity to disappear completely. The overall mean Nusselt number is also increased by about 15% which is proportional to the increase in the angular speed.

4.1.9 At Rotational Speed 118.0 rpm

Because of the size and weight of the test section the highest speed of rotation reached in the present study was 118.0 rpm which corresponds to a Taylor number $Ta=1.78\times10^7$. At this speed the Rayleigh number is $Ra=1.78\times10^5$ and the rotational Rayleigh number is $Ra_r=1.4\times10^5$. The isotherm patterns of figures 4.37a through 4.39a show that the steady symmetric, two cell flow regime continues to prevail. They also show the bulging of the hot air pocket near the cold wall. The numerical calculation also shows a similar behavior, however they are not completely symmetric like the experiment, and that is because gravity is considered in the model in this case. This shows that the numerical model over estimates the influence of gravity at such a high Taylor number. The local Nusselt number profiles of part (b) of the same figures show noticable increase in the mid-wall Nusselt number values which suggest increased motion in this previously stagnant region. The numerical values do not show that improvement in the mid hot wall local Nusselt numbers, and the hot wall profiles are skewed toward one side of the enclosure, but interestingly this skewed orientation is the same in all angular positions which suggests that it may not be the result of over estimation of the influence of gravity.

Figure 4.40 shows significant increase in the mean Nusselt numbers with an overall mean value of 1.95, almost 20% higher than that of the lower rotational speed of 90.0 rpm, and more than 43% higher that the lowest overall mean attained at $\Omega=62rpm$.

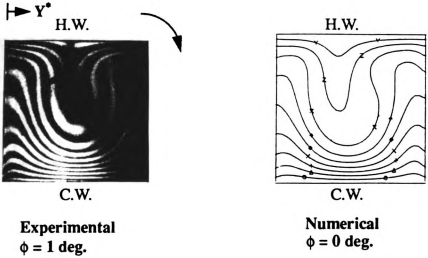

(a) Temperature Field

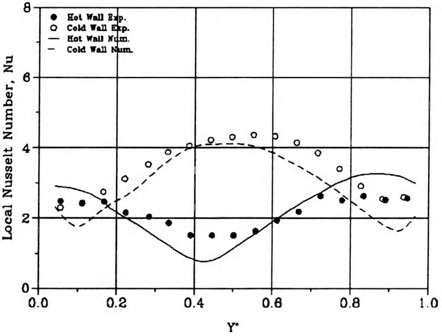

(b) Ω=118 rpm, Ra=1.78x10[6]
ϕ=1° (heated from above)
[Picture 41]

Figure 4.37 Effect of Rotational Speed of 118 rpm at ϕ = 1 degree, Ta = 1.75x10^7

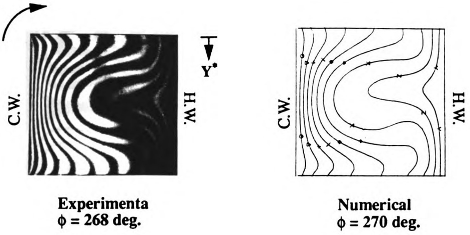

(a) Temperature Field

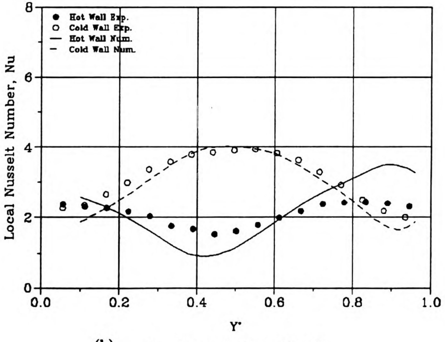

(b) Ω=118 rpm, Ra=1.78x10^6
ϕ=268° (vertical)
[Picture 43]

Figure 4.38 Effect of Rotational Speed of 118 rpm at ϕ = 268 degrees, Ta = 1.75x10^7

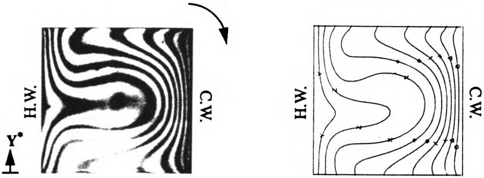

Experimental **Numerical**

(a) Temperature Field

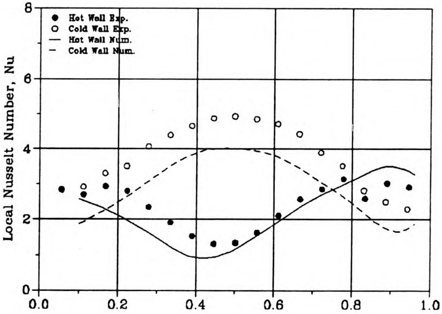

(b) Ω=118 rpm, Ra=1.78x10^5
ϕ=90° (vertical)
[Picture 40]

Figure 4.39 Effect of Rotational Speed of 118 rpm at ϕ = 90 degrees, Ta = 1.75x10^7

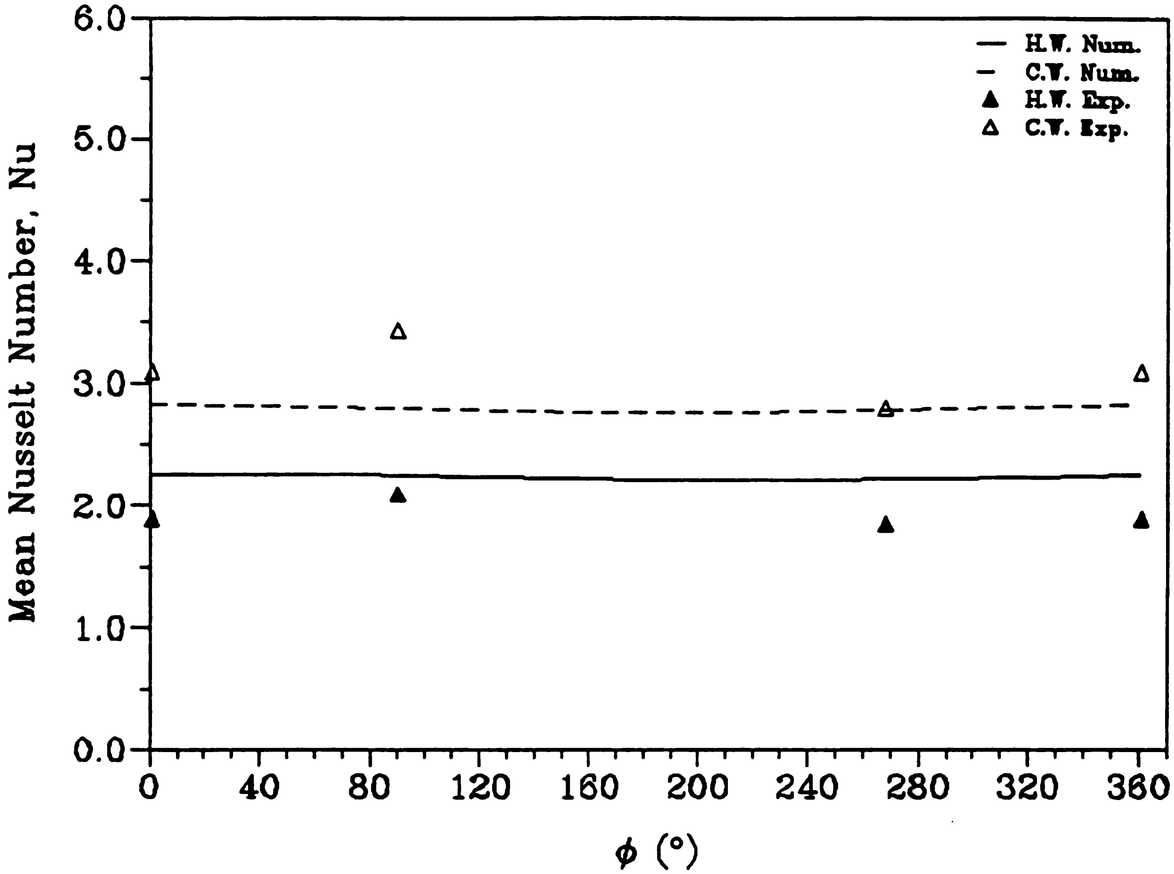

Figure 4.40 Mean Nusselt Number vs. Angular Position at 118 rpm (cw rotation), $Ra=1.78x10^6$ $Ta = 1.75x10^7$

4.2 Effect of Rotation on the Mean Nusselt Number

The mean Nusselt number is the result of the numerical integration of the local Nusselt numbers over the height of the isothermal wall at an angular position. And as shown above these values were used to illustrate the variation in the enclosure heat transfer over one cycle at every rotational speed examined. In this subsection the mean values are discussed as a function of the rotation rate in order to demonstrate the influence of rotation on the enclosure convection heat transfer at each previously selected angular position. At a particular position the mean Nusselt number of the hot wall is expected to be equal to that of the cold wall. However as mentioned previously in this chapter, lateral conduction in the insulated (plexiglas) walls results in significant increase in the cold wall values, especially when the convection currents are slow. Therefore, only the mean Nusselt numbers at the hot wall are discussed, while the values at the cold wall are shown for their qualitative value. Note that the mean Nusselt numbers are plotted vs. the product of Rayleigh and Taylor numbers (instead of the rotational speed) in order to bring to mind the influence of the combined gravitational and rotational buoyancies on the enclosure heat transfer. However the rotational Rayleigh number could have also been used in conjunction with the other two parameters without loss of the physical phenomena.

Figures 4.41 to 4.44 show the inluence of the rotational speed Ω ranging from 22.5 rpm (Ta=6.34$\times10^5$) to 118 rpm (Ta=1.75$\times10^7$) at a Rayleigh number, Ra=(1.77$\pm$0.07)$\times10^5$. At the vertical position ϕ=270 figure 4.41 shows a sharp decline of more than 53% in the mean Nusselt number between Ω=22.5-47.0 rpm (Ta=6.34$\times10^5$–2.77$\times10^6$). This region was characterized initially by enhanced mixing due to the combined influence of the gravitational buoyancy and the Coriolis force, then by the transition to near solid body rotation due to the viscous shear forces. Then heat transfer starts to show a moderate increase due to the growing influence of the centrifugal buoyancy which resulted in the steady two cell flow configuration.

Mean Nusselt Number, Nu

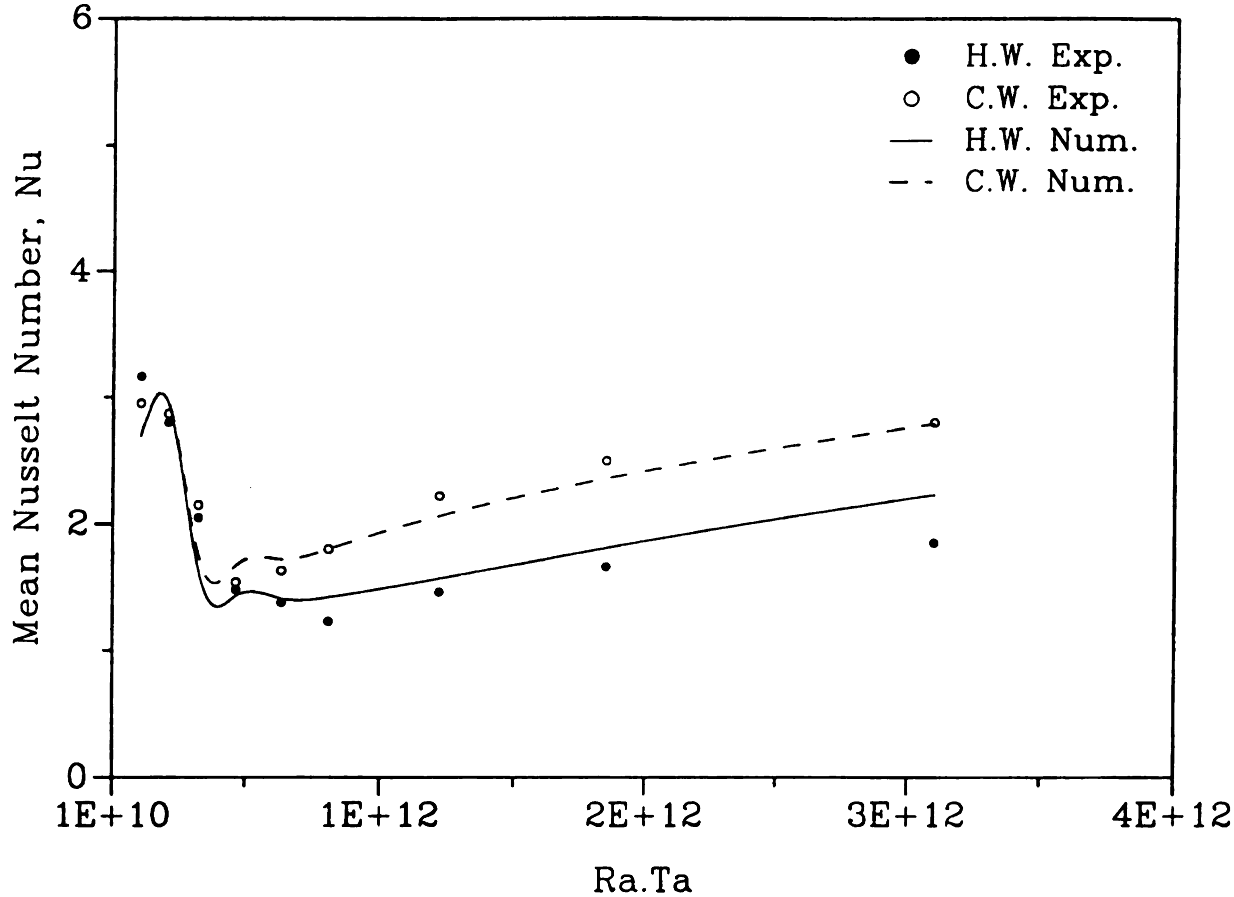

Figure 4.41 Mean Nusselt Number vs. RaxTa at Angular Position ϕ=270 (vertical)

The numerical resuls are also in agreement with the experimental results, and they show that the heat transfer should peak somewhere between 22.5 and 32 rpm.

In figure 4.42 it can be seen that at the heated from below position (ϕ=180°) the maximum value of the mean Nusselt number (near the lower end of the scale) increases by almot 47% over that of the previous vertical position, and that is mainly due to increased influence of the gravitational buoyancy. Despite the significant increase in the maximum value the mean Nusselt number decreases sharply to almost the same value of the previous position (ϕ=270°) at 47 rpm and then follows the same trend. The numerical results also show the large increase at low rotation rates and the identical behavior at higher rates.

At the opposite vertical position (ϕ=90°) figure 4.43 shows a profile similar to that of ϕ=180°, and while the experiment shows about 15% inrease in the peak value the numerical predictions are almost the same. The results are also in agreement with those of Hamady et al. (1990), where the mean Nusselt number is shown to increase consistantly from slower rotation rates (6.5 rpm to 17 rpm) until it connects with the results of the present study. Figure 4.44 shows the mean Nusselt number profile at the heated from above position (ϕ=0°) where the maximum value at slow rotation rates is low as expected because of the absence of the gravitational buoyancy at this angular position.

Figures 4.41 to 4.44 clearly show that three regions can be identified where the heat transfer exhibits unique characters: a low rotation region where the heat transfer is enhanced in a periodic fashion due to the combined influence of gravity and Coriolis acceleration, a moderate rotation region where the heat transfer is greatly suppressed to a minimum of approximately 1.4 because of the viscous shear forces, and a high rotation region where the heat transfer is steady and moderately increasing with the increasing speed of rotation.

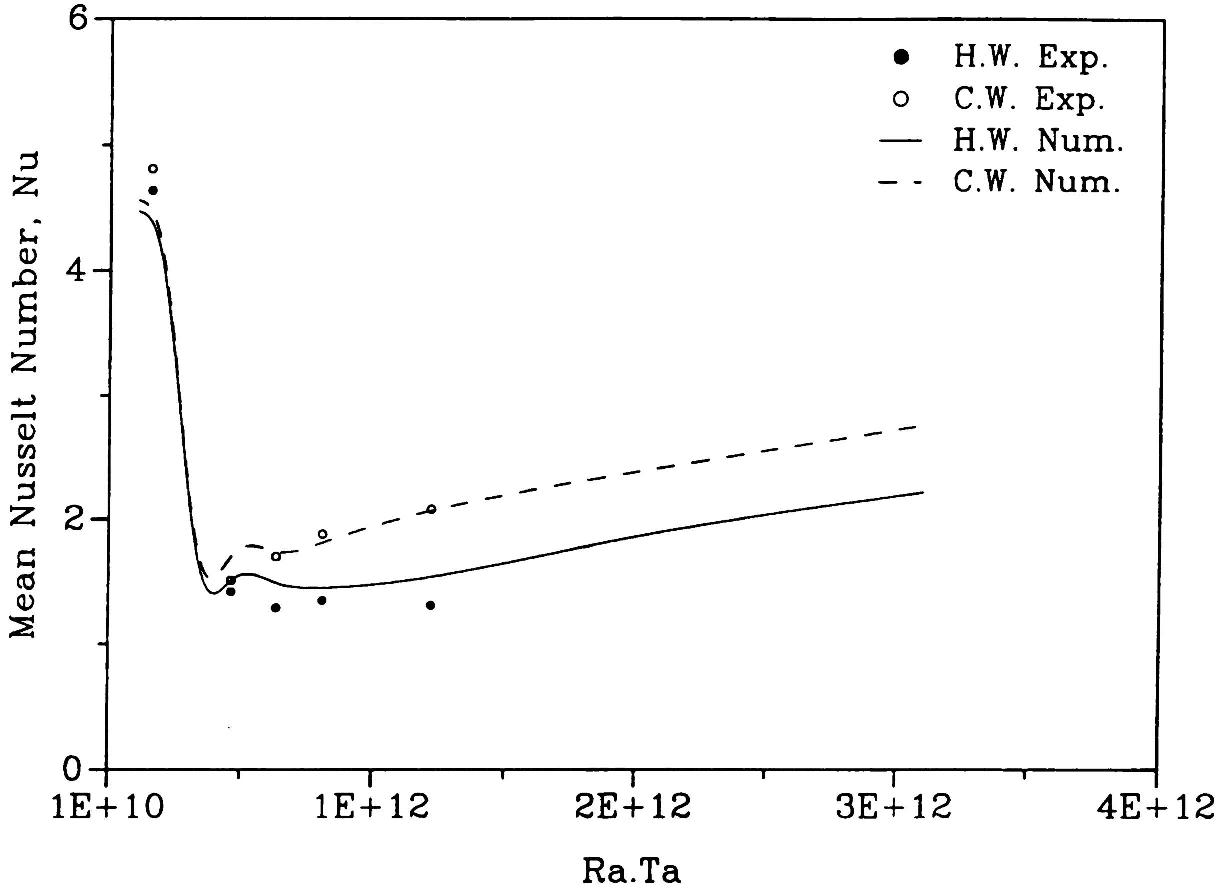

Figure 4.42 Mean Nusselt Number vs. RaxTa at Angular Position ϕ=180 (htd frm below)

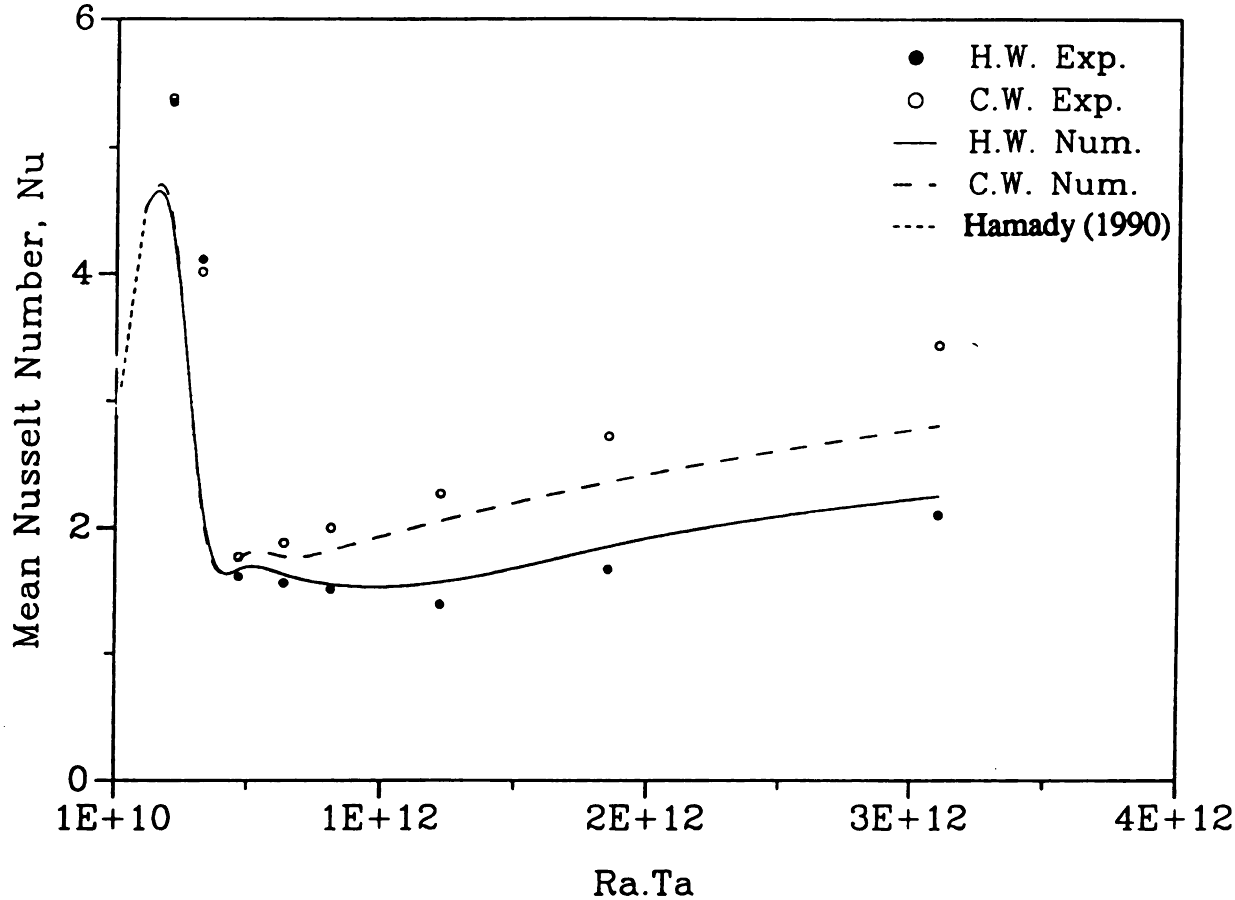

Figure 4.43 Mean Nusselt Number vs. RaxTa at Angular Position ϕ=90 (vertical)

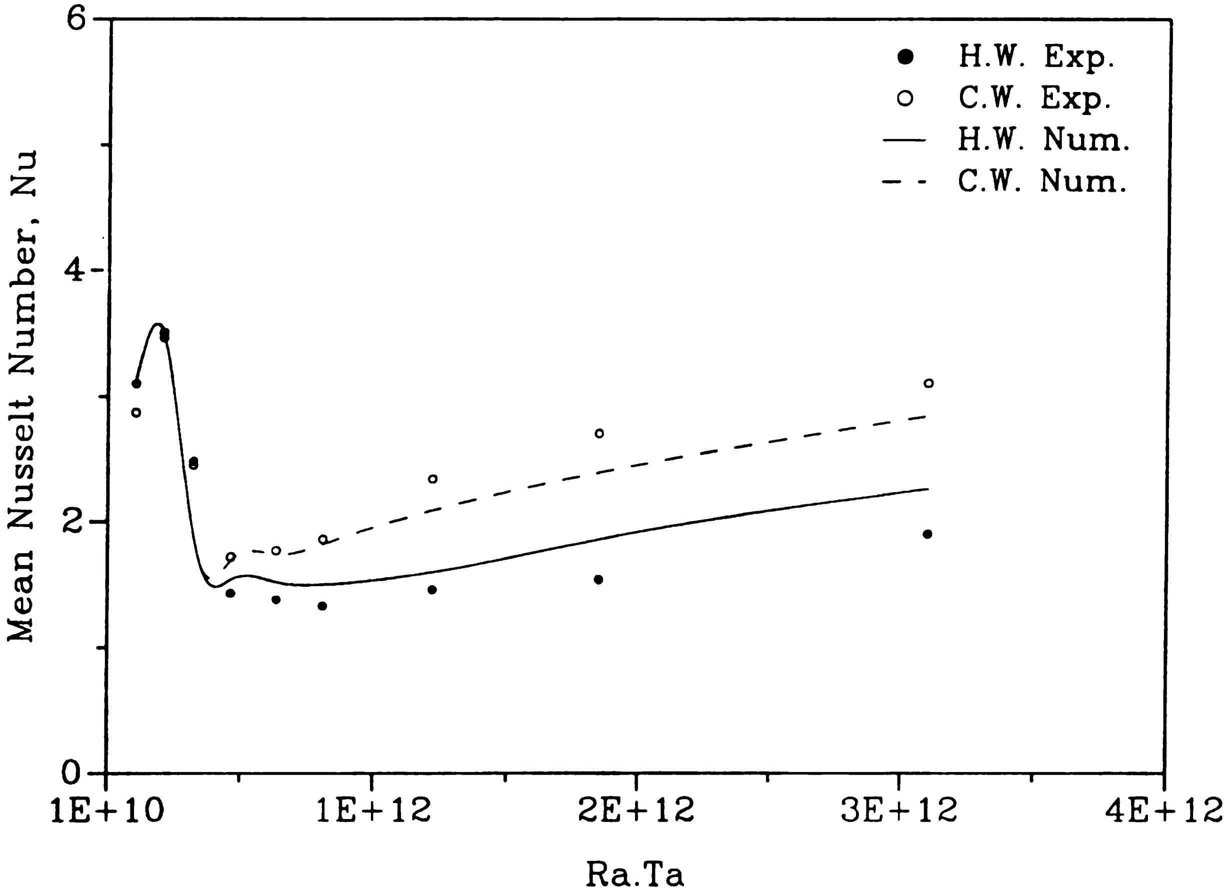

Figure 4.44 Mean Nusselt Number vs. RaxTa at Angular Position ϕ=0 (heated from above)

4.3 Effect of Rotation on the Overall Mean Nusselt Number

In figure 4.45 the overall mean Nusselt number is plotted vs. the product of Rayleigh and Taylor numbers. The overall mean is the average of the mean Nusselt numbers at the four selected angular positions, which means that it represents the average heat transfer to be expected over a cycle at a given rotation rate. In this figure the three regions suggested above are roughly marked. In region 1 ($6.34\times10^5 \leq Ta \leq 1.28\times10^6$) the mean Nusselt number is noted to climb slightly from 3.63 to 3.87, an inrease of almost 7% which is supported by a comparable increase in the numerical values. And though two data points in this region are not sufficient for obtaining a numerical correlation, the increase seems proportional to $Ra^{1/4}\times Ta^{1/8}$ which further supports the idea of dominating gravitational buoyancy and Coriolis forces in this region.

Region 2 was characterized by the domination of the wall shear effects, where the visual study of the flow indicated a transition from the unicellular slushing motion to the bicellular steady flow pattern. In this region the overall Nusselt number droped from a maximum of almost 3.9 to a minimum of less than 1.4 over the Taylor number range of $1.28\times10^6 \leq Ta \leq 2.77\times10^6$. In region 3 the steady 2 cell flow pattern was an evidence of the domination of the centrifugal buoyancy which is shown to enhance the Nusselt number by almost 39% over a Taylor number range of $2.77\times10^6 \leq Ta \leq 1.75\times10^7$. The data in region 3 can be correlated by:

$$Nu = 0.067\, Ra_r^{0.2825} \tag{4.1}$$

this correlation was obtained using the method of least squares, and it predicts the experimental data in this region within ±5% as shown in figure 4.46.

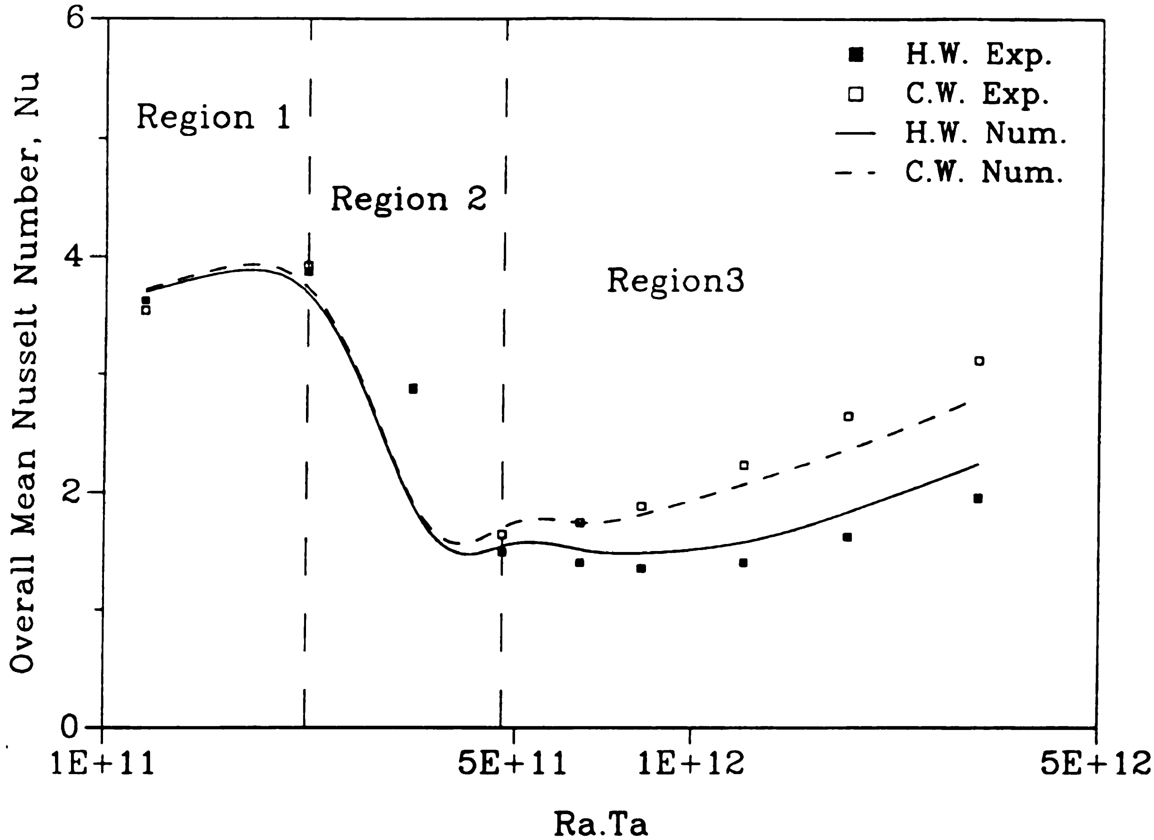

Figure 4.45 Overall Mean Nusselt Number vs. RaxTa

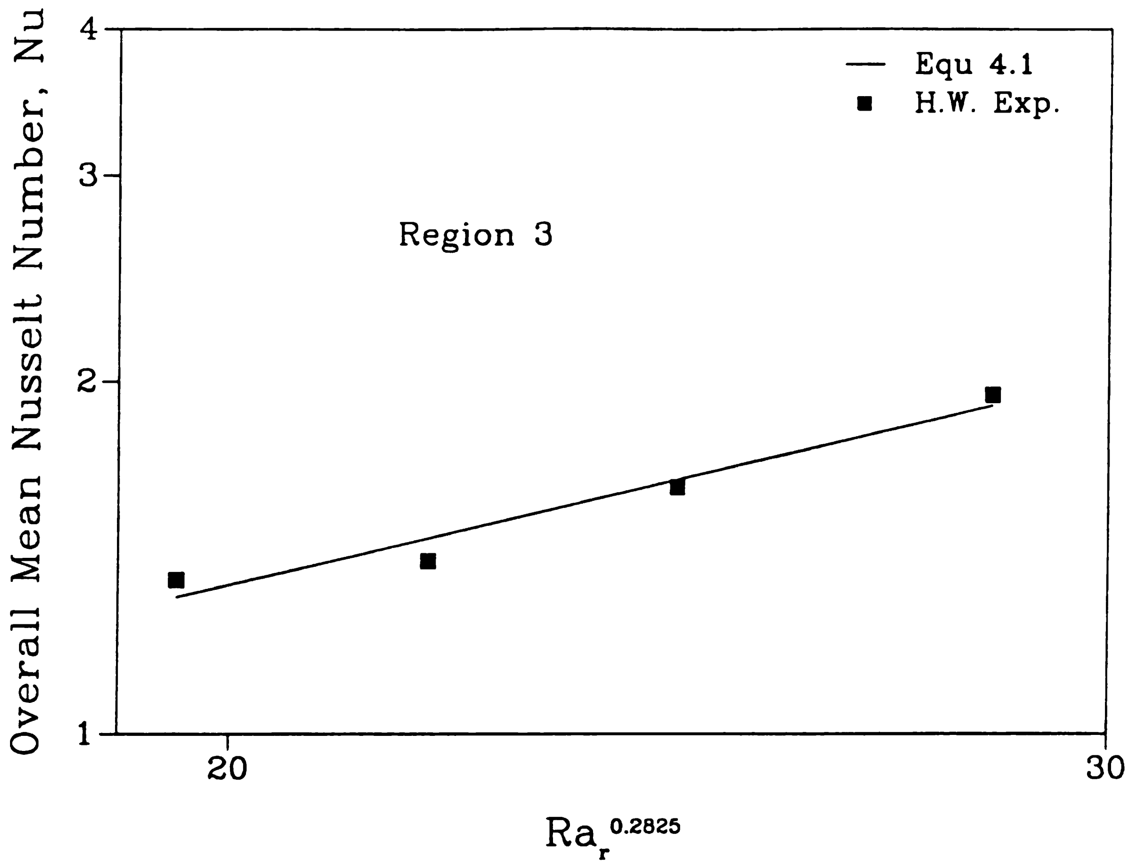

Figure 4.46 Correlation of The Overall Mean Nusselt Number at High Rotation Rates

In general the experimental results presented in this chapter and the good agreement with the numerical predictions provide a comprehensive description of the qualitative nature of the flow dynamics and accurate estimates of the heat transfer in the range of parameters considered. Unique flow patterns and a well defined transition from gravity dominant to centrifugal force dominant regions explained the augmentation of heat transfer in some regions of the controlling parameters and its suppression in other regions. The results showed the transition from boundary layer flow to potential flow as a result of friction forces which greatly suppressed the heat transfer to near pure conduction. It showed the transition from highly unsteady to interesting steady and uniform temperature and flow patterns at high speed rotation. The flow is shown to be periodic at low rotation rates (region 1) and highly stable at high speed rotation (region 3), while the effect of rotation throughout the study was to make the flow two dimensional.

CHAPTER 5

SUMMARY AND CONCLUDING REMARKS

In the present study natural convection heat transfer in a rotating enclosure was experimentally investigated. A horizontally oriented, differentially heated, air filled parallelepiped enclosure of cross-sectional aspect ratio of one (square) and longitudinal aspect ratio of ten was confined to rotate about its longitudinal axis at uniform angular speeds. Real time visual flow observations were done using smoke and laser sheet at the mid-section of the enclosure. Flow visualizations were used to qualitatively understand the interaction of gravitational and rotational buoyant flows and their effect on the heat transfer. A Mach-Zehnder interferometer was used to study the 2-D spatial and temporal temperature distributions inside the cavity. The interferometer was adjusted in the *infinite fringe mode* to directly reveal the entire temperature field, which allowed subsequent calculation of the local Nusselt number distribution at the enclosure's isothermal walls.

The study revealed interesting flow and temperature patterns in the Taylor number range of 10^5 to 10^7 and rotational Rayleigh number range of 10^3 to 10^5 for a Rayleigh number of approximately 2×10^5. It also established three regions where the characteristics of heat transfer are greatly influenced by the domination of one or more of the controlling parameters.

At slow rotation rates up to 32 rpm, rotation was seen to enhance the heat transfer and force gravitationally driven buoyant flows near the isothermal walls into boundary layer flow regimes. The boundary layer flow induced the formation of vortical structures at opposite corners on the isothermal walls as the hot wall moved from top to bottom (ϕ=0° and 270°). These vorticies were swept inward to the core region due to the Coriolis force during the second half of the cycle. Gravitational buoyancy, and Coriolis force induced cross flows, resulted in counter rotation of the core region during the first half of the cycle, and co-rotation during the second half in an oscilating, sloshing like type of motion which enhanced the mixing of the core region fluid, and therefore increased the heat transfer.

The convection process at this first domain of low rotation rates is highly periodic because of the interaction between the influential gravity field and the uniform less effective rotational force fields. This periodicity was seen in the flow and isotherm patterns, as well as in the asymmetric profiles of the local Nusselt number at the isothermal walls and the sinusoidal distribution of their mean values over one cycle.

At rotation rates from 32 to 47 rpm the thickness of the boundary layer increased due to increasing viscous friction, until the entire enclosure fluid attained a state of near solid body rotation. This second region represented a transition from gravitationally dominated to centrifugally dominated flow fields, and was characterized by a sharp decline in heat transfer, which dropped from a maximum of 3.9 at 32 rpm to a minimum value slightly higher than that of pure conduction in air at 47 rpm. The periodic nature of the flow was also seen to fade in this transition region.

In the third region of 53 to 118 rpm the centifugal force became more dominant, which resulted in an interesting flow regime of two equal, counter rotating cells which resembled the classic case of a fluid layer above a horizontal plate heated from below under stable conditions, with the difference that the centrifugal force acts in the radial direction while gravity acts only in the vertical direction. In this region the heat transfer increased steadily with the rotational speed. The overall Nusselt number data in this region was correlated with the rotational Rayleigh number which represents a measure of the centrifugal buoyancy. At 76 rpm the periodic motion completely disappeared, and the isotherms and the local Nusselt number distributions became symmetric.

In conclusion, the experimental results of the present study provide a major contribution to the present knowledge on enclosure heat transfer by establishing the existance of a transition region from gravity dominated to centrifugally dominated natural convection regimes in axially rotating enclosures in general. This transition region was shown to be associated with substantial suppression in heat transfer to near pure conduction in the working fluid.

In addition, several other aspects about this study are noteworthy from both academic and application points of view:

The study contributes to the basic understanding of heat transfer in rotating enclosures under the effect of gravity, an area for which experimental data is almost non-existent. Consequently, the experimental results were used to validate the numerical algorithm of Yang, Yang and Lloyd (1988), which showed excellent agreement with the experiment in most cases.

Also the experimental results provided test cases for the enhancement or suppression of local or mean heat transfer due to the combined effect of rotation and gravity. Such cases are extremely useful in the design of certain rotating devices where temperature control is vital. And by applying the mass transfer analogy the results can be of equal importance in chemical deposition processes where control over the uniformity of the rate of mass transfer is essential.

Increasing the rotation rate to the point where gravity effects become negligible makes available a tool for simulating the heat transfer process in a near zero gravity field, a new area of great importance to space lab research and technical applications.

It is also worth noting that the fiber-optics based flow visualization system developed for the present study was shown to be a powerfull tool in studying rotating enclosures in general, and that the interferometry technique used for collecting the thermal data proved to be suitable for studying rotating systems despite the sensitivity to the rotation-induced vibrations.

At this point some suggestions are made for future experimental and numerical work on heat transfer and buoyant fluid flow in rotating enclosures, with either interacting or negligible gravity field.

Fore a more complete understanding of the physics of the problem it is important to establish the effect of, the imposed temperature difference and the properties of the working fluid for a broad range of Rayleigh and Prandtl numbers, on the transition from gravitationally driven to centrifugally driven buoyant flows.

Also as a natural extension to the present study it is suggested to increase the rotational speed and study the delay of transition to turbulent flow regiems.

It is also interesting to study the effect of some orientation and geometric factors like the aspect ratio (a more shallow enclosure), and the angle of inclination between the axis of rotation and the gravity vector.

Finally, it is of equal importance to study the effect of introducing a distance of eccentricity between the geometrical axis of the enclosure and the axis of rotation which simulates off-axis parallel rotating cavities in a wide range of applications.

Appendices

APPENDIX A

INTERFEROGRAM ANALYSIS

When the Mach-Zehnder interferometer introduced in chapter 3 is adjusted in the infinite fringe setting, each resulting fringe is the locus of points in a 2-dimensional field where the refractive index of air is constant. According to the Gladstone-Dale equation,

$$\frac{n-1}{\rho} = C \tag{A.1}$$

where C is the Gladstone-Dale constant, the refractive index is linearly related to the density of air. This implies that each fringe represents the locus of points in a 2-dimensional field where the density is constant. Therefore, by utilizing the ideal gas equation of state,

$$P = \rho R T \tag{A.2}$$

at constant static pressure, each fringe can be calibrated as the locus of points where the temperature is constant (isotherm). Using this result, the Temperature gradient at the immediate vicinity of the isothermal walls of the enclosure can be measured at discrete locations and used for calculating the local Nusselt numbers as discussed in Appendix B.

The temperature differenc between two isotherms is calculated by,

$$\Delta T_i = \frac{(T_H - T_C)}{m-1} \tag{A.3}$$

where, m is the number of the fringes in the field. The distance between the wall and the center of each fringe is then measured using a high resolution traveling microscope, and the temperature vs. location data is then plotted as shown in the example of figure A.1, where x=0.0 is at the hot wall and x=1.0 is at the cold wall. A polynomial function would then be fitted to the measured points, and the temperature gradient at the hot and cold walls would be obtained by differentiation of the function at x=0.0 and x=1.0, respectively.

Two sources of error in the process of determining the temperature gradient contribute to the relatively low accuracy of this method of analysis based on the infinite fringe mode of interferometry, first the uncertainty in the location of the center of a fringe, and second and more importantly the difficulty associated with choosing the most accurate function that predicts the measured data. Estimates of the error associated with each one of these sources are discussed in Appendix C.

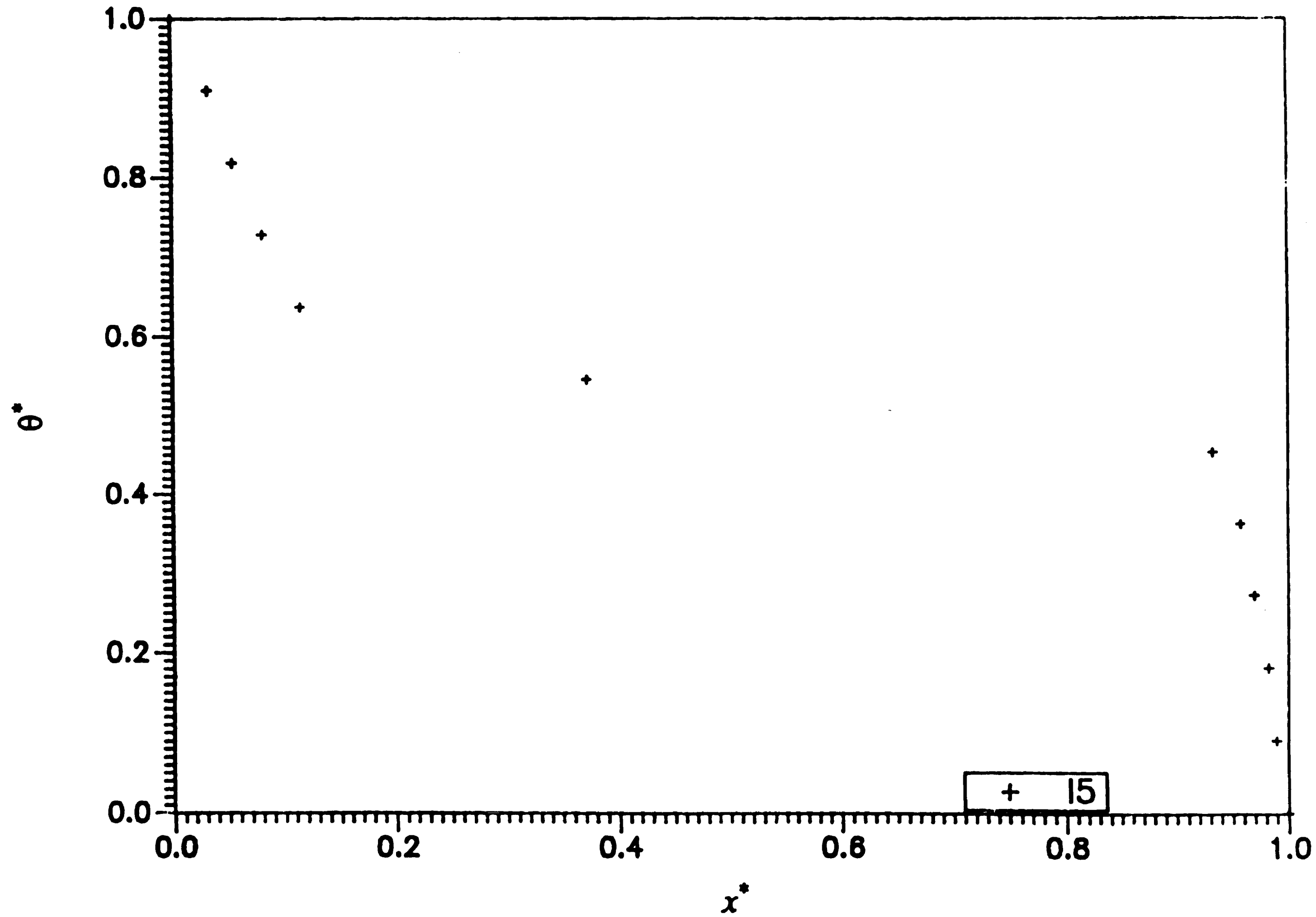

Figure A.1 Diagram of Temperature vs. Location

APPENDIX B

NUSSELT NUMBER ANALYSIS

Heat transfer in the thin layer of air adjacent to the enclosure's isothermal walls is dominantly by condution, where the heat flux transfered per unit surface area is,

$$q = -\, k_s \left[\frac{\partial T}{\partial x}\right]_{x=0} \tag{B.1}$$

where, k_s is the thermal conductivity of air at the temperature of the isothermal wall, and $(\partial T/\partial x)$ is the temperature gradient in the thin layer of air in the x-direction normal to the wall. An energy balance at the thin layer of air yields,

$$q_{conduction} = q_{convection} \tag{B.2}$$

or,

$$-\, k_s \left[\frac{\partial T}{\partial x}\right]_{x=0} = h\, \Delta T \tag{B.3}$$

where, h is the convective heat transfer coefficient, and ΔT is the temperature difference between the walls. The local Nusselt is defined as,

$$Nu = \frac{hH}{k} \tag{B.4}$$

which represents a non-dimensional convective heat transfer coefficient. substituting equation (B.3) into equation (B.4),

$$Nu = \frac{k_H}{k_C} \frac{\partial (T-T_C)/(T_H-T_C)}{\partial (x/H)} \tag{B.5}$$

or,

$$Nu = \frac{k_H}{k_C} \frac{\Delta\theta}{\Delta\xi} \tag{B.6}$$

where, k_H and k_C are the thermal conductivity of air at the temperature of the hot and cold walls, respectively, θ is the non-dimensional temperature, and ξ is the non-dimensional distance normal to the wall. The non-dimensional temperature gradient at the wall ($\Delta\theta/\Delta\xi$) is evaluated from the interferograms as explained in Appendix (1) and knowing the properties of air at the temperature of the isothermal walls the local Nusselt number can be calculated.

The mean Nusselt number is then calculated by fitting a cubic spline function to the local Nusselt number values, and numerically integrating over the entire length of the wall.

APPENDIX C

ERROR ANALYSIS

Three types of errors can affect the accuracy of the experimental results of the present study, optical measurement errors, data aquisition errors and calculation errors. A qualitative assessment of the uncertainties resulting from these sources of error is discussed here to ensure the acceptability of the resuls.

Optical measurement errors are taken care of in the adjustment of the infinite field fringe setting before the experiment, where the first and the last fringes in the field must follow the sufaces of the hot and cold walls, respectively, bad experimennts were rejected based upon this criterion. However, it is estimated that about 5% error can result from this source as judged by few repeatability measurements performed on a single representative experiment.

Kline and McClintock (1953) presented a method for estimating uncertainties in single-sample experiments, where uncertainty was defined as what one thinks the error might be, and it may vary considerably depending upon the particular circumstances of the single observation. As shown in Appendix B, the local Nusselt number is a function of a number of independent variables,

$$Nu = Nu\ (H, k_H, k_C, \frac{x}{H}, \frac{\partial(T-T_C)}{\partial(x/H)}) \tag{C.1}$$

or namely, the height of the enclosure, the thermal conductivities of air at the temperature of each of the isothermal walls, the distance from the wall to the center of the fringe, and the calculated temperature gradient at the wall. Accuracy of better than 1% could be achieved in measuring wall heights and temperatures, however higher uncertainty in the last two variables was possible because of the difficulties associated with, accurately locating the center (the darkest spot) of a fringe, and the choice of the best-fit polynomial that predicts the measured data (see Appendix A) for calculating the temperature gradient at each wall.

The uncertainty in locating the fringe is estimated from repeated measurements of the same interferogram to be less than 5%. The best-fit polynomial function was selected based on the statistic R^2 discussed by Draper and Smith (1981, pp. 101-102). A third degree polynomial gave the best statistical fit, while fits obtained from fourth and fifth degree polynomials appeared statistically reasonabe too, where they gave temperature gradient values within 12% of the values of the best fit. Therefore the third degree polynomial was used in the study with an estimate of uncertainty of 12% in the temperature gradient alone.

Kline and McClintock (1953) suggested a second-power equation for an upper bound on the uncertainty in single measurements, which for the variables of the present study becomes,

$$\left[\frac{\Delta Nu}{Nu}\right]_{max} = \left[\left(\frac{\Delta k_H}{k_H}\right)^2 + \left(\frac{\Delta k_C}{k_C}\right)^2 + \left(\frac{\Delta (x/H)}{x/H}\right)^2 + \left(\frac{\Delta \dfrac{(\partial(T-T_C)}{\partial x/H}}{\dfrac{\partial(T-T_C)}{\partial x/H}}\right)^2 \right]^{1/2} \tag{C.2}$$

therefore, substituting the individual uncertainties of all independent variables in this equation yields an overall estimated uncertainty of about 14%, which was considered reasonable regarding the nature of the experimental technique.

APPENDIX D

COMPUTER PROGRAM
AND
INTERFEROMETRIC MEASUREMENTS

```
      PROGRAM ANALYSIS2
-----------------------------------------------------------------
C This program reads the interferometric measurements in data files
C with "filename, shown in Table 1,
C and then uses IMSL Library subroutines to fit a
C shape preserving polynomial function of a known order to the
C measurements at each line.
C The program then derives the local Nusselt number at the isothermal
C walls then integrates over the wall height to give the mean Nusselt
C number.
C It outputs the mean Nusselt numbers to  the termiral, and generates
C three output data files; one for the local values at tne hot wall
C with the name "PHfilename.dat", and one for the cold wall
C with the name "PCfilename.dat", and the third for statistical
C data with the name "STATfilename.dat".
-----------------------------------------------------------------
      DIMENSION THETA(100),X(100),YH(100),B(30),SSPOLY(30),STAT(10)
     &          ,CNU(100),YC(100),XD(100)
      REAL VALUE1,CSITG,BREAK(22),CSCOEF(4,22),TH,TC,CHC,DELT,DELTF
     &     ,HWHT,CWHT,XW,HNU(100),BSUM,VALUE2,XF,XP,YP,RSPNS,XO
      INTEGER NDEG,NLINE,NFRG,MLINE(100),NRSPNS
      EXTERNAL CSITG
      CHARACTER*12 FILNAM
      CHARACTER*14 CFILN,HFILN
      CHARACTER*16 STFILN,DFNAM,PFNAM
      WRITE(5,*) 'ENTER INPUT FILENAME :'
      READ(5,100) FILNAM
```

```
      WRITE(5,*) 'ENTER DEGREE OF POLYNOMIAL (integer):'
      READ(5,*) NDEG
  100 FORMAT(A)
  109 FORMAT(A,A)
  110 FORMAT(A,I2)
      OPEN(UNIT=10,NAME=FILNAM,TYPE='OLD')
      READ(10,101) NLINE
C 902 WRITE(5,*) NLINE
      READ(10,101) NFRG
      READ(10,*) TH
      READ(10,*) TC
      DELT=TH-TC
      DELTF=DELT/(NFRG+1)
      READ(10,*) CHC
      READ(10,*) HWHT
      READ(10,*) CWHT
      DO 710 L=1,(NFRG+2)
        THETA(L)= (TH - (L-1)*DELTF-TC)/DELT
C 905 WRITE(5,*) THETA(L)
  710 CONTINUE
  101 FORMAT(I2)
      WRITE(CFILN,109) 'PC',FILNAM
      WRITE(HFILN,109) 'PH',FILNAM
      WRITE(STFILN,109) 'STAT',FILNAM
      OPEN(UNIT=11,NAME=HFILN,TYPE='NEW')
      OPEN(UNIT=12,NAME=CFILN,TYPE='NEW')
      OPEN(UNIT=13,NAME=STFILN,TYPE='NEW')
```

```
C----------------------------------------------------
 700  WRITE(5,*) 'If you want the temperature profile(s) along
    + one or more lines in the interferogram, enter [the number
    + of lines]. If no temperature profiles are needed enter [0]:'
      READ(5,*) RSPNS
      IF(RSPNS.EQ.0) GO TO 600
      NRSPNS=RSPNS
      IF(NRSPNS.GT.NLINE) THEN
      WRITE(5,*) 'This number of lines exceeds the number of lines
    + in the data file.'
      GO TO 700
      ELSE
      DO 750 J=1,NRSPNS
      IF(J.NE.1) GOTO 751
      WRITE(5,*) 'Enter the first line number:'
      READ(5,*) MLINE(J)
      GO TO 750
 751  WRITE(5,*) 'Enter the next line number:'
      READ(5,*) MLINE(J)
 750  CONTINUE
      ENDIF
C----------------------------------------------------
        DO 300 I=1,NLINE
          READ(10,*) YD
          YH(I)=YD/HWHT
          YC(I)=YD/CWHT
                READ(10,*) (XD(J),J=1,NFRG+2)
```

```
      XW=XD(NFRG+2)-XD(1)
        DO 320 J=1,NFRG+2
          X(J)=(XD(J)-XD(1))/XW
320     CONTINUE
      CALL RCURV ((NFRG+2),X,THETA,NDEG,B,SSPOLY,STAT)
      WRITE(13,*) I
        DO 330 J=1,NDEG+1
          WRITE(13,*) B(J),SSPOLY(J)
330     CONTINUE
       DO 400 K=1,10
         WRITE(13,*) STAT(K)
400    CONTINUE
      HNU(I)=ABS(CHC*B(2))
        BSUM=0.0
        DO 340 J=1,NDEG
          BSUM=BSUM+J*B(J+1)
340     CONTINUE
      CNU(I)=ABS(CHC*BSUM)
      WRITE(11,*) YH(I),HNU(I)
      WRITE(12,*) YC(I),CNU(I)
      DO 720 L=1,NRSPNS
        IF(I.NE.MLINE(L)) GOTO 720
        WRITE(5,110) ' Enter a filename for the fitted curve
 + of line number ',MLINE(L)
        READ(5,100) PFNAM
        WRITE(5,110) ' Enter a filename for the actual data
 + of line nember ',MLINE(L)
```

```
        READ(5,100) DFNAM
        OPEN(UNIT=14,NAME=PFNAM,TYPE='NEW')
        OPEN(UNIT=15,NAME=DFNAM,TYPE='NEW')
       XF=1.0/100.0
        XO=0.0
       WRITE(14,*) XO,B(1)
        DO 610 J=1,100
       XP=XF*J
       YP=B(1)
       DO 620 K=2,NDEG+1
         YP=YP+B(K)*(XP**(K-1))
620    CONTINUE
       WRITE(14,*) XP,YP
610   CONTINUE
      CLOSE(14)
        DO 640 J=1,NFRG+2
          WRITE(15,*) X(J),THETA(J)
640    CONTINUE
       CLOSE(15)
720    CONTINUE
300   CONTINUE
     CLOSE(11)
     CLOSE(12)
     CLOSE(13)
     GOTO 800
C-----------------------------------------------------
600   DO 302 I=1,NLINE
```

```
      READ(10,*) YD
      YH(I)=YD/HWHT
      YC(I)=YD/CWHT
         READ(10,*) (XD(J),J=1,NFRG+2)
      XW=XD(NFRG+2)-XD(1)
        DO 322 J=1,NFRG+2
          X(J)=(XD(J)-XD(1))/XW
322     CONTINUE
      CALL RCURV ((NFRG+2),X,THETA,NDEG,B,SSPOLY,STAT)
      WRITE(13,*) I
        DO 332 J=1,NDEG+1
          WRITE(13,*) B(J),SSPOLY(J)
332     CONTINUE
        DO 402 K=1,10
          WRITE(13,*) STAT(K)
402     CONTINUE
      HNU(I)=ABS(CHC*B(2))
        BSUM=0.0
        DO 342 J=1,NDEG
          BSUM=BSUM+J*B(J+1)
342     CONTINUE
      CNU(I)=ABS(CHC*BSUM)
      WRITE(11,*) YH(I),HNU(I)
      WRITE(12,*) YC(I),CNU(I)
302   CONTINUE
    CLOSE(11)
    CLOSE(12)
```

```
      CLOSE(13)
800   CALL CSAKM (NLINE,YH,HNU,BREAK,CSCOEF)
      NINTV=NLINE-1
      VALUE1=CSITG(YH(1),YH(NLINE),NINTV,BREAK,CSCOEF)
      WRITE(5,*) 'The Mean Nusselt Number For The Hot Wall= ',VALUE1
      CALL CSAKM (NLINE,YC,CNU,BREAK,CSCOEF)
      NINTV=NLINE-1
      VALUE2=CSITG(YC(1),YC(NLINE),NINTV,BREAK,CSCOEF)
      WRITE(5,*) 'The Mean Nusselt Number For The Cold Wall = ',VALUE2
      CLOSE(10)
      END
```

Table 1: Interferometric Measurements

picture 6

```
17      ; number of lines across isothermal walls
9       ; number of fringes, excluding wall fringe
33.2    ; hot wall temperature
19.4    ; cold wall temperature
1.0415  ; ratio of thermal conductivities (hot/cold)
1.827   ; hot wall height
1.865   ; cold wall height
0.10115 ; non-dim. Y coord., followed by non-dim. X's
0.090 .114 .161 .217 .333 1.035 1.448 1.594 1.708 1.794 1.856
0.203
0.084 .112 .158 .204 .283 1.137 1.476 1.597 1.701 1.785 1.849
0.3045
0.091 .121 .166 .220 .367 1.223 1.509 1.630 1.724 1.795 1.846
0.406
0.089 .130 .185 .268 .626 1.269 1.546 1.660 1.740 1.800 1.850
0.5075
0.091 .144 .218 .370 .579 1.288 1.578 1.683 1.749 1.804 1.841
0.609
0.096 .157 .250 .374 .525 1.257 1.594 1.693 1.750 1.803 1.843
0.7105
0.097 .150 .234 .328 .446 1.206 1.597 1.693 1.747 1.800 1.835
0.812
0.098 .138 .212 .287 .391 1.114 1.591 1.685 1.744 1.795 1.830
0.9135
0.091 .128 .189 .255 .347 .919 1.567 1.665 1.731 1.788 1.832
1.015
0.082 .121 .173 .232 .312 .738 1.526 1.638 1.709 1.779 1.833
1.1165
0.086 .116 .165 .220 .295 .611 1.466 1.595 1.683 1.765 1.833
1.218
0.088 .114 .164 .220 .286 .542 1.348 1.545 1.650 1.753 1.825
1.3195
0.080 .111 .167 .219 .296 .485 1.252 1.501 1.651 1.758 1.828
1.421
0.082 .111 .121 .237 .320 .487 1.207 1.522 1.702 1.778 1.823
1.5225
0.084 .117 .184 .268 .361 .513 1.167 1.664 1.741 1.795 1.825
1.624
0.081 .129 .205 .303 .401 .545 1.193 1.701 1.757 1.808 1.828
1.7255
0.081 .120 .209 .314 .427 .593 1.559 1.701 1.760 1.808 1.830
```

Table 1 (cont'd)

picture 1

17
10
33.2
19.4
1.0415
1.8
1.809
0.1
0.056 .098 .189 .312 .465 .848 1.470 1.675 1.767 1.829 1.876 1.912
0.2
0.051 .112 .231 .362 .550 1.256 1.635 1.732 1.791 1.837 1.878 1.912
0.3
0.053 .113 .241 .394 .666 1.439 1.671 1.740 1.793 1.834 1.876 1.912
0.4
0.054 .119 .254 .432 .721 1.507 1.675 1.740 1.789 1.832 1.873 1.912
0.5
0.056 .118 .246 .404 .626 1.055 1.660 1.731 1.780 1.825 1.869 1.912
0.6
0.055 .119 .224 .345 .502 .801 1.640 1.716 1.772 1.819 1.865 1.914
0.7
0.056 .110 .199 .296 .413 .601 1.602 1.694 1.756 1.807 1.857 1.914
0.8
0.053 .104 .180 .258 .354 .480 1.550 1.662 1.736 1.796 1.852 1.912
0.9
0.055 .101 .167 .231 .308 .403 1.480 1.616 1.707 1.777 1.844 1.914
1.0
0.057 .100 .156 .212 .276 .355 1.361 1.556 1.666 1.755 1.835 1.914
1.1
0.056 .096 .146 .196 .252 .320 .442 1.457 1.606 1.722 1.821 1.917
1.2
0.058 .095 .141 .186 .236 .296 .405 1.322 1.529 1.684 1.803 1.922
1.3
0.059 .091 .133 .175 .222 .278 .384 1.153 1.424 1.635 1.791 1.926
1.4
0.058 .088 .128 .170 .217 .274 .377 1.007 1.364 1.616 1.791 1.930
1.5
0.059 .088 .128 .171 .219 .279 .401 .922 1.419 1.654 1.803 1.934
1.6
0.059 .090 .131 .177 .232 .314 .486 .978 1.492 1.685 1.819 1.943
1.7
0.059 .092 .139 .198 .283 .419 .704 1.186 1.553 1.717 1.837 1.946

Table 1 (cont'd)

picture 4

17
10
33.2
19.4
1.0415
2.563
2.596
0.142389
0.0 .25 .547 1.013 1.338 1.604 1.973 2.258 2.421 2.514 2.578 2.604
0.284778
0.0 .246 .486 1.363 1.649 1.909 2.266 2.405 2.494 2.541 2.585 2.605
0.427166
0.0 .156 .285 1.109 1.849 2.173 2.382 2.465 2.524 2.568 2.597 2.609
0.569555
0.0 .102 .186 .261 .390 1.789 2.421 2.488 2.533 2.566 2.582 2.603
0.711944
0.0 .085 .143 .211 .299 .969 2.427 2.493 2.525 2.558 2.577 2.603
0.854333
0.0 .067 .122 .180 .245 1.117 2.415 2.487 2.517 2.549 2.577 2.601
0.996722
0.0 .060 .108 .162 .215 .293 .398 2.477 2.506 2.546 2.575 2.599
1.139110
0.0 .048 .093 .147 .187 .264 .348 2.462 2.495 2.539 2.571 2.598
1.281499
0.0 .039 .091 .130 .171 .236 .317 2.435 2.484 2.526 2.564 2.599
1.423888
0.0 .039 .087 .124 .161 .215 .288 2.419 2.471 2.517 2.556 2.601
1.566277
0.0 .040 .091 .127 .156 .200 .269 .969 2.452 2.505 2.554 2.601
1.708666
0.0 .037 .090 .127 .152 .192 .263 1.180 2.428 2.491 2.548 2.599
1.851054
0.0 .039 .088 .124 .155 .195 .273 .436 .854 2.463 2.531 2.599
1.993443
0.0 .046 .089 .124 .157 .214 .289 .491 .784 2.426 2.504 2.597
2.135832
0.0 .05 .089 .134 .174 .247 .365 .598 .865 2.342 2.46 2.598
2.278221
0.0 .058 .103 .158 .224 .323 .516 .785 1.019 2.175 2.388 2.597
2.42061
0.0 .058 .117 .191 .298 .482 .748 1.008 1.336 1.78 2.339 2.596

Table 1 (cont'd)

picture 7

17
9
32.4
19.5
1.0388
1.925
1.946
0.10694
0.057 .097 .157 .246 .475 1.000 1.375 1.568 1.697 1.810 1.895
0.21389
0.056 .100 .159 .240 .421 .820 1.474 1.605 1.711 1.814 1.896
0.32083
0.059 .110 .181 .285 .485 .728 1.532 1.649 1.759 1.834 1.899
0.42778
0.065 .135 .221 .360 .482 .645 1.598 1.717 1.796 1.852 1.900
0.53472
0.065 .147 .251 .348 .439 .576 1.648 1.750 1.812 1.859 1.897
0.64167
0.063 .144 .227 .305 .386 .525 1.693 1.771 1.822 1.865 1.897
0.74861
0.062 .129 .190 .260 .328 .479 1.710 1.769 1.824 1.864 1.897
0.85556
0.059 .108 .164 .223 .288 .425 1.714 1.771 1.818 1.862 1.897
0.9625
0.057 .101 .148 .198 .260 .721 1.711 1.767 1.808 1.860 1.894
1.06944
0.057 .097 .139 .184 .249 1.583 1.684 1.751 1.808 1.853 1.894
1.17638
0.057 .095 .137 .185 .251 1.540 1.656 1.723 1.786 1.845 1.893
1.28333
0.058 .096 .140 .191 .269 1.506 1.608 1.682 1.754 1.833 1.892
1.39028
0.059 .099 .147 .206 .301 1.446 1.553 1.640 1.727 1.823 1.892
1.49722
0.060 .107 .165 .240 .357 1.387 1.515 1.626 1.738 1.833 1.894
1.60417
0.062 .126 .197 .301 .416 1.333 1.504 1.684 1.786 1.863 1.904
1.71111
0.072 .155 .246 .356 .472 1.309 1.584 1.742 1.821 1.879 1.912
1.81805
0.070 .164 .286 .397 .551 1.141 1.592 1.751 1.827 1.884 1.912

Table 1 (cont'd)

picture 8

17
10
32.4
19.5
1.0388
1.861
1.864
0.10339
0.038 .086 .184 .302 .484 .935 1.409 1.692 1.806 1.878 1.934 1.981
0.20678
0.037 .108 .215 .336 .564 1.069 1.562 1.742 1.821 1.880 1.931 1.981
0.31017
0.041 .128 .245 .410 .689 1.146 1.632 1.759 1.830 1.884 1.934 1.982
0.41356
0.045 .140 .272 .452 .674 1.163 1.647 1.771 1.834 1.885 1.934 1.983
0.51694
0.047 .141 .261 .395 .573 1.124 1.653 1.772 1.835 1.885 1.933 1.984
0.62033
0.053 .131 .228 .335 .484 1.075 1.659 1.772 1.834 1.883 1.933 1.984
0.72372
0.054 .119 .201 .290 .412 .911 1.633 1.761 1.828 1.881 1.932 1.980
0.82711
0.058 .108 .180 .257 .366 .765 1.595 1.748 1.821 1.878 1.931 1.983
0.9305
0.057 .109 .173 .242 .330 .591 1.559 1.724 1.806 1.871 1.929 1.985
1.03389
0.053 .107 .164 .225 .306 .514 1.489 1.690 1.787 1.859 1.926 1.985
1.13728
0.058 .111 .165 .219 .297 .470 1.417 1.647 1.762 1.849 1.925 1.986
1.24067
0.073 .124 .175 .229 .303 .472 1.314 1.599 1.736 1.841 1.931 2.005
1.34405
0.073 .126 .176 .230 .299 .467 1.159 1.511 1.685 1.816 1.925 2.010
1.44744
0.074 .129 .178 .232 .307 .469 1.056 1.417 1.626 1.797 1.918 2.013
1.55083
0.077 .131 .182 .239 .321 .503 .975 1.384 1.650 1.817 1.932 2.018
1.65422
0.079 .133 .188 .251 .350 .569 1.011 1.471 1.708 1.847 1.944 2.022
1.75761
0.085 .138 .200 .283 .425 .707 1.122 1.559 1.741 1.869 1.962 2.028

Table 1 (cont'd)

picture 8a

17
8
32.4
19.5
1.0388
1.873
1.884
0.10406
0.036 .109 .253 .922 1.373 1.562 1.737 1.861 1.946 1.991
0.20811
0.045 .155 .312 .498 1.474 1.622 1.789 1.880 1.949 1.991
0.31217
0.049 .161 .263 .364 1.576 1.767 1.861 1.911 1.957 1.991
0.41622
0.052 .142 .222 .295 .385 .547 1.888 1.926 1.960 1.990
0.52028
0.054 .120 .187 .247 .319 .415 1.898 1.932 1.961 1.991
0.62433
0.053 .105 .160 .214 .269 .338 1.902 1.932 1.961 1.990
0.72839
0.052 .096 .141 .187 .235 .288 1.902 1.932 1.958 1.984
0.83244
0.053 .085 .126 .161 .205 1.862 1.893 1.924 1.951 1.975
0.9365
0.056 .084 .116 .152 .188 1.848 1.883 1.915 1.946 1.972
1.04056
0.057 .082 .114 .142 1.778 1.828 1.867 1.903 1.937 1.968
1.14461
0.055 .083 .110 .141 1.742 1.800 1.846 1.890 1.929 1.962
1.24867
0.055 .082 .109 .139 1.696 1.766 1.816 1.867 1.913 1.956
1.35272
0.054 .082 .112 .144 1.626 1.717 1.782 1.837 1.897 1.951
1.45678
0.054 .083 .117 .153 1.514 1.662 1.739 1.804 1.872 1.947
1.56083
0.052 .087 .132 .175 .249 .399 1.677 1.759 1.841 1.935
1.66489
0.052 .093 .154 .232 .370 .516 1.574 1.703 1.816 1.929
1.76894
0.048 .105 .199 .326 .471 .617 .790 1.618 1.804 1.931

Table 1 (cont'd)

picture 13

17
9
33.2
19.4
1.0415
1.808
1.848
0.10044
0.035 .066 .136 .268 .581 .927 1.243 1.420 1.580 1.688 1.767
0.20089
0.035 .079 .166 .358 .684 1.014 1.302 1.487 1.630 1.713 1.774
0.30133
0.034 .097 .209 .460 .751 1.086 1.385 1.576 1.674 1.730 1.774
0.40178
0.034 .114 .235 .450 .773 1.143 1.475 1.624 1.689 1.736 1.773
0.50222
0.035 .122 .236 .400 .763 1.132 1.517 1.631 1.690 1.737 1.772
0.60267
0.034 .123 .223 .356 .694 1.120 1.515 1.630 1.689 1.736 1.773
0.70311
0.034 .113 .201 .308 .606 1.120 1.490 1.618 1.683 1.730 1.772
0.80356
0.032 .100 .177 .263 .529 1.087 1.451 1.596 1.669 1.721 1.771
0.904
0.033 .090 .154 .228 .434 1.066 1.410 1.567 1.651 1.710 1.763
1.00444
0.035 .081 .134 .201 .360 1.020 1.372 1.544 1.631 1.701 1.761
1.10489
0.034 .073 .118 .177 .297 .931 1.322 1.508 1.608 1.690 1.761
1.20533
0.035 .069 .109 .165 .265 .844 1.270 1.463 1.586 1.678 1.762
1.30578
0.033 .062 .106 .156 .256 .757 1.189 1.424 1.567 1.671 1.760
1.40622
0.033 .062 .107 .162 .264 .630 1.121 1.383 1.559 1.668 1.762
1.50667
0.042 .077 .121 .195 .331 .615 1.061 1.352 1.579 1.691 1.770
1.60711
0.049 .091 .153 .262 .414 .643 1.054 1.380 1.608 1.717 1.780
1.70755
0.054 .116 .210 .341 .494 .700 1.104 1.465 1.645 1.734 1.782

Table 1 (cont'd)

picture 12

17
11
33.2
19.4
1.0415
1.748
1.775
0.09711
0.025 .097 .196 .359 .639 .942 1.198 1.427 1.586 1.692 1.763 1.817 1.850
0.19422
0.026 .114 .222 .404 .739 1.035 1.268 1.457 1.595 1.688 1.756 1.812 1.849
0.29133
0.026 .123 .241 .426 .746 1.071 1.282 1.460 1.598 1.685 1.752 1.809 1.845
0.38844
0.025 .135 .265 .429 .690 1.060 1.281 1.461 1.593 1.683 1.749 1.805 1.843
0.48556
0.025 .142 .274 .408 .628 1.025 1.272 1.447 1.586 1.680 1.746 1.805 1.840
0.58267
0.024 .136 .255 .376 .572 .957 1.250 1.431 1.574 1.672 1.739 1.799 1.835
0.67978
0.023 .122 .227 .336 .510 .883 1.217 1.415 1.557 1.657 1.731 1.794 1.835
0.77689
0.027 .101 .196 .302 .452 .780 1.180 1.391 1.535 1.644 1.723 1.792 1.835
0.874
0.017 .092 .173 .267 .404 .688 1.125 1.370 1.516 1.625 1.712 1.784 1.833
0.97111
0.017 .088 .157 .247 .374 .622 1.066 1.331 1.490 1.602 1.695 1.777 1.832
1.06822
0.019 .084 .151 .231 .351 .567 .967 1.292 1.458 1.575 1.676 1.768 1.828
1.16533
0.019 .084 .145 .224 .337 .527 .826 1.229 1.428 1.550 1.655 1.760 1.832
1.26244
0.021 .082 .142 .219 .323 .482 .735 1.118 1.392 1.532 1.643 1.757 1.829
1.35956
0.021 .080 .140 .218 .317 .462 .675 .981 1.353 1.515 1.645 1.757 1.833
1.45667
0.020 .076 .135 .215 .314 .443 .635 .889 1.278 1.512 1.665 1.766 1.838
1.55378
0.013 .072 .133 .211 .311 .448 .630 .836 1.169 1.493 1.673 1.773 1.842
1.65089
0.010 .060 .120 .206 .316 .466 .672 .886 1.163 1.468 1.677 1.780 1.847

Table 1 (cont'd)

picture 12a

17
9
33.2
19.4
1.0415
1.790
1.790
0.09794
0.032 .054 .131 .316 .800 1.343 1.570 1.697 1.782 1.847 1.892
0.19589
0.034 .076 .203 .451 1.054 1.515 1.668 1.753 1.808 1.856 1.892
0.29383
0.039 .097 .238 .408 1.282 1.653 1.738 1.790 1.829 1.865 1.892
0.39178
0.046 .101 .223 .343 .549 1.710 1.765 1.802 1.835 1.864 1.892
0.48972
0.046 .097 .196 .293 .424 1.719 1.767 1.804 1.835 1.865 1.892
0.58767
0.048 .093 .174 .252 .352 1.710 1.759 1.797 1.832 1.863 1.891
0.68561
0.053 .090 .155 .224 .300 1.685 1.742 1.786 1.823 1.858 1.889
0.78356
0.051 .085 .138 .198 .263 1.652 1.721 1.769 1.810 1.850 1.887
0.8815
0.055 .087 .131 .181 .239 .318 1.694 1.749 1.795 1.840 1.885
0.97944
0.058 .088 .125 .169 .219 .283 1.659 1.726 1.778 1.830 1.882
1.07739
0.059 .086 .120 .159 .202 .257 1.618 1.700 1.759 1.819 1.880
1.17533
0.059 .085 .116 .150 .188 .237 1.571 1.669 1.739 1.806 1.876
1.27328
0.058 .085 .114 .146 .181 .226 1.486 1.627 1.709 1.789 1.872
1.37122
0.060 .087 .114 .145 .182 .228 .328 1.577 1.678 1.768 1.866
1.46917
0.059 .086 .117 .152 .194 .253 .383 1.494 1.633 1.745 1.860
1.56711
0.057 .087 .127 .173 .233 .330 .500 .966 1.583 1.732 1.859
1.66505
0.058 .093 .154 .227 .321 .454 .642 .995 1.552 1.767 1.859

Table 1 (cont'd)

picture 21

17
9
32.2
19.4
1.0386
1.91
1.952
0.10611
0.043 .113 .231 .448 .733 1.028 1.310 1.508 1.676 1.816 1.887
0.21222
0.049 .137 .286 .534 .794 1.044 1.282 1.466 1.632 1.785 1.876
0.31833
0.048 .171 .360 .592 .851 1.099 1.313 1.484 1.640 1.786 1.871
0.42444
0.059 .203 .405 .639 .901 1.149 1.346 1.510 1.652 1.784 1.871
0.53056
0.061 .218 .428 .673 .948 1.175 1.373 1.529 1.658 1.782 1.876
0.63667
0.058 .235 .448 .692 .967 1.197 1.393 1.545 1.668 1.780 1.872
0.74278
0.054 .233 .454 .701 .955 1.209 1.411 1.559 1.678 1.780 1.872
0.84889
0.052 .231 .452 .700 .976 1.239 1.428 1.567 1.682 1.784 1.864
0.955
0.049 .231 .441 .682 .972 1.241 1.435 1.574 1.687 1.789 1.862
1.06111
0.052 .217 .424 .638 .936 1.234 1.428 1.573 1.680 1.789 1.862
1.16722
0.050 .203 .380 .591 .859 1.173 1.406 1.559 1.676 1.788 1.863
1.27333
0.046 .184 .338 .522 .771 1.065 1.354 1.535 1.665 1.784 1.861
1.37944
0.039 .163 .294 .445 .663 .941 1.255 1.491 1.643 1.771 1.854
1.48556
0.033 .143 .263 .396 .584 .828 1.151 1.426 1.625 1.768 1.854
1.59167
0.028 .131 .252 .376 .548 .770 1.068 1.366 1.606 1.770 1.861
1.69778
0.025 .125 .251 .385 .567 .786 1.087 1.384 1.630 1.786 1.861
1.80389
0.013 .106 .255 .392 .591 .845 1.159 1.449 1.681 1.808 1.864

Table 1 (cont'd)

picture 19

17
9
32.2
19.4
1.0386
1.863
1.863
0.1035
0.026 .097 .218 .372 .607 .892 1.167 1.440 1.680 1.850 1.958
0.207
0.027 .117 .254 .405 .640 .898 1.146 1.391 1.628 1.821 1.958
0.3105
0.027 .118 .257 .430 .663 .923 1.166 1.395 1.629 1.808 1.958
0.414
0.027 .127 .276 .465 .710 .972 1.217 1.448 1.661 1.816 1.957
0.5175
0.027 .137 .302 .494 .761 1.039 1.285 1.504 1.680 1.825 1.958
0.621
0.028 .151 .323 .529 .812 1.089 1.336 1.536 1.697 1.829 1.957
0.7245
0.031 .156 .336 .550 .839 1.125 1.372 1.559 1.700 1.829 1.957
0.828
0.032 .159 .350 .578 .865 1.142 1.403 1.570 1.710 1.829 1.956
0.9315
0.035 .173 .368 .590 .870 1.159 1.415 1.576 1.709 1.831 1.960
1.035
0.038 .186 .381 .600 .864 1.145 1.406 1.574 1.706 1.830 1.959
1.1385
0.040 .200 .380 .585 .829 1.119 1.384 1.562 1.704 1.832 1.960
1.242
0.043 .204 .377 .559 .784 1.062 1.336 1.547 1.700 1.828 1.963
1.3455
0.047 .201 .363 .527 .726 .991 1.274 1.520 1.690 1.830 1.968
1.449
0.041 .187 .344 .495 .689 .923 1.223 1.493 1.682 1.834 1.969
1.5525
0.041 .181 .334 .496 .671 .888 1.184 1.474 1.693 1.842 1.976
1.656
0.041 .159 .316 .475 .659 .881 1.174 1.470 1.695 1.851 1.980
1.7595
0.036 .123 .254 .421 .627 .874 1.189 1.497 1.731 1.874 1.986

Table 1 (cont'd)

picture 18

17
9
32.2
19.4
1.0386
1.933
1.933
0.10739
0.031 .146 .326 .532 .793 1.058 1.369 1.612 1.758 1.851 1.907
0.21478
0.056 .232 .427 .639 .879 1.107 1.364 1.573 1.731 1.831 1.902
0.32217
0.060 .231 .425 .631 .860 1.084 1.321 1.526 1.693 1.807 1.896
0.42956
0.058 .228 .417 .636 .855 1.069 1.293 1.496 1.661 1.785 1.895
0.53694
0.051 .226 .427 .641 .870 1.090 1.309 1.497 1.657 1.777 1.889
0.64433
0.055 .231 .427 .635 .871 1.097 1.332 1.514 1.657 1.781 1.882
0.75172
0.055 .223 .418 .646 .876 1.109 1.341 1.530 1.660 1.781 1.882
0.85911
0.054 .217 .412 .621 .870 1.107 1.350 1.527 1.659 1.775 1.880
0.9665
0.050 .211 .390 .609 .846 1.090 1.341 1.519 1.655 1.775 1.876
1.07389
0.050 .206 .377 .569 .801 1.055 1.309 1.502 1.641 1.764 1.875
1.18128
0.050 .182 .351 .535 .754 1.001 1.254 1.471 1.623 1.754 1.874
1.28867
0.042 .179 .327 .500 .701 .934 1.200 1.436 1.608 1.751 1.874
1.39605
0.043 .158 .295 .459 .646 .868 1.127 1.388 1.587 1.751 1.875
1.50344
0.038 .139 .268 .415 .591 .794 1.050 1.323 1.561 1.742 1.874
1.61083
0.035 .121 .223 .352 .531 .731 .982 1.269 1.522 1.726 1.872
1.71822
0.029 .101 .186 .308 .474 .686 .934 1.230 1.488 1.701 1.873
1.82561
0.029 .088 .167 .280 .462 .705 .995 1.320 1.571 1.770 1.887

Table 1 (cont'd)

picture 20

17
9
32.2
19.4
1.0386
1.859
1.884
0.103278
0.079 .103 .220 .462 .756 1.151 1.485 1.748 1.883 1.977 2.016
0.206555
0.084 .162 .346 .634 .977 1.288 1.542 1.728 1.852 1.946 2.018
0.30983
0.090 .212 .448 .745 1.068 1.353 1.554 1.720 1.842 1.935 2.017
0.41311
0.093 .234 .478 .763 1.086 1.347 1.533 1.697 1.823 1.920 2.010
0.516389
0.096 .244 .475 .750 1.059 1.324 1.511 1.675 1.804 1.909 2.010
0.619667
0.097 .240 .451 .726 1.030 1.299 1.494 1.659 1.786 1.894 2.002
0.722944
0.099 .239 .446 .711 1.026 1.295 1.495 1.653 1.777 1.889 1.998
0.826222
0.099 .233 .435 .697 1.010 1.286 1.495 1.650 1.773 1.883 1.994
0.9295
0.096 .227 .421 .663 .964 1.251 1.479 1.644 1.773 1.880 1.984
1.03278
0.093 .218 .391 .611 .875 1.199 1.451 1.631 1.760 1.868 1.987
1.13605
0.090 .210 .363 .556 .799 1.128 1.412 1.604 1.746 1.863 1.984
1.23933
0.087 .198 .327 .492 .718 1.019 1.340 1.571 1.727 1.856 1.987
1.34261
0.086 .184 .293 .432 .619 .884 1.212 1.515 1.704 1.844 1.989
1.44589
0.083 .165 .259 .376 .532 .770 1.077 1.421 1.671 1.832 1.988
1.54917
0.080 .153 .231 .332 .472 .673 .935 1.285 1.598 1.811 1.987
1.65244
0.073 .141 .217 .308 .439 .621 .862 1.173 1.517 1.791 1.987
1.75572
0.072 .136 .219 .323 .471 .673 .928 1.242 1.543 1.819 1.992

Table 1 (cont'd)

picture 24

17
10
32.9
19.2
1.0413
1.825
1.841
0.10139
0.032 .082 .166 .324 .584 .842 1.073 1.273 1.436 1.566 1.687 1.784
0.20278
0.032 .102 .216 .406 .646 .874 1.084 1.260 1.410 1.550 1.670 1.777
0.30417
0.041 .133 .280 .484 .715 .932 1.131 1.295 1.439 1.566 1.678 1.773
0.40556
0.042 .163 .335 .547 .773 .994 1.172 1.332 1.465 1.581 1.682 1.771
0.50694
0.043 .185 .366 .585 .827 1.029 1.207 1.357 1.487 1.594 1.687 1.770
0.60833
0.045 .198 .392 .616 .860 1.064 1.243 1.385 1.505 1.604 1.695 1.770
0.70972
0.046 .211 .415 .642 .873 1.097 1.276 1.408 1.522 1.615 1.695 1.770
0.81111
0.046 .224 .427 .650 .888 1.120 1.289 1.422 1.528 1.617 1.697 1.768
0.9125
0.050 .227 .431 .648 .891 1.126 1.294 1.428 1.532 1.619 1.695 1.767
1.01389
0.055 .221 .400 .602 .847 1.095 1.288 1.422 1.531 1.618 1.696 1.767
1.11528
0.064 .205 .356 .594 .764 1.024 1.249 1.399 1.516 1.608 1.691 1.766
1.21667
0.065 .186 .317 .476 .681 .920 1.173 1.351 1.495 1.595 1.682 1.766
1.31805
0.058 .167 .274 .406 .587 .808 1.067 1.286 1.459 1.579 1.679 1.766
1.41944
0.054 .154 .249 .358 .513 .702 .946 1.202 1.408 1.555 1.673 1.772
1.52083
0.054 .145 .233 .333 .467 .646 .872 1.120 1.358 1.544 1.679 1.777
1.62222
0.054 .141 .239 .344 .482 .649 .872 1.119 1.369 1.562 1.695 1.778
1.72361
0.049 .134 .241 .355 .514 .696 .929 1.196 1.430 1.612 1.720 1.779

Table 1 (cont'd)

picture 23

17
10
32.9
19.2
1.0413
1.749
1.787
0.09717
0.057 .131 .243 .400 .649 .892 1.133 1.359 1.581 1.744 1.841 1.871
0.19433
0.058 .151 .268 .421 .644 .879 1.085 1.282 1.495 1.681 1.819 1.872
0.2915
0.052 .157 .286 .452 .668 .887 1.084 1.278 1.490 1.667 1.803 1.870
0.38867
0.048 .168 .314 .494 .720 .934 1.136 1.328 1.526 1.679 1.797 1.872
0.48583
0.048 .179 .337 .535 .771 .987 1.192 1.384 1.559 1.691 1.793 1.871
0.583
0.046 .187 .358 .580 .813 1.029 1.246 1.430 1.578 1.698 1.793 1.866
0.68017
0.043 .186 .368 .598 .843 1.067 1.279 1.453 1.588 1.698 1.790 1.860
0.77733
0.042 .192 .389 .622 .870 1.097 1.322 1.468 1.592 1.701 1.792 1.862
0.8745
0.040 .192 .392 .627 .867 1.113 1.328 1.474 1.592 1.695 1.788 1.859
0.97167
0.040 .190 .382 .610 .857 1.097 1.310 1.465 1.587 1.693 1.786 1.863
1.06883
0.041 .191 .369 .574 .797 1.062 1.273 1.444 1.574 1.688 1.783 1.870
1.166
0.045 .183 .342 .517 .726 .973 1.211 1.409 1.562 1.678 1.780 1.872
1.26317
0.041 .169 .312 .470 .652 .881 1.122 1.353 1.534 1.669 1.775 1.872
1.36033
0.040 .156 .290 .433 .601 .813 1.051 1.3 1.509 1.655 1.772 1.874
1.4575
0.040 .142 .268 .407 .570 .764 1.001 1.242 1.474 1.647 1.772 1.875
1.55467
0.040 .126 .246 .383 .553 .751 .979 1.216 1.457 1.646 1.769 1.872
1.65183
0.037 .095 .200 .345 .508 .718 .956 1.211 1.466 1.652 1.779 1.888

Table 1 (cont'd)

picture 25

17
9
32.9
19.2
1.0413
1.834
1.834
0.10189
0.070 .189 .386 .611 .887 1.131 1.397 1.573 1.687 1.761 1.810
0.20378
0.088 .265 .463 .693 .941 1.146 1.363 1.532 1.656 1.746 1.804
0.30567
0.085 .281 .481 .717 .938 1.142 1.336 1.498 1.626 1.731 1.802
0.40756
0.082 .292 .498 .728 .947 1.144 1.322 1.494 1.613 1.721 1.804
0.50944
0.077 .303 .515 .747 .976 1.170 1.352 1.506 1.619 1.718 1.803
0.61133
0.074 .316 .534 .766 .995 1.194 1.382 1.520 1.626 1.719 1.801
0.71322
0.072 .305 .531 .773 .999 1.209 1.399 1.528 1.629 1.721 1.801
0.81511
0.072 .301 .524 .773 1.009 1.214 1.398 1.527 1.627 1.717 1.798
0.917
0.080 .283 .488 .742 .991 1.196 1.390 1.519 1.623 1.714 1.797
1.0189
0.082 .260 .448 .673 .924 1.158 1.359 1.500 1.607 1.707 1.803
1.12078
0.080 .235 .408 .602 .851 1.081 1.319 1.473 1.590 1.696 1.798
1.22267
0.075 .208 .362 .540 .759 .998 1.246 1.436 1.569 1.688 1.794
1.32455
0.069 .182 .323 .479 .677 .911 1.169 1.389 1.544 1.681 1.797
1.42644
0.059 .158 .279 .424 .606 .817 1.076 1.330 1.511 1.670 1.798
1.52833
0.055 .137 .240 .366 .538 .743 1.003 1.262 1.479 1.658 1.797
1.63022
0.052 .120 .204 .316 .477 .682 .935 1.203 1.440 1.633 1.798
1.73211
0.048 .103 .179 .283 .439 .678 .981 1.275 1.515 1.701 1.820

Table 1 (cont'd)

picture 22

17
10
32.9
19.2
1.0413
1.769
1.778
0.09828
0.059 .081 .164 .319 .590 .942 1.280 1.523 1.700 1.802 1.877 1.913
0.19656
0.065 .118 .259 .482 .766 1.057 1.323 1.537 1.684 1.787 1.869 1.914
0.29483
0.075 .148 .353 .577 .857 1.124 1.357 1.525 1.674 1.780 1.863 1.914
0.39311
0.077 .184 .386 .614 .884 1.127 1.337 1.509 1.651 1.763 1.858 1.913
0.49139
0.083 .183 .398 .624 .894 1.125 1.331 1.500 1.642 1.758 1.851 1.912
0.58967
0.088 .205 .411 .642 .912 1.150 1.342 1.515 1.644 1.751 1.847 1.908
0.68794
0.088 .209 .413 .663 .932 1.169 1.371 1.531 1.651 1.755 1.845 1.905
0.78622
0.086 .198 .403 .663 .938 1.185 1.390 1.539 1.656 1.755 1.838 1.903
0.8845
0.086 .202 .394 .638 .914 1.153 1.382 1.536 1.659 1.756 1.837 1.902
0.98278
0.091 .200 .376 .591 .851 1.114 1.353 1.527 1.649 1.753 1.832 1.901
1.08105
0.089 .188 .341 .524 .777 1.049 1.307 1.493 1.632 1.741 1.827 1.898
1.17933
0.092 .178 .307 .464 .684 .959 1.226 1.448 1.606 1.728 1.817 1.897
1.27761
0.087 .164 .272 .401 .583 .836 1.113 1.369 1.571 1.707 1.815 1.895
1.37589
0.087 .151 .237 .348 .497 .728 .995 1.259 1.500 1.683 1.804 1.897
1.47417
0.089 .142 .212 .305 .434 .629 .879 1.145 1.409 1.643 1.800 1.897
1.57244
0.082 .134 .202 .286 .408 .585 .819 1.072 1.349 1.607 1.790 1.895
1.67072
0.085 .133 .204 .294 .437 .629 .875 1.147 1.422 1.661 1.828 1.899

Table 1 (cont'd)

picture 28

17
10
32.1
19.4
1.0383
1.914
1.938
0.10633
0.073 .107 .188 .321 .555 .841 1.110 1.366 1.563 1.716 1.841 1.920
0.21267
0.073 .122 .220 .382 .616 .884 1.113 1.333 1.524 1.682 1.825 1.914
0.319
0.073 .142 .269 .452 .689 .948 1.172 1.369 1.549 1.695 1.829 1.909
0.42533
0.074 .169 .324 .534 .773 1.024 1.236 1.425 1.584 1.719 1.837 1.909
0.53167
0.077 .193 .384 .629 .880 1.110 1.302 1.480 1.624 1.736 1.841 1.909
0.638
0.081 .219 .449 .733 .971 1.188 1.374 1.526 1.651 1.747 1.844 1.905
0.74433
0.080 .247 .517 .807 1.038 1.251 1.423 1.561 1.671 1.759 1.850 1.902
0.85066
0.078 .289 .580 .852 1.088 1.296 1.449 1.574 1.679 1.765 1.848 1.907
0.957
0.082 .292 .586 .881 1.108 1.316 1.461 1.577 1.678 1.766 1.849 1.903
1.06333
0.086 .282 .536 .834 1.099 1.305 1.452 1.577 1.680 1.764 1.851 1.899
1.1697
0.084 .254 .460 .744 1.005 1.261 1.422 1.561 1.669 1.760 1.848 1.905
1.276
0.080 .222 .386 .622 .895 1.164 1.360 1.522 1.652 1.753 1.848 1.902
1.38233
0.084 .199 .335 .516 .765 1.041 1.281 1.472 1.624 1.740 1.844 1.898
1.48867
0.083 .181 .294 .444 .639 .910 1.175 1.404 1.592 1.725 1.845 1.904
1.595
0.080 .163 .273 .397 .570 .814 1.082 1.327 1.542 1.711 1.845 1.9
1.70133
0.075 .161 .265 .382 .538 .771 1.034 1.296 1.530 1.729 1.860 1.909
1.80767
0.070 .148 .261 .395 .561 .798 1.069 1.363 1.590 1.772 1.880 1.909

Table 1 (cont'd)

picture 29

17
9
32.1
19.4
1.0383
1.86
1.86
0.10333
0.122 .216 .367 .574 .898 1.187 1.463 1.679 1.857 1.976 2.024
0.20667
0.128 .250 .392 .616 .905 1.166 1.393 1.617 1.802 1.951 2.024
0.31
0.139 .267 .432 .658 .946 1.192 1.425 1.642 1.814 1.951 2.024
0.41333
0.143 .295 .488 .756 1.039 1.270 1.479 1.680 1.820 1.939 2.024
0.51667
0.146 .326 .558 .851 1.129 1.346 1.536 1.705 1.831 1.944 2.024
0.62
0.143 .360 .632 .934 1.187 1.407 1.586 1.724 1.843 1.943 2.025
0.72333
0.158 .386 .689 .984 1.214 1.450 1.606 1.726 1.845 1.939 2.024
0.82667
0.155 .416 .730 1.019 1.272 1.461 1.615 1.735 1.839 1.937 2.016
0.93
0.142 .399 .716 1.011 1.256 1.461 1.611 1.729 1.835 1.928 2.009
1.03333
0.136 .379 .665 .971 1.226 1.437 1.594 1.714 1.826 1.923 2.009
1.13667
0.130 .344 .589 .873 1.157 1.388 1.559 1.694 1.802 1.915 2.010
1.24
0.120 .295 .494 .740 1.069 1.286 1.502 1.660 1.792 1.910 2.012
1.34333
0.117 .264 .432 .630 .903 1.180 1.415 1.609 1.763 1.897 2.017
1.44667
0.113 .234 .382 .549 .770 1.046 1.332 1.556 1.737 1.880 2.010
1.55
0.110 .218 .351 .504 .702 .973 1.259 1.5 1.711 1.868 2.009
1.65333
0.105 .201 .332 .472 .661 .892 1.201 1.463 1.708 1.863 2.008
1.75667
0.098 .171 .287 .434 .631 .912 1.190 1.478 1.726 1.892 2.017

Table 1 (cont'd)

picture 31

17
8
32.1
19.4
1.0383
1.928
1.928
0.10711
0.094 .221 .381 .656 .988 1.384 1.652 1.816 1.917 1.949
0.21422
0.096 .263 .439 .703 1.006 1.341 1.589 1.772 1.891 1.951
0.32133
0.107 .274 .472 .735 1.019 1.316 1.565 1.736 1.867 1.958
0.42844
0.108 .292 .513 .799 1.079 1.341 1.572 1.733 1.859 1.957
0.53556
0.097 .333 .568 .877 1.153 1.410 1.596 1.741 1.860 1.952
0.64267
0.096 .359 .646 .950 1.223 1.461 1.627 1.747 1.861 1.950
0.74978
0.097 .372 .733 1.015 1.277 1.489 1.637 1.753 1.854 1.947
0.85689
0.099 .363 .734 1.048 1.294 1.497 1.642 1.752 1.851 1.943
0.964
0.098 .348 .711 1.045 1.294 1.496 1.633 1.745 1.847 1.943
1.07111
0.090 .315 .641 .977 1.238 1.460 1.611 1.734 1.837 1.944
1.17822
0.090 .268 .526 .873 1.154 1.410 1.578 1.718 1.827 1.944
1.28533
0.088 .225 .445 .738 1.050 1.336 1.528 1.692 1.818 1.943
1.39244
0.086 .198 .376 .612 .919 1.226 1.471 1.662 1.809 1.940
1.49956
0.076 .172 .321 .514 .779 1.095 1.394 1.629 1.795 1.935
1.60667
0.075 .152 .274 .440 .675 1.000 1.330 1.590 1.778 1.933
1.71378
0.076 .132 .231 .375 .586 .907 1.262 1.552 1.752 1.933
1.82089
0.075 .114 .196 .321 .537 .878 1.260 1.588 1.796 1.945

Table 1 (cont'd)

picture 30

17
9
32.1
19.4
1.0383
1.883
1.883
0.10461
0.050 .067 .144 .293 .590 1.003 1.395 1.681 1.841 1.940 1.991
0.20922
0.055 .091 .220 .413 .702 1.087 1.410 1.644 1.808 1.926 1.989
0.31383
0.064 .114 .293 .512 .819 1.159 1.442 1.642 1.792 1.917 1.992
0.41844
0.071 .146 .353 .600 .927 1.218 1.457 1.643 1.797 1.917 1.992
0.52306
0.073 .180 .414 .698 1.009 1.293 1.497 1.670 1.808 1.922 1.994
0.62767
0.081 .211 .491 .824 1.124 1.362 1.559 1.704 1.820 1.927 1.992
0.73228
0.083 .235 .562 .928 1.212 1.417 1.606 1.730 1.834 1.935 2.001
0.83689
0.085 .246 .596 .970 1.236 1.446 1.616 1.737 1.836 1.932 1.997
0.9415
0.093 .256 .590 .944 1.233 1.457 1.621 1.740 1.837 1.935 2.000
1.04611
0.100 .243 .527 .881 1.197 1.438 1.609 1.732 1.838 1.934 2.003
1.15072
0.106 .238 .464 .774 1.126 1.390 1.585 1.728 1.839 1.939 2.009
1.25533
0.109 .227 .409 .648 .994 1.293 1.540 1.704 1.832 1.938 2.01
1.35994
0.111 .207 .354 .535 .843 1.170 1.452 1.656 1.815 1.933 2.013
1.46456
0.112 .192 .312 .464 .709 1.007 1.341 1.594 1.792 1.936 2.019
1.56917
0.109 .181 .277 .413 .618 .895 1.228 1.520 1.762 1.936 2.021
1.67378
0.109 .175 .261 .383 .572 .848 1.181 1.484 1.751 1.946 2.022
1.77839
0.107 .169 .254 .380 .592 .898 1.264 1.564 1.831 1.972 2.023

Table 1 (cont'd)

picture 345

17
8
32.1
19.4
1.0384
1.928
1.928
0.1071
0.036 .106 .2 .387 .8 1.182 1.463 1.653 1.795 1.902
0.2142
0.036 .115 .227 .430 .817 1.165 1.437 1.628 1.778 1.902
0.3213
0.036 .148 .269 .514 .921 1.238 1.475 1.641 1.780 1.902
0.4284
0.036 .172 .335 .678 1.062 1.337 1.535 1.681 1.794 1.902
0.5356
0.036 .199 .431 .903 1.210 1.430 1.588 1.699 1.798 1.902
0.6427
0.036 .248 .662 1.074 1.328 1.502 1.624 1.718 1.807 1.902
0.7498
0.036 .343 .852 1.194 1.4 1.543 1.646 1.730 1.809 1.902
0.8569
0.036 .435 .934 1.259 1.435 1.559 1.657 1.735 1.813 1.902
0.964
0.036 .428 .986 1.279 1.441 1.566 1.657 1.736 1.811 1.902
1.0711
0.036 .326 .851 1.236 1.425 1.559 1.654 1.735 1.809 1.902
1.1782
0.036 .261 .619 1.143 1.379 1.525 1.635 1.724 1.806 1.902
1.2853
0.036 .190 .403 .925 1.261 1.469 1.604 1.706 1.797 1.902
1.3924
0.036 .159 .301 .591 1.081 1.366 1.549 1.679 1.784 1.902
1.4996
0.036 .128 .249 .423 .811 1.206 1.454 1.623 1.766 1.902
1.6067
0.036 .112 .218 .349 .618 1.029 1.336 1.579 1.755 1.902
1.7138
0.036 .093 .195 .322 .527 .9 1.258 1.541 1.759 1.902
1.8209
0.036 .085 .194 .330 .540 .912 1.311 1.590 1.783 1.902

Table 1 (cont'd)

picture 340

17
9
32.1
19.4
1.0384
1.856
1.863
.1031
.0 .031 .124 .245 .485 .871 1.24 1.562 1.728 1.869 1.934
.2062
.0 .049 .149 .276 .539 .923 1.223 1.473 1.679 1.839 1.932
.3093
.0 .061 .176 .33 .653 1.023 1.287 1.516 1.7 1.844 1.928
.4124
.0 .074 .21 .42 .847 1.157 1.383 1.585 1.731 1.841 1.927
0.5156
.0 .102 .288 .624 1.038 1.278 1.474 1.642 1.756 1.856 1.925
0.6187
.0 .135 .391 .862 1.16 1.373 1.54 1.671 1.772 1.86 1.924
0.7218
.0 .171 .564 .993 1.244 1.433 1.575 1.688 1.78 1.862 1.922
0.8249
.0 .211 .707 1.073 1.303 1.471 1.595 1.699 1.787 1.867 1.918
0.928
.0 .244 .735 1.091 1.312 1.481 1.599 1.699 1.785 1.867 1.918
1.0311
.0 .238 .675 1.064 1.308 1.473 1.592 1.695 1.782 1.866 1.918
1.1342
.0 .201 .518 .972 1.256 1.441 1.572 1.68 1.77 1.86 1.919
1.2373
.0 .177 .384 .777 1.148 1.377 1.538 1.658 1.76 1.855 1.92
1.3404
.0 .15 .309 .547 .98 1.276 1.483 1.629 1.746 1.853 1.924
1.4436
.0 .134 .261 .435 .78 1.128 1.401 1.59 1.728 1.846 1.926
1.5467
.0 .125 .24 .388 .647 1.013 1.323 1.549 1.719 1.847 1.931
1.65
.0 .113 .225 .365 .59 .94 1.263 1.523 1.72 1.85 1.935
1.7529
.0 .093 .212 .355 .566 .907 1.257 1.543 1.75 1.874 1.941

Table 1 (cont'd)

picture 342

17
9
32.1
19.4
1.0384
1.935
1.935
0.1075
0.064 .138 .242 .385 .643 .963 1.291 1.556 1.750 1.855 1.927
0.215
0.064 .169 .282 .438 .704 1.008 1.302 1.522 1.71 1.832 1.927
0.3225
0.064 .187 .316 .493 .798 1.087 1.341 1.547 1.7 1.824 1.927
0.43
0.064 .205 .36 .58 .914 1.177 1.401 1.58 1.72 1.826 1.927
0.5375
0.064 .237 .429 .737 1.052 1.291 1.481 1.632 1.733 1.831 1.927
0.645
0.064 .281 .567 .905 1.174 1.378 1.542 1.658 1.749 1.841 1.927
0.7525
0.064 .334 .705 1.009 1.245 1.434 1.567 1.672 1.760 1.840 1.927
0.86
0.064 .390 .795 1.080 1.300 1.467 1.588 1.681 1.763 1.842 1.927
0.9675
0.064 .383 .772 1.080 1.316 1.472 1.589 1.681 1.764 1.843 1.927
1.075
0.064 .324 .694 1.040 1.280 1.446 1.572 1.668 1.756 1.837 1.927
1.1825
0.064 .269 .549 .920 1.205 1.402 1.539 1.648 1.743 1.881 1.927
1.29
0.064 .229 .433 .765 1.110 1.330 1.497 1.622 1.729 1.827 1.927
1.3975
0.064 .199 .357 .576 .953 1.224 1.428 1.586 1.707 1.818 1.927
1.505
0.064 .184 .312 .478 .774 1.097 1.347 1.543 1.690 1.813 1.927
1.6125
0.064 .167 .275 .416 .660 .982 1.277 1.496 1.666 1.807 1.927
1.72
0.064 .151 .245 .377 .584 .895 1.209 1.461 1.642 1.800 1.927
1.8275
0.064 .135 .222 .347 .563 .874 1.202 1.472 1.684 1.836 1.927

Table 1 (cont'd)

picture 343

17
9
32.1
19.4
1.0384
1.838
1.861
0.10211
0.098 .189 .310 .525 .950 1.363 1.623 1.819 1.928 2.018 2.045
0.20422
0.103 .229 .370 .595 1.023 1.369 1.593 1.777 1.901 2.007 2.041
0.30633
0.108 .263 .433 .730 1.115 1.390 1.601 1.762 1.885 1.996 2.041
0.40844
0.110 .287 .507 .896 1.218 1.443 1.633 1.775 1.888 1.989 2.041
0.5106
0.116 .336 .644 1.038 1.312 1.513 1.671 1.786 1.894 1.985 2.037
0.6127
0.117 .396 .811 1.182 1.390 1.578 1.707 1.802 1.895 1.979 2.030
0.7148
0.120 .459 .960 1.250 1.442 1.606 1.716 1.809 1.895 1.975 2.029
0.8169
0.123 .484 1.009 1.283 1.464 1.619 1.720 1.810 1.893 1.966 2.025
0.9190
0.121 .423 .914 1.248 1.454 1.603 1.718 1.807 1.890 1.960 2.020
1.0211
0.121 .348 .764 1.191 1.420 1.587 1.705 1.802 1.885 1.960 2.022
1.1232
0.119 .286 .542 1.041 1.336 1.536 1.670 1.782 1.876 1.953 2.022
1.2253
0.119 .247 .416 .772 1.201 1.446 1.617 1.745 1.854 1.942 2.019
1.3274
0.116 .220 .350 .540 .984 1.307 1.525 1.693 1.831 1.931 2.019
1.4296
0.118 .200 .305 .454 .722 1.116 1.394 1.617 1.786 1.910 2.011
1.5317
0.116 .182 .274 .392 .574 .918 1.236 1.506 1.727 1.887 2.011
1.6338
0.116 .171 .252 .354 .512 .800 1.108 1.423 1.656 1.861 2.013
1.7359
0.115 .163 .242 .346 .510 .795 1.090 1.420 1.646 1.878 2.017

Table 1 (cont'd)

picture 445

17
9
33.2
19.6
1.0408
1.924
1.955
.1069
.045 .083 .153 .248 .485 .905 1.231 1.496 1.671 1.807 1.912
0.2138
.044 .095 .170 .282 .580 .983 1.279 1.483 1.653 1.787 1.911
0.3207
0.047 .115 .207 .362 .788 1.140 1.367 1.540 1.683 1.800 1.912
0.4276
0.054 .138 .248 .532 1.048 1.287 1.468 1.606 1.722 1.816 1.912
0.5344
0.060 .172 .345 .963 1.230 1.419 1.566 1.665 1.753 1.830 1.918
0.6413
0.067 .229 .684 1.163 1.360 1.500 1.612 1.693 1.777 1.843 1.918
0.7482
0.069 .324 .966 1.272 1.436 1.548 1.643 1.717 1.783 1.844 1.917
0.8551
0.072 .518 1.109 1.329 1.473 1.576 1.659 1.727 1.793 1.847 1.916
0.962
0.074 .485 1.164 1.360 1.483 1.586 1.661 1.730 1.789 1.849 1.917
1.0689
0.076 .326 1.079 1.340 1.478 1.577 1.657 1.727 1.786 1.847 1.915
1.1758
0.077 .228 .644 1.285 1.443 1.555 1.644 1.712 1.783 1.843 1.914
1.2827
0.069 .182 .327 1.123 1.365 1.509 1.618 1.698 1.770 1.842 1.911
1.3896
0.059 .148 .252 .479 1.230 1.432 1.569 1.669 1.756 1.837 1.911
1.4964
0.051 .125 .213 .338 .908 1.284 1.490 1.628 1.735 1.830 1.909
1.6033
0.052 .114 .192 .292 .544 1.074 1.359 1.569 1.710 1.823 1.909
1.7102
0.045 .107 .186 .292 .454 .881 1.249 1.495 1.687 1.822 1.910
1.8171
0.035 .101 .184 .301 .484 .853 1.215 1.511 1.711 1.837 1.908

Table 1 (cont'd)

picture 440

17
10
33.2
19.6
1.0408
1.851
1.861
0.10283
0.073 .111 .179 .267 .418 .723 1.085 1.382 1.638 1.807 1.935 2.001
0.20567
0.075 .122 .198 .290 .445 .798 1.139 1.390 1.617 1.786 1.915 1.998
0.3085
0.076 .133 .212 .318 .545 .984 1.260 1.474 1.662 1.806 1.918 1.992
0.41133
0.081 .152 .250 .392 .829 1.176 1.400 1.583 1.730 1.840 1.931 1.994
0.51417
0.083 .168 .297 .559 1.092 1.335 1.515 1.658 1.771 1.861 1.937 1.993
0.617
0.086 .195 .377 .888 1.236 1.445 1.589 1.706 1.797 1.875 1.942 1.991
0.71983
0.088 .231 .546 1.091 1.341 1.518 1.634 1.731 1.810 1.880 1.944 1.991
0.82267
0.091 .268 .720 1.169 1.414 1.551 1.654 1.743 1.817 1.883 1.943 1.989
0.9255
0.090 .286 .743 1.205 1.432 1.561 1.662 1.745 1.818 1.884 1.945 1.991
1.02833
0.091 .261 .566 1.156 1.412 1.549 1.656 1.739 1.812 1.883 1.945 1.992
1.13117
0.088 .230 .420 1.048 1.349 1.512 1.630 1.725 1.802 1.877 1.942 1.995
1.234
0.088 .202 .334 .611 1.225 1.435 1.585 1.695 1.786 1.869 1.939 1.996
1.33683
0.088 .185 .290 .430 .966 1.305 1.500 1.651 1.761 1.855 1.939 1.999
1.43966
0.087 .173 .264 .375 .610 1.105 1.379 1.577 1.719 1.834 1.927 2.003
1.5425
0.087 .166 .249 .343 .5 .854 1.219 1.479 1.673 1.815 1.924 2.005
1.64533
0.086 .164 .241 .341 .479 .740 1.104 1.396 1.623 1.805 1.923 2.011
1.74817
0.084 .152 .233 .335 .476 .715 1.057 1.364 1.629 1.818 1.938 2.015

Table 1 (cont'd)

picture 443

17
9
33.2
19.6
1.0408
1.863
1.880
0.1035
0.020 .069 .149 .277 .554 1.105 1.474 1.698 1.832 1.922 1.963
0.207
0.033 .1 .194 .335 .659 1.183 1.474 1.675 1.801 1.900 1.961
0.3105
0.046 .128 .239 .402 .916 1.295 1.525 1.684 1.807 1.901 1.961
0.414
0.047 .154 .290 .582 1.159 1.410 1.586 1.714 1.819 1.906 1.963
0.5175
0.060 .198 .387 1.013 1.317 1.513 1.639 1.743 1.831 1.908 1.962
0.621
0.067 .263 .631 1.228 1.438 1.574 1.682 1.766 1.838 1.908 1.958
0.7245
0.068 .349 1.016 1.319 1.494 1.610 1.697 1.775 1.844 1.908 1.957
0.828
0.068 .459 1.116 1.365 1.518 1.625 1.708 1.780 1.844 1.904 1.954
0.9315
0.068 .420 1.092 1.367 1.520 1.626 1.709 1.781 1.845 1.904 1.954
1.035
0.068 .298 .969 1.328 1.491 1.607 1.702 1.777 1.844 1.900 1.955
1.1385
0.068 .220 .493 1.224 1.440 1.574 1.677 1.762 1.835 1.895 1.955
1.242
0.065 .172 .328 .991 1.339 1.513 1.639 1.737 1.820 1.888 1.953
1.3455
0.061 .145 .257 .438 1.115 1.398 1.566 1.695 1.796 1.875 1.946
1.449
0.058 .122 .212 .338 .707 1.188 1.447 1.631 1.760 1.861 1.940
1.5525
0.054 .112 .186 .283 .462 .924 1.285 1.523 1.706 1.838 1.930
1.656
0.053 .100 .169 .252 .394 .696 1.103 1.402 1.645 1.810 1.946
1.7595
0.053 .099 .164 .251 .397 .681 1.019 1.385 1.629 1.817 1.943

Table 1 (cont'd)

picture 41

17
10
33.1
19.8
1.0396
1.853
1.87
0.102944
0.049 .074 .127 .202 .330 .632 1.016 1.291 1.496 1.647 1.764 1.858
0.205889
0.047 .079 .139 .218 .346 .734 1.110 1.337 1.509 1.646 1.760 1.854
0.30883
0.044 .087 .153 .234 .411 .976 1.250 1.429 1.575 1.688 1.777 1.861
0.411778
0.042 .096 .170 .281 .869 1.214 1.396 1.530 1.635 1.719 1.789 1.861
0.52372
0.040 .105 .208 .445 1.189 1.373 1.500 1.595 1.670 1.739 1.797 1.858
0.617667
0.044 .124 .286 1.057 1.319 1.455 1.555 1.631 1.691 1.750 1.801 1.854
0.72061
0.044 .169 .531 1.206 1.397 1.503 1.583 1.650 1.703 1.754 1.804 1.862
0.823555
0.041 .251 .820 1.280 1.437 1.528 1.601 1.659 1.712 1.761 1.807 1.860
0.9265
0.045 .270 .961 1.320 1.454 1.539 1.608 1.663 1.712 1.762 1.810 1.853
1.02944
0.046 .193 .533 1.308 1.446 1.537 1.604 1.662 1.711 1.763 1.810 1.853
1.13239
0.050 .152 .303 1.249 1.424 1.519 1.594 1.657 1.708 1.762 1.809 1.860
1.23533
0.048 .125 .224 1.122 1.366 1.483 1.576 1.643 1.701 1.758 1.814 1.858
1.3383
0.044 .115 .189 .315 1.250 1.413 1.532 1.621 1.690 1.753 1.814 1.858
1.44122
0.042 .104 .171 .267 1.014 1.280 1.457 1.579 1.668 1.747 1.816 1.855
1.54417
0.040 .098 .163 .251 .448 1.090 1.347 1.513 1.642 1.737 1.820 1.852
1.6471
0.049 .1 .164 .254 .411 .879 1.229 1.433 1.602 1.729 1.822 1.852
1.75005
0.039 .097 .161 .248 .405 .892 1.234 1.441 1.602 1.731 1.818 1.852

Table 1 (cont'd)

picture 43

17
11
33.1
19.8
1.0396
1.808
1.828
0.10044
0.051 .097 .157 .231 .355 .619 .973 1.230 1.454 1.634 1.760 1.859 1.918
0.20089
0.050 .102 .165 .237 .362 .668 1.047 1.279 1.457 1.615 1.741 1.838 1.914
0.30133
0.053 .107 .178 .255 .402 .900 1.187 1.377 1.530 1.659 1.762 1.842 1.914
0.40178
0.053 .116 .192 .293 .562 1.127 1.340 1.489 1.610 1.708 1.786 1.850 1.913
0.50222
0.057 .123 .226 .366 1.035 1.288 1.453 1.571 1.663 1.738 1.8 1.856 1.912
0.6027
0.057 .136 .272 .666 1.199 1.406 1.528 1.619 1.694 1.757 1.812 1.861 1.911
0.7031
0.057 .172 .384 .980 1.305 1.475 1.573 1.651 1.717 1.771 1.822 1.869 1.914
0.8036
0.062 .193 .522 1.073 1.361 1.501 1.592 1.665 1.727 1.778 1.828 1.872 1.915
0.904
0.062 .215 .500 1.062 1.379 1.514 1.601 1.671 1.731 1.781 1.831 1.875 1.913
1.00444
0.066 .196 .380 .951 1.355 1.502 1.597 1.669 1.731 1.783 1.833 1.879 1.926
1.10489
0.066 .168 .295 .521 1.282 1.462 1.572 1.654 1.721 1.777 1.829 1.879 1.924
1.2053
0.070 .151 .250 .385 1.133 1.386 1.522 1.621 1.699 1.762 1.822 1.877 1.929
1.3058
0.074 .137 .219 .317 .533 1.242 1.426 1.562 1.660 1.739 1.809 1.871 1.926
1.40622
0.073 .130 .202 .282 .418 .993 1.269 1.456 1.596 1.703 1.790 1.860 1.930
1.50667
0.075 .128 .191 .269 .379 .658 1.084 1.329 1.502 1.653 1.765 1.849 1.931
1.60711
0.075 .121 .186 .264 .379 .573 .936 1.210 1.425 1.603 1.743 1.846 1.936
1.70755
0.076 .125 .188 .269 .403 .595 .886 1.162 1.395 1.598 1.751 1.862 1.947

Table 1 (cont'd)

picture 40

17
8
33.1
19.8
1.0396
1.808
1.815
0.10044
0.112 .145 .212 .322 .672 1.347 1.656 1.828 1.922 2.019
0.20088
0.116 .162 .240 .347 .844 1.421 1.648 1.809 1.911 2.006
0.30133
0.120 .179 .268 .390 1.222 1.523 1.696 1.823 1.917 2.007
0.4018
0.123 .196 .290 .465 1.407 1.601 1.740 1.845 1.921 2.006
0.5022
0.132 .232 .376 1.400 1.577 1.708 1.797 1.872 1.938 2.005
0.6027
0.149 .281 1.272 1.527 1.657 1.755 1.826 1.890 1.946 2.005
0.7031
0.149 .384 1.424 1.605 1.705 1.783 1.846 1.899 1.950 2.002
0.8036
0.150 .574 1.487 1.635 1.719 1.793 1.847 1.901 1.950 2.002
0.904
0.162 .476 1.501 1.642 1.723 1.793 1.850 1.901 1.951 2.003
1.0044
0.163 .349 1.465 1.621 1.714 1.788 1.844 1.900 1.949 2.007
1.1049
0.159 .286 .518 1.572 1.686 1.766 1.829 1.890 1.942 2.006
1.2053
0.161 .256 .377 1.477 1.635 1.735 1.810 1.877 1.935 2.002
1.3058
0.162 .237 .330 .516 1.537 1.676 1.778 1.865 1.929 2.001
1.4062
0.159 .226 .302 .416 1.362 1.568 1.718 1.835 1.915 2.004
1.5067
0.154 .218 .283 .373 .986 1.397 1.612 1.783 1.889 2.016
1.6071
0.156 .215 .275 .357 .554 1.204 1.488 1.719 1.865 2.021
1.7076
0.154 .212 .277 .361 .565 1.075 1.440 1.705 1.885 2.021

LIST OF REFERENCES

LIST OF REFERENCES

Abell, S. and Hudson, J. L. ,"An Experimental Study of Centrifugally Driven Free Convection in a Rectangular Cavity", *Int. J. Heat and Mass Transfer,* vol. 18, pp. 1415-1423, 1975.

Bajorek, S.M. ,"Experimental Investigation of Natural Convection in Partitioned Enclosures," M.S. Thesis, University of Notre Dame, 1981.

Ball, K.S., Farouk, B. and Dixit, V.C. ,"An Experimental Study of Heat Tranfer in a Vertical Annulus with a Rotating Inner Cylinder", *Int. J. Heat Mass Transfer,* vol. 32, No. 8, pp. 1517-1527, 1989.

Barua, S.N. ,"Secondary Flow in a Rotating Straight Pipe", *Roy. Soc. London,* Ser. A, vol. 227, pp.133-139, 1955.

Bergles, A.E. ,"Survey and Evaluation of Techniques to Augment Convection Heat and Mass Transfer", *Progress in Heat and Mass Transfer,* Pargamon Press, vol. 1, p. 323, 1968.

Bühler, K. and Oertel, H. ,"Thermal Cellular Convection in Rotating Rectangular Boxes", *J. Fluid Mech.* , vol. 114, pp. 261-282, 1982.

Cannon, J.N. and Kays, W.M. ."Heat Transfer to a Fluid Flowing Inside a Pipe Rotating about its Longitudinal Axis," *J. of Heat Transfer,* vol. 91, pp. 135-139, 1969.

Catton, I. ,"The Influence of Rotation on Natural Convection in Horizontal Liquid Layers," *Fourth International Heat Conference,* Paris-Versailles, vol. IV, NC 4.1, pp. 1-10, 1970.

Chandrasekhar, R. S. , *Hydrodynamic and Hydromagnetic Stability* , Oxford University Press, London, 1961.

Clever, R.M. and Busse, F.H. ,"Nonlinear Properties of Convection Rolls in a Horizontal Layer Rotating about a Vertical Axis," *J. Fluid Mech.*, vol. 30, pp. 465-478, 1979.

Draper, N.R. and Smith, H., *Applied Regression Analysis*, second ed., John Wiley & Sons, New York, 1981.

DiPrima, R.C. and Swinney, H.L. ,"Instabilities and Transition in Flow between Concentric Rotating Cylinders," *in Hydrodynamic Instabilities and the Transition to Turbulence*, ed. H.L. Swinney and J.P. Gollub, Chap. 6, pp.139-180, Springer-Verlag, Berlin Heidelberg, 1981.

De Vahl Davis, G. , Leonardi, E. and Reizes, J. A. ,"Convection in a Rotating Annular Cavity", *Heat and Mass Transfer in Rotating Machinery* , eds. D. E. Metzger and N. H. Afgan , pp. 131-142, Hemisphere, 1984.

Eckels, P.W., Parker, Jr., J.H. and Patterson, A. ,"Secondary Flow Effects in High Tip Speed Free Convection," *J. Heat Transfer*, vol. 109, pp. 97-103, 1987.

Edwards, D.K. ,"Rotation Induced Free-Convection Heat Transfer in a Zero Gravity Field," *AIAA J.*, vol. 5, No. 2, p. 333, 1967.

El-Masri, M. A. ,"A Proposed Regenerative Thermosyphone Blade Cooling System for High Efficiency Gas Turbine", *Heat and Mass Transfer in Rotating Machinery* , eds D. E. Metzger and N. H. Afgan , pp. 645-658, Hemisphere, 1984.

Firouzian, M., Owen, J.M., Pincombe, J.R. and Rogers, R.H. ,"Fluid Dynamics and Heat Transfer in a Rotating Cylinderical Cavity with a Radial Inflow of Fluid. Part 1: The Flow Structure," *Int. J. Heat Fluid Flow*, vol. 6, p. 228, 1985.

Firouzian, M., Owen, J.M., Pincombe, J.R. and Rogers, R.H. ,"Fluid Dynamics and Heat Transfer in a Rotating Cylinderical Cavity with a Radial Inflow of Fluid. Part 2: Velocity, Pressure and Heat Transfer Measurements," *Int. J. Heat Fluid Flow*, vol. 7, p. 21, 1986.

Gebhart, B. ,*Heat Transfer*, 2nd ed., McGraw-Hill, New York, 1971.

Gilman, P. A. ,"Convection in Rotating Annulus Uniformly Heated From Below. Part 2. Nonlinear Results", *J. Fluid Mech.* , vol. 57, pp. 381-400, 1973.

Goldstein, R.J. ,"Optical Techniques For Temperature Measurement," *Measurements in Heat Transfer,* eds. E.R.G. Eckert and R.J. Goldstein, 2nd ed., Hemisphere, 1976.

Hamady, F. J. ,"Experimental Study of Local Natural Convection Heat Transfer in Inclined and Rotating Enclosures", Ph. D. dissertation, Michigan State University, 1987.

Hamady, F.J., Lloyd, J.R., Yang, H.Q. and Yang, K.T. ,"A Study of Natural Convection in a Rotating Enclosure," submitted to *Int. J. Heat Mass Transfer,* 1990.

Homsy, G.M. and Hudson, J.L. ,"Heat Transfer in a Rotating Cylinder of Fluid Heated From Above," *Int. J. Heat Mass Transfer,* vol. 14, pp. 1149-1159, 1971.

Homsy, G.M. and Hudson, J.L. ,"Stability of Radially Bounded Rotating Fluid Heated From Below," *Appl. Sci. Res.,* vol. 26, pp. 33-66, 1972.

Hudson, J. L. ,"Experiments on Centrifugally Driven Thermal Convection in a Rotating Cylinder", *J. Fluid Mech.* , vol. 86, pp. 147-159, 1970.

Humphrey, J.F., Morris, W.D. and Barrow, H. ,"Convection Heat Transfer in the Entry Region of a Tube which Revolves about an Axis Parallel to Itself," *Int. J. Heat Mass Transfer,* vol. 10, pp. 333-347, 1967.

Hunter, C. and Riahi, N. ,"Nonlinear Convection in a Rotating Fluid," *J. Fluid Mech.,* vol. 72, pp. 433-454, 1975.

Kataoka, K., Bitou, Y., Hashioka, K., Komai, T. and Doi, H. ,"Mass Transfer in the Annulus between Two Coaxial Rotating Cylinders," *in Heat and Mass Transfer in Rotating Machinery,* ed. D.E. Metzger and N.H. Afgan, pp. 143-153, Hemisphere, Washington, D.C., 1984.

Kataoka, K. and Deguchi, T. ,"Generation and Evolution of Turbulence in an Annulus between Two Concentric Rotating Cylinders," *in Heat Transfer and Fluid Flow in Rotating Machinery,* ed. W.J. Yang, pp. 245-254, Hemesphere, Washington, D.C., 1987.

Kheshgi, H.S. and Scriven, L.E. ,"Viscous Flow Through a Rotating Square Channel," Phys. Fluids, vol. 28, No. 10, pp.2868-2979, 1985.

Kline, S.J. and McClintock, F.A. ,"The Description of Uncertainties in a Single Sample Experiments," *Mechanical Engineering*, vol. 75, pp. 3-9, 1953.

Kuzay, T.M. and Scott, C.J. ,"Turbulent Heat Transfer in an Annulus with Inner Cylinder Rotation," *J. Heat Transfer*, vol. 99, pp. 12-19, 1977.

Langlois, W.E. ,"Computer Simulation of Czochralski Melt Convection in a Magnetic Field," *J. Crystal Growth*, vol. 70, pp. 73-77, 1984.

Langlois, W.E. ,"Buoyancy-Driven Flows in Crystal-Growth Melts," *Ann. Rev. Fluid Mech.*, vol. 17, pp. 191-215, 1985.

Levy, E., Neti, S., Brown, G. and Bayat, F. ,"Laminr Heat Transfer and Pressure Drop in a Rectangular Duct Rotating about a Parallel Axis," *J. Heat Transfer*, vol. 108, pp. 350-356, 1986.

Marto, P. J. ,"Rotating Heat Pipes", *Heat and Mass Transfer in Rotating Machinery* , eds. D. E. Metzger and N. H. Afgan, pp. 609-632, Hemisphere, 1984.

Metzger, D. E. ,"Fundamental Heat Transfer Research for Gas Turbine Engines: NASA Workshop Overview", *Heat and Mass Transfer in Rotating Machinery* , eds. D. E. Metzger and N. H. Afgan, pp. 381-396, Hemisphere, 1984.

Metzger, D.E. and Afgan, N.H. , *Heat and Mass Transfer in Rotating Machinery*, Hemisphere, 1984.

Mori, Y. and Nakayama, W. ,"Forced Convection Heat Transfer in a Straight Pipe Rotating around a Parallel Axis (1st report, Laminar region)," *Int. J. Heat Mass Transfer*, vol. 10, pp. 1179-1194, 1967.

Mori, Y. and Nakayama, W. ,"Convection Heat Transfer in Rotating Radial Circular Pipes," *J. Heat Mass Transfer*, vol. 11, pp. 1027-1040, 1968.

Mori, Y., Fukada, T. and Nakayama, W. ,"Convective Heat Transfer in a Rotating Radial Circular Pipe," *Int. J. Heat Mass Transfer*, vol. 14, p. 1807, 1971.

Morris, W.D. and Ayhan, T. ,"Observations on the Influence of Rotation on Heat Transfer in the Coolant Channels of Gas Turbine Rotor Blades," *Inst. Mech. Eng. Proc.*, vol. 193, pp. 303-311, 1979.

Morris, W.D. and Ayhan, T. ,"An Experimental Study of Turbulent Heat Transfer in a Tube which Rotates about an Orthogonal Axis," *Heat and Mass Transfer in Rotating Machinery* ,ed. D.E. Metzger and N.H. Afgan, pp. 25-37, Hemisphere, Washington, D.C., 1984.

Morris, W.D. ,*Heat Transfer and Fluid Flow in Rotating Coolant Channels,* Wiley, 1981.

Nakayama, W. ,"Forced Convection Heat Transfer in a Straight Pipe Rotating around a Parallel Axis (2nd report, Turbulent region)," *Int. J. Heat Mass Transfer,* vol. 11, pp. 1185-1201, 1968.

Neti, S., Warnock, A.S., Sevy, E.K. and Kannan K.S. ,"Computation of Laminar Heat transfer in Rotating Rectangular Ducts," *J. Heat Transfer,* vol. 107, pp. 575-582, 1985.

Nothrop, A. and Owen, J.M. ,"Heat Transfer Measurements in Rotating-Disc Systems, Part 2: The Rotating Cavity with a Radial Outflow of Coolant Air," *Int. J. Heat and Fluid Flow,* vol. 9, No. 1, pp. 27-36, 1988.

Potter, M.C. and Foss, J.F. , *Fluid Mechanics,* John Wiley & Son, 1975.

Randriamampianina, A. , Bontoux, P. et Roux, B. ,"Ecoulements Induits par la Force Gravifique dans une Cavite Cylinderique en Rotation", *Int. J. Heat Mass Transfer,* vol. 30, pp. 1275-1292, 1987.

Rossby, H. T. ,"A Study of Benard Convection With and Without Rotation", *J. Fluid Mech.* , vol. 36, pp. 309-335, 1969.

Sakamoto, M. and Fuki, S. ,"Convection Heat Transfer of a Rotating Tube Revolving about an Axis Parallel to itself," *Fourth Int. Heat Transfer Conf.,* vol. III, Paper FC7.2, pp. 1-11, Paris-Versailles, 1970.

Schmidt, E. ,"Heat Transmission by Natural Convection at High Centrifugal Acceleration in Water-Cooled Gas Turbine Blades", *Proc. Gen. Disc. on Heat Transfer, IV,* pp. 361-363, Instn. Mech. Engrs. , London, 1951.

Siegel, R. ,"Analysis of Buoyancy Effect on Fully Developed Laminar Heat Transfer in a Rotating Tube, *J. Heat Transfer,* vol. 107, pp. 338-344, 1985.

Siegwarth, D.P., Mikesell, R.D., Readal, T.C. and Hanratty, T.J. ,"The Effect of Secondary Flow on the Temperature Field and Primary Flow in a Heated Horizontal Tube," *Int. J. Heat Mass Transfer, vol. 12, pp. 1535-1552, 1969.*

Singh, M. and Rajvanshi, S.C. ,"Heat Transfer between Rotating Eccentric Cylinders with Different Radii," *Int. J. Heat Mass Transfer,* vol. 25, pp. 1719-1724, 1982.

Sobel, L., El-Masri, M. and Smith, J.L. ,"Heat Transfer and Flow Visualization in Natural Convection in Rapidly Spinning Systems, *J. Heat Transfer,* vol. 108, pp. 547-553, 1986.

Stephenson, P.L. ,"An Experimental Study of Flow and Heat Transfer in a Duct Rotating about a Parallel Axis," *Heat and Mass Transfer in Rotating Machinery,*" ed. D.E. Metzger and N.H. Afgan, pp. 39-49, Hemisphere, Washington, D.C., 1984.

Torrest, M. A. and Hudson, L. ,"The Effect of Centrifugal Convection on the Stability of a Rotating Fluid Heated From Below ", *Appl. Sci. Res.* vol. 29, pp. 273-289, 1974.

Veronis, G. ,"Large-Amplitude Benard Convection in a Rotating Fluid," *J. Fluid Mech.,* vol. 31, part 1, pp. 113-139, 1968.

Vidyanidhi, V., Suryanarayana, V.V.S. and Chenchu Raju, V.C. ,"An Analysis of Steady Fully Developed Heat Transfer in a Rotating Straight Pipe, *J. Heat Transfer,* vol. 99, pp. 148-150, 1977.

Woods, J.L. and Morris, W.D. ,"A Study of Heat Transfer in a Rotating Cylindrical Tube," *J. Heat Transfer,* vol. 102, pp. 612-616, 1980.

Yang, H.Q. ,"Physics-Based Grid Generation for Three-Dimensional Laminar Buoyant Flow in Rectangular Enclosures," Ph.D. Thesis, University of Notre Dame, 1986.

Yang, H. Q. , Yang, K. T. and Lloyd J. R. ,"Buoyant Flow Calculations with Non-Orthogonal Curvilinear Coordinates for Vertical and Horizontal Parallelepiped Enclosures", to appear in *Int. J. Num. Meth. in Engineering*, (1988a).

Yang, H. Q. , Yang, K. T. and Lloyd, J. R. ,"Rotational Effects on Natural Convection in a Horizontal Cylinder ", *AICHE Journal*vol. 34, No. 10, pp. 1627-1633, (1988).

Yang, H. Q. , Yang, K. T. and Lloyd, J. R. ,"Three-Dimensional Laminar Buoyant Flow in a Horizontal Circular Cylinder with Differentially Heated End Walls at High Rayleigh Numbers", to appear in *Num. Heat Transfer*, (1988b).

Yang, K.T. ,"Natural Convection in Enclosures," Chapter 13, *Handbook of Single Phase Convection Heat Transfer,* ed. K. Kakac, R.K. Shah and W. Aung, Wiley-Interscience, 1987.

Yang, K.T., (personal communication), 1990.

Yang, W.J. , *Heat Transfer and Fluid Flow in Rotating Machinery,* Hemisphere, 1987.

Yong, N.L. and Minkowycz, W.J. ,"Heat Transfer Characteristics of the Annulus of Two Coaxial Cylinders with One Cylinder Rotating," *Int. J. Heat Mass Transfer,* vol. 32, No. 4, pp. 711-722, 1989.

Zhong, Z.Y., Yang, K.T. and Lloyd, J.R. ,"Variable Property Effects in Laminar Natural Convection in a Square Enclosure," *J. Heat Transfer,* vol. 107, pp. 133-138, 1985.